

Random Incident Waves for Fast Compressed Pulse-Echo Ultrasound Imaging

Martin F. Schiffner

Abstract—Established image recovery methods in fast ultrasound imaging, e.g. delay-and-sum, trade the image quality for the high frame rate. Cutting-edge inverse scattering methods based on compressed sensing (CS) disrupt this tradeoff via *a priori* information. They iteratively recover a high-quality image from only a few sequential pulse-echo measurements or less echo signals, if (i) a known dictionary of structural building blocks represents the image almost sparsely, and (ii) their individual pulse echoes, which are predicted by a linear model, are sufficiently uncorrelated. The exclusive modeling of the incident waves as steered plane waves or cylindrical waves, however, has so far limited the convergence speed, the image quality, and the potential to meet condition (ii).

Motivated by the benefits of randomness in CS, a novel method for the fast compressed acquisition and the subsequent recovery of images is proposed to overcome these limitations. It recovers the spatial compressibility fluctuations in weakly-scattering soft tissue structures, where an orthonormal basis meets condition (i), by a sparsity-promoting ℓ_q -minimization method, $q \in [0; 1]$. A realistic d -dimensional model, $d \in \{2, 3\}$, accounting for diffraction, single monopole scattering, the combination of power-law absorption and dispersion, and the specifications of a planar transducer array, predicts the pulse echoes of the individual basis functions. Three innovative types of incident waves, whose syntheses leverage random apodization weights, time delays, or combinations thereof, aid in meeting condition (ii).

In two-dimensional numerical simulations, single realizations of these waves outperform the prevalent quasi-plane wave for both the canonical and the Fourier bases. They significantly decorrelate the pulse echoes, e.g. they reduce the full extents at half maximum of the point spread functions by up to 73.7%. For a tissue-mimicking phantom and $q \in \{1, 0.5\}$, they improve the convergence speed and the image quality in terms of the mean structural similarity indices and the relative root mean-squared errors by up to $\{2.7\%, 22.9\%\}$, $\{44.1\%, 55.5\%\}$, and $\{42\%, 60.5\%\}$, respectively.

Index Terms—random incident waves, inverse scattering, compressed sensing, sparse regularization, ultrafast ultrasound imaging, computational ultrasound imaging, fast multipole method, GPU computing

I. INTRODUCTION

MEDICAL ultrasound imaging (UI) is a safe, cost-effective, portable, and frequently-used modality that provides sub-millimeter spatial resolutions in real-time [1, Fig. 1.15, Table 1.2], [2]. The typical progressive scanning of a specified field of view (FOV) by focused beams, however, requires hundreds of sequential pulse-echo measurements per image and, owing to the finite sound speed, limits the frame rate [3, 536–539], [4], [5]. Advances in electronic miniaturization and processing power have recently led to freely programmable UI systems and software-based “ultrafast” imaging

modes, e.g. coherent plane-wave compounding [6], synthetic aperture (SA) imaging [7], [8], or limited-diffraction beam imaging [9], [10], that overcome this limitation and capture large FOVs at rates in the kilohertz range [11], [1, Sect. 1.11]. Using a fully-sampled transducer array, they sequentially insonify the entire FOV by only a few unfocused waves and process the echo signals generated by all elements. Besides rendering UI safer [12] and more sensitive [13], they have enabled the observation of moving objects and transient phenomena [12], [14], [15], even in three dimensions [16].

The established image recovery methods, which are explicit and computationally efficient, gradually trade the image quality for the frame rate [6], [8], [9], [17]. Their physical models neglect various effects, e.g. the finite number of array elements and their anisotropic directivities, and basic abilities of programmable UI systems, e.g. the syntheses of complex incident waves. The popular delay-and-sum (DAS) method, for example, focuses the echo signals on specified points in the FOV to quantify their echogeneity. Emitting steered plane waves (PWs) [6], [12], [13], [15], [16], whose spatial extent and energy content are unlimited, or outgoing $\{1, 2\}$ -spherical waves [8], [14], [16], whose isotropic sources are points, it adds the signal samples at the round-trip times-of-flight (TOFs) [6, (2), (6)], [8, (4), (5)]. The competing Fourier methods, in contrast, invert the wave equation and potentially improve the image quality at reduced computational costs [7], [9], [10], [17]–[20]. Detecting the scattered waves on infinite planes, they derive the $\{2, 3\}$ -dimensional spatial Fourier transform of the image using either an exploding reflector model for steered PWs [17] or variants of the Fourier diffraction theorem¹ (FDT) for non-diffracting beams, e.g. steered PWs [9], [10], [19], [20] or X waves [9], and outgoing 1-spherical (cylindrical) waves [7].

Novel inverse scattering methods, which increase both the complexity and the computational costs, improve the image quality [24]–[34]. They regularize the ill-posed recovery problem given both a set of echo signals and a linear model for its prediction. Their universality, which stems from the arbitrary sophistication of this model and its optional calibration via experimental measurements, optimally complements the programmable UI systems. For instance, they theoretically support incident waves and array geometries of any complexity, the separate recovery of multiple acoustic material parameters,

¹The FDT (cf. e.g. [21, Thm. 8.4], [22, Thm. 3.1], [23, Sect. 6.3]), which is also referred to as the “generalized projection-slice theorem”, adapts the Fourier slice theorem underlying the image recovery in x-ray computed tomography from rays to diffracting waves. Using the Weyl expansions of the outgoing free-space Green’s functions [21, Sect. 4.1], it decomposes all waves into steered PWs and, thus, facilitates their treatment.

efficient spatiotemporal sampling concepts for data rate reduction, denoising, and the inclusion of *a priori* information about the image. Cutting-edge variants [24], [25], [27]–[30], [32]–[34] have recently adopted “compressed sensing”² (CS), a data acquisition and recovery method providing essential benefits in other modalities [39]–[41], to disrupt the tradeoff between the image quality and the frame rate. They iteratively recover a high-quality image from only a single pulse-echo measurement or less echo signals, if (i) a known dictionary of structural building blocks represents the image almost sparsely, and (ii) their individual pulse echoes, which are predicted by the linear model, are sufficiently uncorrelated.

The linear models, which are formulated in the time domain [24], [25], [28], [29] or the temporal [30]–[34] and spatiotemporal [27] Fourier domains, however, currently limit the convergence speed, the image quality, and the potential to meet condition (ii). Like the established methods, they partly neglect diffraction, the combination of frequency-dependent absorption and dispersion, and the specifications of the instrumentation, including the array geometry, the acoustic lens, and the electromechanical transfer behavior. Moreover, they partly limit the number of spatial dimensions to only two, intermix results for the two- and three-dimensional Euclidean spaces, and replace the acoustic material parameters by an abstract reflectivity function. The exclusive usage of steered PWs [24], [25], [27]–[34] or outgoing cylindrical waves [25] ignores basic abilities of programmable UI systems. The latter typically specifies pulse shapes, apodization weights, and time delays for the waves emitted by the individual array elements and provides hundreds of degrees of freedom to synthesize alternative types of incident waves. Although nonconvex recovery methods require less data [42]–[44], convex variants are prevalent [25], [27], [28], [30], [32]–[34].

The randomization of the apodization weights and the time delays in the syntheses of the incident waves, which is motivated by the essential theorems underlying CS, potentially improves the conformity with condition (ii). In fact, the linear time-shift invariant (LTI) measurement process physically superimposes the weighted and delayed echo signals induced by the individual array elements. Each incident wave randomly projects a complete SA acquisition sequence on a single pulse-echo measurement and, thus, strongly compresses both the acquisition time and the data volume. The few studies of such waves in compressed UI and their origins will now be reviewed.

A. Related Work

The syntheses of random waves in UI partly trace back to time-reversal [45] and computational microwave imaging [46]–[50]. The latter trades the hardware complexity and costs, which are raised by transceiver arrays or mechanical scans, for the computational costs of the image recovery. Highly dispersive customized apertures, e.g. complex metamaterials [47],

[49], [50] or leaky reverberant cavities [46], [48], form virtual transceiver arrays. These expand excitations at sufficiently different frequencies into distinct spatial codes, i.e. spatially erratic incident fields, and, reciprocally, mix the scattered fields in reception, providing frequency-diverse projections of the FOV. The knowledge of the two-way transfer function enables the image recovery. Unlike the random sampling [25], [28], [51] or mixing [25], [52] of the scattered waves, which reduce the number of transceivers and measurements, the random waves improve the conformity with condition (ii).

Kruizinga *et al.* [53] equipped a single transducer with a plastic delay mask to enable compressive three-dimensional UI with cheap and simple hardware. The varying thickness of the mask introduced random time delays into both the emitted and the received waves to decorrelate the pulse echoes received from distinct voxels. Adopting a simple calibration procedure, which measured the random sound field in water and, thus, limited its range of validity, the recovery of sparse objects required 50 sequential pulse-echo measurements at evenly spaced angles of rotation. Ghanbarzadeh-Dagheyani *et al.* [54] optimized a holey cavity with respect to its opening sizes and the materials to enable compressive two-dimensional UI with only a few transceivers. Encasing only two point-like transceivers that perform a complete SA acquisition sequence, its presence significantly improved the lateral resolution of two point-like targets in a lossless homogeneous fluid. Unlike the time-reversal technique [45], which uses a leaky cavity to generate focused beams, the FOV is not progressively scanned.

Van Sloun *et al.* [55] proposed randomly-apodized monofrequent emissions from a circular array in two-dimensional tomography. These outperformed sparse SA acquisition sequences using only a few emissions from random elements. Liu *et al.* [56], [57] realized uniformly-distributed apodization weights for linear and convex arrays. Unlike the inverse scattering methods, they recovered the echo signals induced by a complete SA acquisition sequence, which were represented almost sparsely by a sym8 wavelet basis, and subsequently applied the popular DAS method for image formation. Despite the improvements in contrast and spatial resolution, the large number of unknown temporal samples required tens of sequential pulse-echo measurements per image.

B. Specific Contributions

A method for the fast compressed acquisition and the subsequent recovery of images is proposed that features three major innovations. First, realistic d -dimensional physical models for the pulse-echo measurement process and the syntheses of the incident waves minimize inaccuracies and leverage the abilities of programmable UI systems. They linearly relate the spatial compressibility fluctuations in weakly-scattering soft tissue structures to the radio frequency (RF) voltage signals provided by the instrumentation. They readily support calibration procedures, the usage of measured incident fields, and applications beyond ultrafast UI, e.g. progressive scanning, structured insonification, or simulation studies. Second, three innovative types of energy equivalent random waves are synthesized using random apodization weights, time delays, or

²The initial distinction between the terms “sparse recovery” and “compressed sensing” (CS), which was based on the usage of either deterministic or random sensing matrices and their theoretical guarantees, has been abandoned [35, 2], [36]. Additional names include “compressive sensing” [37] and “compressive sampling” [38].

TABLE I: Summary of the mathematical symbols used throughout the paper.

Symbol	Meaning
$[N]$	Set of consecutive positive integers, $[N] = \{1, 2, \dots, N\}$ for $N \in \mathbb{N}$
$[N]_0$	Set of consecutive nonnegative integers, $[N]_0 = \{0, 1, \dots, N\}$ for $N \in \mathbb{N}_0$
$\langle \mathbf{a}, \mathbf{b} \rangle$	Inner product of the vectors $\mathbf{a} = (a_1, \dots, a_N)^T \in \mathbb{C}^N$ and $\mathbf{b} = (b_1, \dots, b_N)^T \in \mathbb{C}^N$, $\langle \mathbf{a}, \mathbf{b} \rangle = \sum_{n=1}^N a_n b_n^*$
$\ \mathbf{a}\ _q$	ℓ_q -norm, $q \in [1; \infty)$, or ℓ_q -quasinorm, $q \in (0; 1)$, of the vector $\mathbf{a} \in \mathbb{C}^N$, $\ \mathbf{a}\ _q = \sum_{n=1}^N a_n ^q$
$\ \mathbf{a}\ _0$	Number of nonzero components, $\ \mathbf{a}\ _0 := \ \mathbf{a}\ _0^0 = \lim_{q \rightarrow 0} \ \mathbf{a}\ _q = \{n \in [N] : a_n \neq 0\} $
\mathbf{r}	Spatial position in the d -dimensional Euclidean space, $\mathbf{r} = (r_1, \dots, r_d)^T \in \mathbb{R}^d$
\mathbf{r}_ρ, r_d	Lateral coordinates $\mathbf{r}_\rho = (r_1, \dots, r_{d-1})^T \in \mathbb{R}^{d-1}$ and axial coordinate $r_d \in \mathbb{R}$ of the spatial position $\mathbf{r} = (\mathbf{r}_\rho^T, r_d)^T$
\mathbb{S}^{d-1}	Unit $(d-1)$ -sphere, $\mathbb{S}^{d-1} = \{\mathbf{r} \in \mathbb{R}^d : \ \mathbf{r}\ _2 = 1\}$
\mathbb{S}_+^{d-1}	Unit $(d-1)$ -hemisphere, $\mathbb{S}_+^{d-1} = \{\mathbf{r} \in \mathbb{R}^d : \ \mathbf{r}\ _2 = 1, r_d \in \mathbb{R}^+\}$
\mathbf{e}_δ	Unit vector indicating the direction of the r_δ -axis, $\delta \in [d]$, in a d -dimensional Cartesian coordinate system, $\mathbf{e}_\delta \in \mathbb{S}^{d-1}$
\mathbf{H}	Superscript indicating an adjoint (conjugate transpose) matrix
\mathbf{I}	Identity matrix
$\tilde{\cdot}$	Tilde accent indicating a time-domain signal

combinations thereof. The associated spatial codes decorrelate the pulse echoes of the structural building blocks defined by an orthonormal basis meeting condition (i) and, thus, improve the conformity with condition (ii). Third, both convex and nonconvex variants of a sparsity-promoting ℓ_q -minimization method, $q \in [0; 1]$, enable the quantitative recovery of the compressibility fluctuations.

Two-dimensional numerical simulations validate the proposed method using single realizations of the random waves for a wire phantom and a tissue-mimicking phantom. Although the random waves decrease the robustness against additive errors for the wire phantom, they significantly increase both the image quality and the convergence speed for the tissue-mimicking phantom. The study significantly expands the initial results published in two abstracts [58], [59].

These contributions are organized as follows. Section II briefly reviews the CS framework. Sections III and IV present the physical models for the pulse-echo measurement process and the syntheses of the incident waves. Section V details the image recovery based on CS, and Sect. VI adds an efficient matrix-free implementation. Section VII summarizes the parameters of the numerical simulations, and Sect. VIII presents the results. Section IX discusses these results and the proposed method. Eventually, Sect. X concludes the paper. Table I summarizes the mathematical symbols.

II. COMPRESSED SENSING IN A NUTSHELL

CS deals with the stable³ recovery of a high-dimensional vector $\mathbf{x} \in \mathbb{C}^N$ from a low-dimensional vector of potentially corrupted observations $\mathbf{y}^{(\eta)} \in \mathbb{C}^M$, $M \ll N$. Both vectors satisfy the underdetermined linear algebraic system

$$\mathbf{y}^{(\eta)} = \Phi \mathbf{x} + \boldsymbol{\eta}, \quad (1)$$

where the known matrix $\Phi \in \mathbb{C}^{M \times N}$ represents the nonadaptive observation process, and the unknown vector $\boldsymbol{\eta} \in \mathbb{C}^M$ denotes additive errors of bounded ℓ_2 -norm $\|\boldsymbol{\eta}\|_2 \leq \eta$.

Since basic linear algebra either negates the existence of any solution to the underdetermined linear algebraic system

³The adjective ‘‘stable’’ indicates that neither inaccurate observations nor a sparsity defect result in huge recovery errors [35, 7, 8].

(1) or predicts infinitely many solutions, CS replaces the identity by an inequality using the known upper bound on the ℓ_2 -norm of the additive errors and postulates that a known dictionary of structural building blocks, e.g. an orthonormal basis or a frame, represents the high-dimensional vector almost sparsely [60]. The latter constraint effectively reduces the total number of unknown components to a relatively small number of unknown coefficients associated with the relevant structural building blocks. The identification of these building blocks and the subsequent estimation of their coefficients then enable the approximate recovery of the high-dimensional vector. Both measures render CS a unique type of regularization method (cf. e.g. [61, Chapt. 1], [62, Sect. 1.3]).

Let the column vectors $\boldsymbol{\psi}_n \in \mathbb{C}^N$, $n \in [N]$, of the unitary matrix $\Psi \in \mathbb{C}^{N \times N}$, which represents a suitable orthonormal basis of \mathbb{C}^N , e.g. the Fourier, a wavelet, or the canonical basis, define the admissible structural building blocks. The vector of transform coefficients

$$\boldsymbol{\theta} = \Psi^H \mathbf{x} \quad (2)$$

constitutes a nearly-sparse representation of the high-dimensional vector, if the sorted absolute values of its components decay rapidly. The exact indices of the significant components, which exceed a specified absolute value, however, are typically unknown *a priori*.

The insertions of the nearly-sparse representation (2) and the sensing matrix

$$\mathbf{A} = \Phi \Psi, \quad (3)$$

which is assumed not to contain any zero columns, i.e. $\mathbf{a}_n \in \mathbb{C}^M \setminus \{\mathbf{0}\}$ for all $n \in [N]$, into the underdetermined linear algebraic system (1) yield

$$\mathbf{y}^{(\eta)} = \underbrace{\Phi \Psi}_{=\mathbf{A}} \boldsymbol{\theta} + \boldsymbol{\eta} = \mathbf{A} \boldsymbol{\theta} + \boldsymbol{\eta}. \quad (4)$$

The associated CS problem reads

$$\begin{aligned} &\text{Recover} && \text{nearly-sparse } \boldsymbol{\theta} \in \mathbb{C}^N \\ &\text{subject to} && \|\mathbf{y}^{(\eta)} - \mathbf{A} \boldsymbol{\theta}\|_2 \leq \eta \end{aligned} \quad (5)$$

and the methods for its stable solution coalesce into the sparsity-promoting ℓ_q -minimization method [63, (1.11)] and

(1.12)], [60, (2) and (11)], [42, $(\mathbf{P}_{q,\theta})$]⁴

$$\begin{aligned} \hat{\boldsymbol{\theta}}^{(q,\eta)} \in \arg \min_{\boldsymbol{\theta} \in \mathbb{C}^N} \|\tilde{\boldsymbol{\theta}}\|_q \\ \text{subject to } \|\mathbf{y}^{(\eta)} - \mathbf{A}\tilde{\boldsymbol{\theta}}\|_2 \leq \eta, \end{aligned} \quad (\mathbf{P}_{q,\eta})$$

where the parameter $q \in [0;1]$ determines the type of optimization method. The parameter $q = 1$ induces the convex ℓ_1 -minimization method, whose implementation permits computationally efficient algorithms, whereas the half-open parameter interval $q \in [0;1)$ induces the nonconvex ℓ_q -minimization method, whose global intractability necessitates local approximations.

Multiple sufficient conditions on the sensing matrix (3) ensure the stable recovery of the nearly-sparse representation (2) in the CS problem (5) by the sparsity-promoting ℓ_q -minimization method $(\mathbf{P}_{q,\eta})$. They specify upper bounds for various characteristic measures quantifying the suitability of the sensing matrix (3), e.g. the null space constants [35, Def. 4.21], [63, Def. 1.2], the restricted isometry ratio [42], and the restricted isometry constant (RIC) [38], [64], [65]. The evaluation of these measures for a fixed sensing matrix (3), however, is a computationally-intractable combinatorial problem [66]. Its complexity impedes both the deterministic construction of high-dimensional sensing matrices (3), whose characteristic measures meet the upper bounds, and the verification of the sufficient conditions. In contrast, the evaluation of a characteristic measure named worst-case coherence [35, Def. 5.1] is relatively simple. It loosely bounds from above the RIC [35, Prop. 6.2] and, by its Welch lower bound [35, Thm. 5.7], [36, Lem. 3.7], ensures the restricted isometry property (RIP) for s nonzero components, if the number of observations meets $M \in \Omega(s^2)$. Fortunately, certain types of random sensing matrices (3) also obey the RIP with very high probability, if the number of observations is sufficiently large [35, 6], [60]. Realizations of independent and identically distributed (i.i.d.) random variables governed by certain distributions, e.g. Gaussian or Bernoulli, as entries [67, Thm. 5.2]⁵ and randomly and uniformly chosen scaled rows of a Fourier basis [69, Thm. 3.3], for example, require $M \in \Omega(s \ln(N/s))$ and $M \in \Omega(s \ln^4(N))$ observations, respectively. These orders of growth are almost linear in s and, thus, significantly better than that guaranteed by the worst-case coherence.

In medical imaging, the individual entries of the observation process and, in conjunction with the orthonormal basis, those of the sensing matrix (3) depend on the underlying physical model. Various imaging parameters controlling the instrumentation, however, enable the systematic manipulation of groups of these entries within technologically and physiologically tolerable limits. The randomizations of these degrees of freedom generate sensing matrices (3) with random structures that potentially improve the aforementioned characteristic measures and, consequently, aid in meeting the associated sufficient conditions. In fact, the degrees of freedom in the physical

models underlying magnetic resonance imaging (MRI) [35, 11, 12], [41] and compressed beamforming in UI [70]–[74], for example, specify subsets of scaled Fourier coefficients to be processed. Their random and uniform selection generates the aforementioned random sensing matrix meeting the RIP with relatively few observations. In addition, the introduction of diagonal weighting matrices, whose entries equal the ℓ_2 -norms of the sensing matrix's column vectors $\|\mathbf{a}_n\|_2$ or their reciprocals, into the underdetermined linear algebraic system (4) always enables the ℓ_2 -normalization of the sensing matrix's column vectors without violating the mathematical equivalence. The resulting normalized sensing matrix minimizes both the restricted isometry ratio and the RIC for 1-sparse representations (2) and better conforms with the associated sufficient conditions [35, Prop. 6.2].

The transform point spread function (TPSF) frequently quantifies the coherence of the sensing matrices (3) in medical imaging (cf. e.g. [39], [41]). It equals the mutual correlation coefficient of the column vectors given by [39, (23)], [41, (2)]

$$\text{TPSF}\{\mathbf{A}\}(n_1, n_2) = \frac{\langle \mathbf{a}_{n_1}, \mathbf{a}_{n_2} \rangle}{\|\mathbf{a}_{n_1}\|_2 \|\mathbf{a}_{n_2}\|_2} \quad (6)$$

for all $(n_1, n_2) \in [N]^2$. If the orthonormal basis is canonical, i.e. $\boldsymbol{\Psi} = \mathbf{I}$, the TPSF (6) reduces to the point spread function (PSF) and exclusively quantifies the coherence of the observation process [41]. For $n_1 = n_2$, both column vectors match, and the TPSF (6) trivially attains its maximum absolute value of unity. For $n_1 \neq n_2$, however, both column vectors typically differ, and the absolute value of the TPSF (6) ideally approaches zero with noise-like statistics [39], [41]. These properties, which are referred to as incoherent aliasing, indicate the reliable discrimination of the admissible structural building blocks by the observation process and guide the sparsity-promoting ℓ_q -minimization method $(\mathbf{P}_{q,\eta})$. Owing to the high dimensionality of the sensing matrices (3), practical evaluations of the TPSF (6) usually select one index from the expected support of the nearly-sparse representation (2), i.e. $n_2 \in \text{supp}(\boldsymbol{\theta})$ (cf. e.g. [39, Fig. 1], [41, Figs. 4 and 5]).

III. LINEAR PHYSICAL MODEL FOR THE PULSE-ECHO MEASUREMENT PROCESS

The proposed d -dimensional, $d \in \{2,3\}$, physical model uses the interactions of arbitrary incident waves with the human body to predict the RF voltage signals provided by the instrumentation. The interactions include diffraction, single monopole scattering, and the combined effects of power-law absorption and dispersion. A rigid baffle on the hyperplane $r_d = 0$, which embeds the vibrating faces of the transducer elements and bounds the half-space $r_d > 0$, approximates the complex boundary conditions. The temporal Fourier domain simplifies the mathematical formulation of the model and enables the parallel processing of distinct discrete frequencies in numerical evaluations.

A. Pulse-Echo Measurement Process

The UI system sequentially performs $N_{\text{in}} \in \mathbb{N}$ independent pulse-echo measurements using a planar transducer array (cf.

⁴The first author confirms the validity of the results, which are exclusively stated for \mathbb{R}^N , for \mathbb{C}^N in [64].

⁵The result holds universally under any unitary transform, i.e. the right multiplication of a random observation process by any complex-valued unitary $N_{\text{lat}} \times N_{\text{lat}}$ matrix preserves the RIP [68, 222], [67, Sect. 6].

TABLE II: Geometric and electromechanical parameters of the instrumentation for all $\delta \in [d-1]$, $m \in [N_{\text{el}} - 1]_0$, $l \in \mathbb{L}_{\text{BP}}^{(n)}$.

Symbol	Meaning
$N_{\text{el},\delta}$	Number of elements along the r_δ -axis, $N_{\text{el},\delta} \in \mathbb{N}$
$w_{\text{el},\delta}$	Width of the vibrating faces along the r_δ -axis, $w_{\text{el},\delta} \in \mathbb{R}^+$
$k_{\text{el},\delta}$	Width of the kerfs separating the elements along the r_δ -axis, $k_{\text{el},\delta} \in \mathbb{R}_0^+$
$\Delta r_{\text{el},\delta}$	Element pitch, i.e. constant spacing between the centers of the adjacent vibrating faces along the r_δ -axis, $\Delta r_{\text{el},\delta} = w_{\text{el},\delta} + k_{\text{el},\delta}$
$\mathbf{r}_{\text{el},m}$	Center coordinates of the vibrating faces, $\mathcal{M} = \{\mathbf{r}_{\text{el},m} \in \mathbb{R}^d : \mathbf{r}_{\text{el},m} = \sum_{\delta=1}^{d-1} (m_\delta - M_{\text{el},\delta}) \Delta r_{\text{el},\delta} \mathbf{e}_\delta, m_\delta \in [N_{\text{el},\delta} - 1]_0, m = \mathcal{I}(\mathbf{m}, \mathbf{N}_{\text{el}})\}$, where $M_{\text{el},\delta} = (N_{\text{el},\delta} - 1)/2$ and $\mathcal{I}(\mathbf{m}, \mathbf{N}_{\text{el}}) = \sum_{\delta=1}^{d-1} m_\delta \prod_{k=\delta+1}^{d-1} N_{\text{el},k} + m_{d-1}$
N_{el}	Total number of elements, $N_{\text{el}} = \mathcal{M} = \prod_{\delta=1}^{d-1} N_{\text{el},\delta}$
L_m	Coplanar compact sets specifying the $(d-1)$ -dimensional vibrating faces on the hyperplane $r_d = 0$, $L_m = \prod_{\delta=1}^{d-1} [r_{\text{el},m,\delta} - 0.5w_{\text{el},\delta}; r_{\text{el},m,\delta} + 0.5w_{\text{el},\delta}] \subset \mathbb{R}^{d-1}$
$\chi_{m,l}^{(\text{tx})}$	Transmitter apodization functions accounting for the heterogeneous normal velocities and the acoustic lens, $\chi_{m,l}^{(\text{tx})} : L_m \mapsto \mathbb{C}$
$\chi_{m,l}^{(\text{rx})}$	Receiver apodization functions accounting for the heterogeneous sensitivities and the acoustic lens, $\chi_{m,l}^{(\text{rx})} : L_m \mapsto \mathbb{C}$
$h_{m,l}^{(\text{tx})}$	Transmitter electromechanical transfer functions accounting for the driving circuits, the cables, and the radiating elements, $h_{m,l}^{(\text{tx})} \in \mathbb{C}$
$h_{m,l}^{(\text{rx})}$	Receiver electromechanical transfer functions accounting for the receiving elements, the cables, and the amplifiers, $h_{m,l}^{(\text{rx})} \in \mathbb{C}$

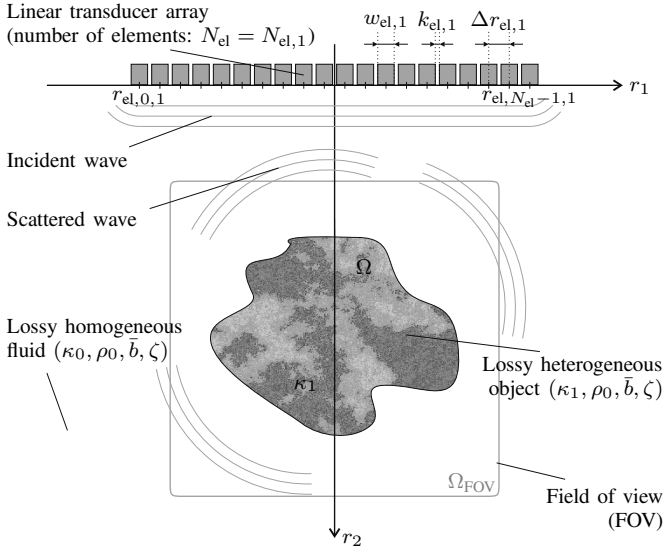


Fig. 1: Pulse-echo measurement process in the two-dimensional Euclidean space, i.e. $d = 2$. A linear transducer array emits a broadband incident wave into a lossy homogeneous fluid with the unperturbed values of the compressibility $\kappa_0 \in \mathbb{R}^+$ and the mass density $\rho_0 \in \mathbb{R}^+$. This wave penetrates an embedded lossy heterogeneous object represented by the bounded set $\Omega \subset \{\mathbf{r} \in \mathbb{R}^d : r_d > 0\}$, and its interactions with the unperturbed compressibility $\kappa_1 : \Omega \mapsto \mathbb{R}^+$ induce a scattered wave. A portion of the latter mechanically excites the faces of the array elements that generate RF voltage signals. These enable the imaging of the specified FOV represented by the bounded set $\Omega_{\text{FOV}} \subset \{\mathbf{r} \in \mathbb{R}^d : r_d > 0\}$.

Fig. 1 and Table II). Each measurement begins at the time instant $t = 0$ and triggers the concurrent recording of the RF voltage signals $\tilde{u}_m^{(\text{rx},n)} : \mathbb{T}_{\text{rec}}^{(n)} \mapsto \mathbb{R}$ generated by all array elements $m \in [N_{\text{el}} - 1]_0$ in the specified time interval

$$\mathbb{T}_{\text{rec}}^{(n)} = [t_{\text{lb}}^{(n)}; t_{\text{ub}}^{(n)}], \quad (7)$$

where $t_{\text{lb}}^{(n)} \in \mathbb{R}_0^+$ and $t_{\text{ub}}^{(n)} > t_{\text{lb}}^{(n)}$ denote its lower and upper bounds, respectively. The finite recording times $T_{\text{rec}}^{(n)} = |\mathbb{T}_{\text{rec}}^{(n)}| = t_{\text{ub}}^{(n)} - t_{\text{lb}}^{(n)}$ enable the representation of these signals by the Fourier series (cf. e.g. [75, (2.2.1/2)], [76, (2.12/13)])

$$\tilde{u}_m^{(\text{rx},n)}(t) = u_{m,0}^{(\text{rx},n)} + 2\text{Re}\left\{\sum_{l=1}^{\infty} u_{m,l}^{(\text{rx},n)} e^{j\omega_l t}\right\} \quad (8a)$$

for all $(n, m) \in [N_{\text{in}} - 1]_0 \times [N_{\text{el}} - 1]_0$, where $\omega_l = 2\pi fl = 2\pi l/T_{\text{rec}}^{(n)}$ denote the discrete angular frequencies, and

$$u_{m,l}^{(\text{rx},n)} = \frac{1}{T_{\text{rec}}^{(n)}} \int_{\mathbb{T}_{\text{rec}}^{(n)}} \tilde{u}_m^{(\text{rx},n)}(t) e^{-j\omega_l t} dt \quad (8b)$$

are the complex-valued coefficients, whose conjugate even symmetry renders the negative frequency indices redundant.

The bandpass characters of the recorded RF voltage signals, which are described by the lower and upper frequency bounds $f_{\text{lb}}^{(n)} \in \mathbb{R}^+$ and $f_{\text{ub}}^{(n)} \geq f_{\text{lb}}^{(n)} + 1/T_{\text{rec}}^{(n)}$, respectively, define the sets of relevant discrete frequencies

$$\mathbb{F}_{\text{BP}}^{(n)} = \left\{f_l \in \mathbb{R}^+ : f_l = \frac{l}{T_{\text{rec}}^{(n)}}, l \in \mathbb{L}_{\text{BP}}^{(n)}\right\} \quad (9a)$$

for all $n \in [N_{\text{in}} - 1]_0$, where the admissible index sets are

$$\mathbb{L}_{\text{BP}}^{(n)} = \left\{l \in \mathbb{N} : l_{\text{lb}}^{(n)} \leq l \leq l_{\text{ub}}^{(n)}\right\} \quad (9b)$$

with the lower and upper bounds

$$l_{\text{lb}}^{(n)} = \lceil T_{\text{rec}}^{(n)} f_{\text{lb}}^{(n)} \rceil \quad \text{and} \quad l_{\text{ub}}^{(n)} = \lfloor T_{\text{rec}}^{(n)} f_{\text{ub}}^{(n)} \rfloor, \quad (9c)$$

respectively. These enable the truncation of each Fourier series (8a), where, defining the effective bandwidths $B_u^{(n)} = f_{\text{ub}}^{(n)} - f_{\text{lb}}^{(n)}$, the number of relevant discrete frequencies approximates the effective time-bandwidth products

$$N_{f,\text{BP}}^{(n)} = |\mathbb{L}_{\text{BP}}^{(n)}| = l_{\text{ub}}^{(n)} - l_{\text{lb}}^{(n)} + 1 \approx T_{\text{rec}}^{(n)} B_u^{(n)} \quad (10)$$

for all $n \in [N_{\text{in}} - 1]_0$, and the representation of each pulse-echo measurement by $N_{\text{el}} N_{f,\text{BP}}^{(n)}$ coefficients (8b).

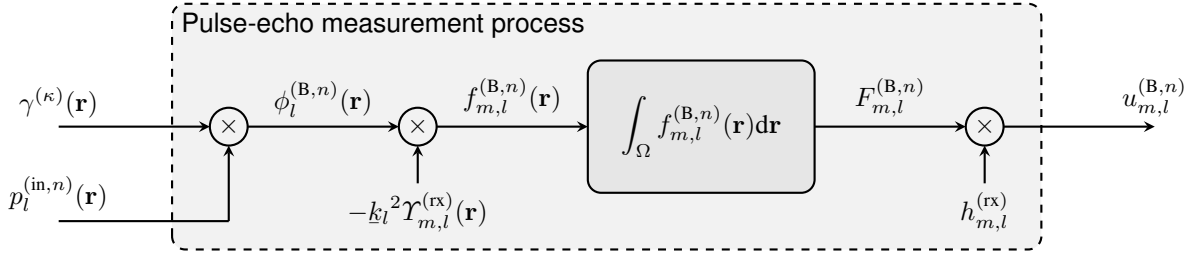


Fig. 2: Block diagram of the pulse-echo measurement process (17b). Given the incident acoustic pressure fields $p_l^{(in,n)} : \mathbb{R}^d \mapsto \mathbb{C}$, which satisfy the Helmholtz equations (15), the Born approximation linearly maps the compressibility fluctuations (11) to the recorded RF voltage signals (17).

B. Acoustic Model for Human Soft Tissues

Medical UI usually models soft tissue structures⁶ as quiescent, lossless, and heterogeneous fluids that linearly propagate small-amplitude disturbances of the stationary state as longitudinal waves [78]–[81]. The relevant acoustic material parameters are the unperturbed values of both the compressibility and the mass density, which are typically normalized by their spatial averages $\kappa_0 \in \mathbb{R}^+$ and $\rho_0 \in \mathbb{R}^+$, respectively [78], [80], [81]. For the sake of simplicity, the proposed model considers a homogeneous unperturbed mass density. The relative spatial fluctuations in the unperturbed compressibility read (cf. Fig. 1)

$$\gamma^{(\kappa)}(\mathbf{r}) = \begin{cases} 1 - \kappa_1(\mathbf{r})/\kappa_0 & \text{for } \mathbf{r} \in \Omega, \\ 0 & \text{for } \mathbf{r} \notin \Omega. \end{cases} \quad (11)$$

The spatial amplitude absorption coefficient $\alpha_l \in \mathbb{R}_0^+$, which is commonly neglected, obeys the power law (cf. e.g. [82, Sect. 4.3.8], [83, (4)])

$$\alpha_l = \bar{b} |\omega_l|^\zeta \quad (12)$$

in the entire Euclidean space for all relevant discrete frequencies $l \in \mathbb{L}_{\text{BP}}^{(n)}$, where the parameter pair $(\bar{b}, \zeta) \in \mathbb{R}_0^+ \times \mathbb{R}_0^+$ depends on both the specific type of tissue and the ambient conditions. The exponent ζ usually ranges between 1.0 and 1.5 [84], [82, 112], [83]. Given reference values of the angular frequency $\omega_{\text{ref}} \in \mathbb{R}^+$ and the associated phase velocity $c_{\text{ref}} \in \mathbb{R}^+$, the complex-valued wavenumber [85], [86]

$$k_l = \underbrace{\frac{\omega_l}{c_{\text{ref}}}}_{=\beta_l = \omega_l/c_l} + \beta_{\text{E,ref},l} - j \underbrace{\bar{b} |\omega_l|^\zeta}_{=\alpha_l}, \quad (13a)$$

where the phase term $\beta_l \in \mathbb{R}$ sums the real-valued wavenumber $k_{\text{ref},l} = \omega_l/c_{\text{ref}}$ and the excess dispersion term

$$\beta_{\text{E,ref},l} = \begin{cases} -2\bar{b}\omega_l \ln(|\omega_l/\omega_{\text{ref}}|)/\pi & \text{for } \zeta = 1, \\ \bar{b} \tan(\zeta\pi/2)\omega_l (|\omega_l|^{\zeta-1} - |\omega_{\text{ref}}|^{\zeta-1}) & \text{else,} \end{cases} \quad (13b)$$

combines power-law absorption with anomalous dispersion.

C. Recorded Radio Frequency Voltage Signals

The array elements transduce the compressive blocked forces exerted by the free-space scattered acoustic pressure fields $p_l^{(\text{sc},n)} : \mathbb{R}^d \mapsto \mathbb{C}$ on their planar faces $L_m \subset \mathbb{R}^{d-1}$ into the RF voltage signals (cf. e.g. [87, Sect. 9.2], [78], [80], [88])

$$u_{m,l}^{(\text{rx},n)} = 2h_{m,l}^{(\text{rx})} \int_{L_m} \chi_{m,l}^{(\text{rx})}(\mathbf{r}_\rho) p_l^{(\text{sc},n)}(\mathbf{r}_\rho, 0) d\mathbf{r}_\rho \quad (14)$$

for all $(n, l, m) \in [N_{\text{in}} - 1]_0 \times \mathbb{L}_{\text{BP}}^{(n)} \times [N_{\text{el}} - 1]_0$, where $h_{m,l}^{(\text{rx})} \in \mathbb{C}$ denote the electromechanical transfer functions and $\chi_{m,l}^{(\text{rx})} : L_m \mapsto \mathbb{C}$ are the apodization functions (cf. Table II).

The Born approximation, which drives the established image recovery methods in ultrafast UI [6]–[10], [88], uses the incident acoustic pressure fields $p_l^{(\text{in},n)} : \mathbb{R}^d \mapsto \mathbb{C}$ induced by the transducer array in the homogeneous fluid and governed by the Helmholtz equations (cf. e.g. [21, (6.4)], [22, 47], [23, (30)])

$$(\Delta + k_l^2) p_l^{(\text{in},n)}(\mathbf{r}) = 0 \quad (15)$$

to estimate the free-space scattered acoustic pressure fields as (cf. e.g. [21, (6.53)], [22, (3.16)], [23, (40)], [89, (57)])

$$p_l^{(\text{sc},n)}(\mathbf{r}) \approx k_l^2 \int_{\Omega} \gamma^{(\kappa)}(\mathbf{r}') p_l^{(\text{in},n)}(\mathbf{r}') g_l(\mathbf{r} - \mathbf{r}') d\mathbf{r}' \quad (16)$$

for all $(n, l) \in [N_{\text{in}} - 1]_0 \times \mathbb{L}_{\text{BP}}^{(n)}$, where the outgoing free-space Green's functions (A.55) account for diffraction and monopole scattering (cf. Appendix I). The resulting single scattering is valid for weakly-scattering heterogeneous objects, i.e. $|p_l^{(\text{sc},n)}(\mathbf{r})| \ll |p_l^{(\text{in},n)}(\mathbf{r})|$ for all $\mathbf{r} \in \Omega$. These feature both small absolute values of the compressibility fluctuations (11) and small acoustic sizes [90], [89, 708].

The Born approximation of the scattered acoustic pressure fields (16) estimates the recorded RF voltage signals (14) as the Fredholm integral equations of the first kind

$$u_{m,l}^{(\text{rx},n)} \approx u_{m,l}^{(\text{B},n)} = \Phi_{m,l} [p_l^{(\text{in},n)}, \gamma^{(\kappa)}] \quad (17a)$$

for all $(n, l, m) \in [N_{\text{in}} - 1]_0 \times \mathbb{L}_{\text{BP}}^{(n)} \times [N_{\text{el}} - 1]_0$, where the

⁶The anatomic term “soft tissue” refers to tendons, ligaments, skin, nerves, muscle, fat, fibrous tissue, blood vessels, or other supporting tissue of the body [77, “soft tissue”]. In the context of UI, however, the term additionally includes organs like liver, kidney, thyroid, brain, and the heart.

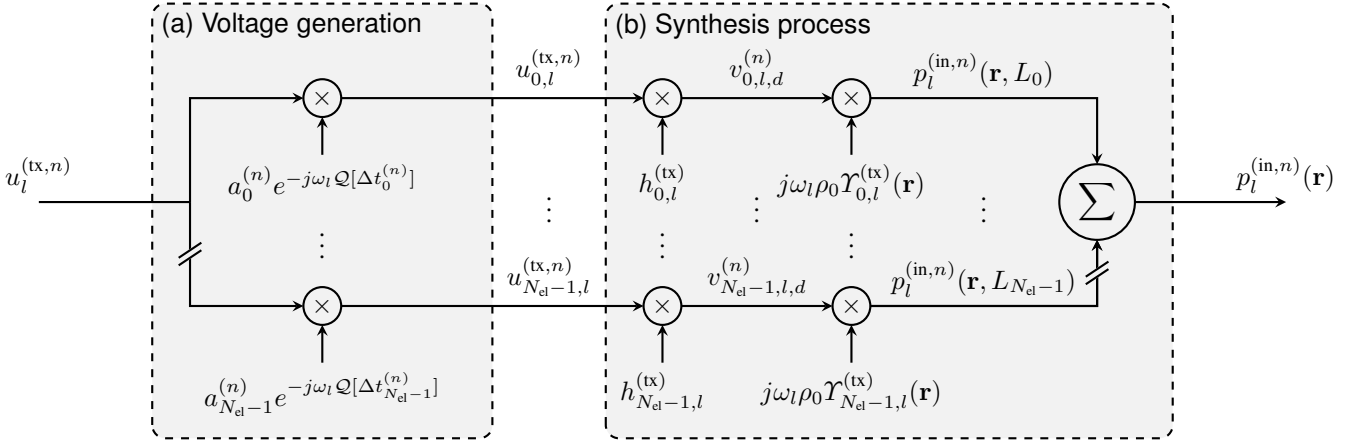


Fig. 3: Block diagram of the syntheses of the incident waves. Given the apodization weights $a_m^{(n)} \in \mathbb{R}$ and the time delays $\Delta t_m^{(n)} \in \mathbb{R}_0^+$, the voltage generation (cf. (a)) maps the reference voltage signals $u_l^{(tx,n)} \in \mathbb{C}$ to the excitation voltages (20). These voltages control the synthesis process (cf. (b)) that superimposes the quasi- $(d-1)$ -spherical waves emitted by the individual elements of the planar transducer array (18) to form various types of incident waves (19).

properties of the pulse-echo measurement process

$$\Phi_{m,l}[p_l^{(in,n)}, \gamma^{(\kappa)}] = -k_l^2 h_{m,l}^{(rx)} \int_{\Omega} \gamma^{(\kappa)}(\mathbf{r}) p_l^{(in,n)}(\mathbf{r}) \Upsilon_{m,l}^{(rx)}(\mathbf{r}) d\mathbf{r} \quad (17b)$$

significantly depend on the incident waves (cf. Fig. 2), and the apodized spatial receive functions

$$\Upsilon_{m,l}^{(rx)}(\mathbf{r}) = -2 \int_{L_m} \chi_{m,l}^{(rx)}(\mathbf{r}'_{\rho}) g_l(\mathbf{r}'_{\rho} - \mathbf{r}_{\rho}, -r_d) d\mathbf{r}'_{\rho}, \quad (17c)$$

which correspond to the spatial impulse responses in the time domain [79], [80], characterize the anisotropic directivities of the planar faces.

IV. SYNTHESIS OF THE INCIDENT WAVES

Modern programmable UI systems synthesize various types of incident waves by superimposing the weighted and delayed waves emitted by the individual elements of the planar transducer array. These quasi- $(d-1)$ -spherical waves, which are referred to as quasi-cylindrical waves (QCWs) in the two-dimensional Euclidean space, i.e. $d=2$, reflect the anisotropic directivities of the vibrating faces and, thus, differ from the outgoing $(d-1)$ -spherical waves induced by isotropic point sources. The LTI measurement process superimposes their pulse echoes such that each incident wave projects a complete SA acquisition sequence on a single pulse-echo measurement.

The highly probable satisfaction of the RIP by certain types of random sensing matrices for relatively few observations (cf. Sect. II) motivates the randomization of the apodization weights and the time delays. Unlike the steered quasi-plane waves (QPWs), which practically implement the steered PWs in ultrafast UI, the resulting random waves decorrelate the pulse echoes of the lossy heterogeneous object's admissible structural building blocks. They strongly compress both the acquisition time and the data volume of a complete SA acquisition sequence and potentially improve the image recovery.

A. Superpositions of Quasi- $(d-1)$ -Spherical Waves

The array elements transduce their excitation voltages $u_{m,l}^{(tx,n)} \in \mathbb{C}$ into the homogeneous normal velocities on their planar faces $L_m \subset \mathbb{R}^{d-1}$ [78], [88]. The Rayleigh-Sommerfeld diffraction equations uniquely solve the Helmholtz equations (15) for these boundary conditions (cf. e.g. [21, (2.48)], [89, (13) of §8.11]) and represent the individual quasi- $(d-1)$ -spherical waves by the incident acoustic pressure fields

$$p_l^{(in,n)}(\mathbf{r}, L_m) = j\omega_l \rho_0 h_{m,l}^{(tx)} u_{m,l}^{(tx,n)} \Upsilon_{m,l}^{(tx)}(\mathbf{r}) \quad (18a)$$

for all $(n, l, m) \in [N_{in}-1]_0 \times \mathbb{L}_{BP}^{(n)} \times [N_{el}-1]_0$, where $h_{m,l}^{(tx)} \in \mathbb{C}$ denote the electromechanical transfer functions, and the apodized spatial transmit functions

$$\Upsilon_{m,l}^{(tx)}(\mathbf{r}) = -2 \int_{L_m} \chi_{m,l}^{(tx)}(\mathbf{r}'_{\rho}) g_l(\mathbf{r}_{\rho} - \mathbf{r}'_{\rho}, r_d) d\mathbf{r}'_{\rho} \quad (18b)$$

characterize the anisotropic directivities of the vibrating faces for all $r_d > 0$, similar to the apodized spatial receive functions (17c) (cf. Table II). Their superpositions represent the incident waves by the acoustic pressure fields

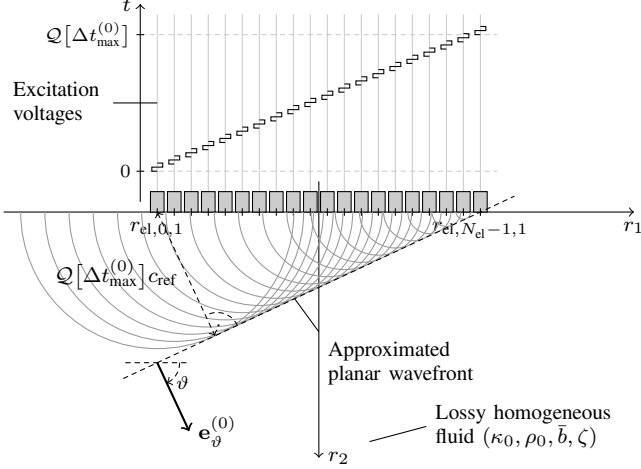
$$p_l^{(in,n)}(\mathbf{r}) = j\omega_l \rho_0 \sum_{m=0}^{N_{el}-1} h_{m,l}^{(tx)} u_{m,l}^{(tx,n)} \Upsilon_{m,l}^{(tx)}(\mathbf{r}) \quad (19)$$

for all $(n, l) \in [N_{in}-1]_0 \times \mathbb{L}_{BP}^{(n)}$, where the excitation voltages determine the synthesized types of incident waves (cf. Fig. 3(b)).

B. Types of Incident Waves

The generation of the excitation voltages typically applies quantized apodization weights $a_m^{(n)} \in \mathbb{R}$ and time delays $\Delta t_m^{(n)} \in \mathbb{R}_0^+$ to the reference voltage signals $u_l^{(tx,n)} \in \mathbb{C}$, whose electric energies are constant for all $n \in [N_{in}-1]_0$. Apodization weights of unity absolute values then ensure the energy equivalence of the incident waves and only require the

(a) Steered quasi-plane wave



(b) Realization of a proposed type of random wave

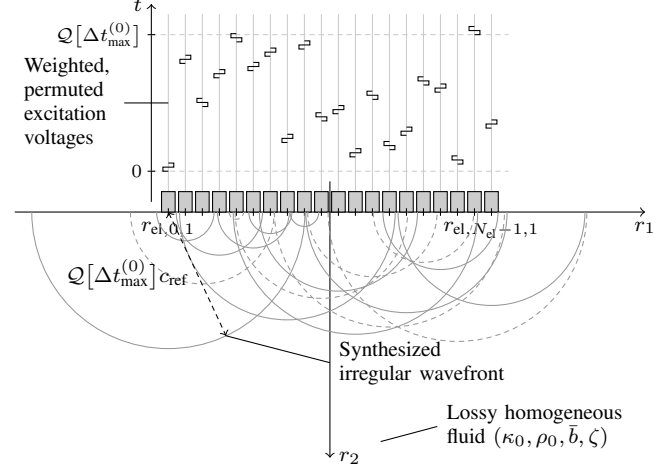


Fig. 4: Syntheses of a steered quasi-plane wave (QPW) (cf. (a)) and a proposed type of random wave (cf. (b)) in the two-dimensional Euclidean space, i.e. $d = 2$. The gray semicircles represent the individual quasi-cylindrical waves (QCWs) emitted by each element of the linear transducer array. Their dashed variants indicate negatively-apodized QCWs, i.e. $a_m^{(0)} = -1$ in (24), whereas their solid variants indicate positively-apodized QCWs, i.e. $a_m^{(0)} = 1$ in (21) and (24). Their distinct radii reflect the time delays in (21) and (24), whose maxima equal $\Delta t_{\max}^{(0)} = \max_{m \in [N_{\text{el}} - 1]_0} \{\Delta t_m^{(0)}\} = (N_{\text{el}} - 1)\Delta r_{\text{el},1}|e_{\vartheta,1}^{(0)}|/c_{\text{ref}}$. The dashed black line indicates the approximated planar wavefront. The black arrow shows the preferred direction of propagation.

quantization of the time delays. For a clock signal with the frequency $f_{\text{clk}} = 1/T_{\text{clk}} \in \mathbb{R}^+$ and the quantization operator

$$\mathcal{Q}[\Delta t_m^{(n)}] = \lceil \Delta t_m^{(n)} f_{\text{clk}} \rceil T_{\text{clk}}, \quad (20a)$$

the generated excitation voltages are

$$u_{m,l}^{(\text{tx},n)} = u_l^{(\text{tx},n)} a_m^{(n)} e^{-j\omega_l \mathcal{Q}[\Delta t_m^{(n)}]} \quad (20b)$$

for all $(n, l, m) \in [N_{\text{in}} - 1]_0 \times \mathbb{L}_{\text{BP}}^{(n)} \times [N_{\text{el}} - 1]_0$, where the asymmetric brackets denote the rounding to the nearest integer and the complex exponential functions induce the phase shifts corresponding to the time delays (cf. Fig. 3(a)).

1) *Steered Quasi-Plane Waves*: Steered QPWs denote the approximations of steered PWs synthesized by the UI system. The time delays in the excitation voltages (20) depend affinely on the center coordinates of the vibrating faces on each coordinate axis, whereas all apodization weights equal unity. These specifications yield

$$a_m^{(n)} = 1 \quad \text{and} \quad \Delta t_m^{(n)} = \frac{\langle \mathbf{r}_{\text{el},m} - \mathbf{r}_{\text{ref}}^{(n)}, \mathbf{e}_{\vartheta}^{(n)} \rangle}{c_{\text{ref}}} \quad (21a)$$

for all $(n, m) \in [N_{\text{in}} - 1]_0 \times [N_{\text{el}} - 1]_0$, where $\mathbf{r}_{\text{el},m} \in \mathcal{M}$ denote the center coordinates of the vibrating faces, $\mathbf{e}_{\vartheta}^{(n)} = (e_{\vartheta,1}^{(n)}, \dots, e_{\vartheta,d}^{(n)})^T \in \mathbb{S}_+^{d-1}$ indicate the preferred directions of propagation, and $\mathbf{r}_{\text{ref}}^{(n)} = (r_{\text{ref},1}^{(n)}, \dots, r_{\text{ref},d-1}^{(n)}, 0)^T$ are the reference positions with the components

$$r_{\text{ref},\delta}^{(n)} = \begin{cases} -M_{\text{el},\delta} \Delta r_{\text{el},\delta} & \text{for } e_{\vartheta,\delta}^{(n)} \geq 0, \\ M_{\text{el},\delta} \Delta r_{\text{el},\delta} & \text{for } e_{\vartheta,\delta}^{(n)} < 0, \end{cases} \quad (21b)$$

for all $\delta \in [d - 1]$ (cf. Table II). The latter ensure the nonnegativity of the time delays and, thus, the causality of the voltage generation. The finite number of elements

and their anisotropic directivities limit the accuracies of the approximations to bounded areas in front of the array (cf. Fig. 4(a)).

2) *Randomly-Apodized Quasi-(d-1)-Spherical Waves*: The first type of random wave uses realizations of i.i.d. random variables $\Lambda_m^{(n)}$ as the apodization weights in the excitation voltages (20), whereas all time delays equal zero. These specifications yield

$$a_m^{(n)} = \Lambda_m^{(n)} \quad \text{and} \quad \Delta t_m^{(n)} = 0 \quad (22a)$$

for all $(n, m) \in [N_{\text{in}} - 1]_0 \times [N_{\text{el}} - 1]_0$. The Bernoulli distribution

$$\Lambda_m^{(n)} = \begin{cases} 1 & \text{with probability 0.5,} \\ -1 & \text{with probability 0.5,} \end{cases} \quad (22b)$$

exclusively requires inverting buffer amplifiers and, thus, enables a relatively simple hardware realization.

3) *Randomly-Delayed Quasi-(d-1)-Spherical Waves*: The second type of random wave assigns random permutations of uniformly spaced time instants to the time delays in the excitation voltages (20), whereas all apodization weights equal unity. These specifications yield

$$a_m^{(n)} = 1 \quad \text{and} \quad \Delta t_m^{(n)} = \Pi_m^{(n)}([N_{\text{el}} - 1]_0) T_{\text{inc}}^{(n)} \quad (23a)$$

for all $(n, m) \in [N_{\text{in}} - 1]_0 \times [N_{\text{el}} - 1]_0$, where $\Pi_m^{(n)}([N_{\text{el}} - 1]_0)$ denote the elements of index m in random permutations of the set $[N_{\text{el}} - 1]_0$ and $T_{\text{inc}}^{(n)} \in \mathbb{R}^+$ are fixed time periods. The latter significantly influence the properties of the superpositions and, consequently, those of the pulse-echo measurement process (17b).

In the limiting cases $T_{\text{inc}}^{(n)} \rightarrow 0+$, the superpositions converge to steered QPWs with the preferred directions of

propagation $\mathbf{e}_\vartheta^{(n)} = \mathbf{e}_d$, because the apodization weights and the time delays in (23a) converge to those in (21). The specific fixed time periods

$$\begin{aligned} T_{\text{inc}}^{(n)} &= \frac{1}{N_{\text{el}} - 1} \max_{m \in [N_{\text{el}} - 1]_0} \left\{ \frac{\langle \mathbf{r}_{\text{el},m} - \mathbf{r}_{\text{ref}}^{(n)}, \mathbf{e}_\vartheta^{(n)} \rangle}{c_{\text{ref}}} \right\} \\ &= \frac{1}{N_{\text{el}} - 1} \sum_{\delta=1}^{d-1} (N_{\text{el},\delta} - 1) \frac{\Delta r_{\text{el},\delta} |e_{\vartheta,\delta}^{(n)}|}{c_{\text{ref}}} \end{aligned} \quad (23b)$$

result in the syntheses times of the steered QPWs. In the two-dimensional Euclidean space, i.e. $d = 2$, they simplify to $T_{\text{inc}}^{(n)} = \Delta r_{\text{el},1} |e_{\vartheta,1}^{(n)}| / c_{\text{ref}}$ and induce random permutations of the time delays specified for the steered QPWs in (21).

4) *Randomly-Apodized and Randomly-Delayed Quasi-(d-1)-Spherical Waves*: The third type of random wave combines realizations of i.i.d. random variables $\Lambda_m^{(n)}$ as the apodization weights with random permutations of uniformly spaced time instants as the time delays in the excitation voltages (20). These specifications yield

$$a_m^{(n)} = \Lambda_m^{(n)} \quad \text{and} \quad \Delta t_m^{(n)} = \Pi_m^{(n)} ([N_{\text{el}} - 1]_0) T_{\text{inc}}^{(n)} \quad (24)$$

for all $(n, m) \in [N_{\text{in}} - 1]_0 \times [N_{\text{el}} - 1]_0$, where the Bernoulli distribution (22b) is combined with the fixed time periods (23b). They result in irregular wavefronts that do not resemble any common models (cf. Fig. 4(b)).

V. IMAGE RECOVERY BASED ON COMPRESSED SENSING

The proposed method aims at recovering the compressibility fluctuations (11) inside the specified FOV (cf. Fig. 1) from only a few recordings of the RF voltage signals, which are modeled by their Born approximation (17). The numerical solution of this linear inverse scattering problem (ISP) necessitates suitable spatial discretizations of the physical models. These discretizations, however, result in an ill-conditioned and, for only a few sequential pulse-echo measurements, typically underdetermined dense linear algebraic system (1) that does not support any direct solution. The proposed method circumvents this difficulty by reformulating the discretized linear ISP as an instance of the CS problem (5). Postulating the existence of a nearly-sparse representation of the discretized compressibility fluctuations in a known orthonormal basis (2), the sparsity-promoting ℓ_q -minimization method ($\mathbf{P}_{q,\eta}$) ensures its stable recovery if the sensing matrix (3) meets one of the sufficient conditions (cf. Sect. II).

A. Spatial Discretizations of the Physical Models

Two types of regular grids emulate the geometries and the spatial heterogeneities of the vibrating faces and the FOV containing the lossy heterogeneous object (cf. Table III). The apodization functions (cf. Table II) and the compressibility

fluctuations (11) are discretized as

$$\chi_{m,l}^{(\text{tx})}(\mathbf{r}_\rho) = \Delta A \sum_{\nu=0}^{N_{\text{mat}}-1} \chi_{m,\nu,l}^{(\text{tx})} \delta[\mathbf{r}_\rho - \mathbf{r}_{\text{mat},\nu,\rho}^{(m)}], \quad (25a)$$

$$\chi_{m,l}^{(\text{rx})}(\mathbf{r}_\rho) = \Delta A \sum_{\nu=0}^{N_{\text{mat}}-1} \chi_{m,\nu,l}^{(\text{rx})} \delta[\mathbf{r}_\rho - \mathbf{r}_{\text{mat},\nu,\rho}^{(m)}], \quad (25b)$$

$$\gamma_i^{(\kappa)}(\mathbf{r}) = \Delta V \sum_{i=0}^{N_{\text{lat}}-1} \gamma_i^{(\kappa)} \delta(\mathbf{r} - \mathbf{r}_{\text{lat},i}), \quad (25c)$$

where $\chi_{m,\nu,l}^{(\text{tx})} = \chi_{m,l}^{(\text{tx})}[\mathbf{r}_{\text{mat},\nu,\rho}^{(m)}]$, $\chi_{m,\nu,l}^{(\text{rx})} = \chi_{m,l}^{(\text{rx})}[\mathbf{r}_{\text{mat},\nu,\rho}^{(m)}]$, and $\gamma_i^{(\kappa)} = \gamma^{(\kappa)}(\mathbf{r}_{\text{lat},i})$ denote their regular samples for all $(m, \nu, l) \in [N_{\text{el}} - 1]_0 \times [N_{\text{mat}} - 1]_0 \times \mathbb{L}_{\text{BP}}^{(n)}$ or all $i \in [N_{\text{lat}} - 1]_0$.

B. Computations of the Incident Acoustic Pressure Fields

The insertions of the apodized spatial transmit functions (18b) and the discretized transmitter apodization functions (25a) into the incident acoustic pressure fields (19) yield the discretizations

$$\begin{aligned} p_l^{(\text{in},n)}(\mathbf{r}_{\text{lat},i}) &= -j2\omega_l \rho_0 \Delta A \sum_{m=0}^{N_{\text{el}}-1} h_{m,l}^{(\text{tx})} u_{m,l}^{(\text{tx},n)} \\ &\times \sum_{\nu=0}^{N_{\text{mat}}-1} \chi_{m,\nu,l}^{(\text{tx})} g_l[\mathbf{r}_{\text{lat},i} - \mathbf{r}_{\text{mat},\nu}^{(m)}] \end{aligned} \quad (26)$$

for all $(n, l, i) \in [N_{\text{in}} - 1]_0 \times \mathbb{L}_{\text{BP}}^{(n)} \times [N_{\text{lat}} - 1]_0$, where the acoustic energy, which includes all sequential pulse-echo measurements and all relevant discrete frequencies, equals

$$E^{(\text{in})}(\mathbf{r}_{\text{lat},i}) = \sum_{n=0}^{N_{\text{in}}-1} \sum_{l \in \mathbb{L}_{\text{BP}}^{(n)}} |p_l^{(\text{in},n)}(\mathbf{r}_{\text{lat},i})|^2 \quad (27)$$

for all $i \in [N_{\text{lat}} - 1]_0$.

C. Linear System Induced by the Born Approximation

With the discretized versions of the receiver apodization functions (25b) and the compressibility fluctuations (25c), the Born approximation of the recorded RF voltage signals (17) yields the linear algebraic equations

$$u_{m,l}^{(\text{rx},n)} \approx u_{m,l}^{(\text{B},n)} = \sum_{i=0}^{N_{\text{lat}}-1} \phi_{m,l,i} [p_l^{(\text{in},n)}] \gamma_i^{(\kappa)} \quad (28a)$$

for all $(n, l, m) \in [N_{\text{in}} - 1]_0 \times \mathbb{L}_{\text{BP}}^{(n)} \times [N_{\text{el}} - 1]_0$, where the coefficients satisfy

$$\begin{aligned} \phi_{m,l,i} [p_l^{(\text{in},n)}] &= 2k_l^2 \Delta A \Delta V h_{m,l}^{(\text{rx})} p_l^{(\text{in},n)}(\mathbf{r}_{\text{lat},i}) \\ &\times \sum_{\nu=0}^{N_{\text{mat}}-1} \chi_{m,\nu,l}^{(\text{rx})} g_l[\mathbf{r}_{\text{mat},\nu}^{(m)} - \mathbf{r}_{\text{lat},i}], \end{aligned} \quad (28b)$$

and the number of observations equals

$$N_{\text{obs}} = N_{\text{el}} \sum_{n=0}^{N_{\text{in}}-1} N_{f,\text{BP}}^{(n)} \quad (29)$$

TABLE III: Geometric parameters of the spatial discretizations for all $\delta \in [d-1]$, $\zeta \in [d]$, $m \in [N_{\text{el}}-1]$.

Symbol	Meaning
$N_{\text{mat},\delta}$	Number of grid points per vibrating face along the r_δ -axis, $N_{\text{mat},\delta} \in \mathbb{N}$
$\Delta r_{\text{mat},\delta}$	Constant spacing between the adjacent grid points on each vibrating face along the r_δ -axis, $\Delta r_{\text{mat},\delta} = w_{\text{el},\delta}/N_{\text{mat},\delta}$
$\mathbf{r}_{\text{mat},\nu}^{(m)}$	Coordinates of the grid points on each vibrating face, $\mathcal{V}_m = \{\mathbf{r}_{\text{mat},\nu}^{(m)} \in \mathbb{R}^d : \mathbf{r}_{\text{mat},\nu}^{(m)} = \mathbf{r}_{\text{el},m} + \sum_{\delta=1}^{d-1} (\nu_\delta - M_{\text{mat},\delta}) \Delta r_{\text{mat},\delta} \mathbf{e}_\delta, \nu_\delta \in [N_{\text{mat},\delta} - 1]_0, \nu = \mathcal{I}(\nu, \mathbf{N}_{\text{mat}})\}$, where $M_{\text{mat},\delta} = (N_{\text{mat},\delta} - 1)/2$ and $\mathcal{I}(\nu, \mathbf{N}_{\text{mat}}) = \sum_{\delta=1}^{d-2} \nu_\delta \prod_{k=\delta+1}^{d-1} N_{\text{mat},k} + \nu_{d-1}$
N_{mat}	Total number of grid points per vibrating face, $N_{\text{mat}} = \mathcal{V}_m = \prod_{\delta=1}^{d-1} N_{\text{mat},\delta}$
ΔA	$(d-1)$ -dimensional surface element, $\Delta A = \prod_{\delta=1}^{d-1} \Delta r_{\text{mat},\delta}$
$N_{\text{lat},\zeta}$	Number of grid points in the FOV along the r_ζ -axis, $N_{\text{lat},\zeta} \in \mathbb{N}$
$\Delta r_{\text{lat},\zeta}$	Constant spacing between the adjacent grid points in the FOV along the r_ζ -axis, $\Delta r_{\text{lat},\zeta} \in \mathbb{R}^+$
$\mathbf{r}_{\text{lat},0}$	Offset of the grid points in the FOV, $\mathbf{r}_{\text{lat},0} \in \mathbb{R}^{d-1} \times \mathbb{R}^+$
$\mathbf{r}_{\text{lat},i}$	Coordinates of the grid points in the FOV, $\mathcal{L} = \{\mathbf{r}_{\text{lat},i} \in \mathbb{R}^d : \mathbf{r}_{\text{lat},i} = \mathbf{r}_{\text{lat},0} + \sum_{\zeta=1}^d i_\zeta \Delta r_{\text{lat},\zeta} \mathbf{e}_\zeta, i_\zeta \in [N_{\text{lat},\zeta} - 1]_0, i = \mathcal{I}(i, \mathbf{N}_{\text{lat}})\}$, where $\mathcal{I}(i, \mathbf{N}_{\text{lat}}) = \sum_{\zeta=1}^{d-1} i_\zeta \prod_{k=\zeta+1}^d N_{\text{lat},k} + i_d$
N_{lat}	Total number of grid points in the FOV, $N_{\text{lat}} = \mathcal{L} = \prod_{\zeta=1}^d N_{\text{lat},\zeta}$
ΔV	d -dimensional volume element, $\Delta V = \prod_{\zeta=1}^d \Delta r_{\text{lat},\zeta}$

Stacking the regular samples in the discretized compressibility fluctuations (25c) for all grid points into the complex-valued⁷ $N_{\text{lat}} \times 1$ vector

$$\boldsymbol{\gamma}^{(\kappa)} = \left[\gamma_0^{(\kappa)} \quad \dots \quad \gamma_{N_{\text{lat}}-1}^{(\kappa)} \right]^T \quad (30)$$

and the recorded RF voltage signals (8b) and their Born approximation (28) into the complex-valued $N_{\text{obs}} \times 1$ vectors

$$\mathbf{u}^{(\text{rx})} = \underset{n=0}{\text{vcat}} \underset{l \in \mathbb{L}_{\text{BP}}^{(n)}}{\text{vcat}} \underset{m=0}{\text{vcat}} u_{m,l}^{(\text{rx},n)}, \quad (31a)$$

$$\mathbf{u}^{(\text{B})} = \underset{n=0}{\text{vcat}} \underset{l \in \mathbb{L}_{\text{BP}}^{(n)}}{\text{vcat}} \underset{m=0}{\text{vcat}} u_{m,l}^{(\text{B},n)}, \quad (31b)$$

respectively, the complex-valued $N_{\text{obs}} \times N_{\text{lat}}$ matrix

$$\Phi[p^{(\text{in})}] = \underset{n=0}{\text{vcat}} \underset{l \in \mathbb{L}_{\text{BP}}^{(n)}}{\text{vcat}} \underset{m=0}{\text{vcat}} \underset{i=0}{\text{hcat}} \phi_{m,l,i}[p_l^{(\text{in},n)}], \quad (31c)$$

represents the pulse-echo measurement process and defines the ill-conditioned, and, for only a few sequential measurements, typically underdetermined dense linear algebraic system

$$\mathbf{u}^{(\text{rx})} \approx \mathbf{u}^{(\text{B})} = \Phi[p^{(\text{in})}] \boldsymbol{\gamma}^{(\kappa)}. \quad (31d)$$

These unwanted properties, which result from the discretization of the Fredholm integral equations of the first kind (17) [61,] [62, 2, 3], the relatively small number of sequential pulse-echo measurements per image, and the slow spatial decays of the outgoing free-space Green's functions (A.55) [91], [92], prevent the direct recovery of the compressibility fluctuations (30) from the recorded RF voltage signals (31a). The reformulation of this discretized linear ISP as an instance of the CS problem (5), however, circumvents this difficulty.

D. Regularization of the Inverse Scattering Problem

Postulating the knowledge of a suitable orthonormal basis of $\mathbb{C}^{N_{\text{lat}}}$, which is represented by the complex-valued unitary

⁷The positivity of the relevant discrete frequencies forming the sets (9) results in the recovery of complex-valued compressibility fluctuations (30) that contain only positive spatial frequencies along the r_d -axis.

$N_{\text{lat}} \times N_{\text{lat}}$ matrix Ψ of structural building blocks ψ_i , the complex-valued $N_{\text{lat}} \times 1$ vector of transform coefficients

$$\boldsymbol{\theta}^{(\kappa)} = \Psi^H \boldsymbol{\gamma}^{(\kappa)} \quad (32)$$

constitutes a nearly-sparse representation of the compressibility fluctuations (30). Inserting this representation, defining the complex-valued $N_{\text{obs}} \times N_{\text{lat}}$ sensing matrix

$$\mathbf{A}[p^{(\text{in})}] = \Phi[p^{(\text{in})}] \Psi, \quad (33)$$

and accounting for an unknown complex-valued $N_{\text{obs}} \times 1$ vector of additive errors of bounded ℓ_2 -norm $\|\boldsymbol{\eta}\|_2 \leq \eta$, the linear algebraic system (31) becomes

$$\mathbf{u}^{(\text{rx})} = \underbrace{\Phi[p^{(\text{in})}] \Psi}_{=\mathbf{A}[p^{(\text{in})}]} \boldsymbol{\theta}^{(\kappa)} + \boldsymbol{\eta} = \underbrace{\mathbf{A}[p^{(\text{in})}] \boldsymbol{\theta}^{(\kappa)}}_{=\mathbf{u}^{(\text{B})}} + \boldsymbol{\eta}. \quad (34)$$

The additive errors reflect the inaccuracies of the discretized physical models and the voltage measurements.

The column vectors of the sensing matrix (33), i.e. the Born approximations of the recorded RF voltage signals (31b) induced by the individual components of the nearly-sparse representation (32), define the pulse echoes of the admissible structural building blocks. Although their ℓ_2 -normalization by diagonal weighting matrices minimizes both the restricted isometry ratio and the restricted isometry constant for 1-sparse representations (32) (cf. Sect. II), it potentially amplifies the additive errors. In fact, the density of population and the dynamic range of the recorded electric energies

$$E_i^{(\text{B})} = \|\mathbf{a}_i[p^{(\text{in})}]\|_2^2 \quad (35)$$

for all $i \in [N_{\text{lat}}]$, which characterize the transfer behavior, vary significantly with the orthonormal basis. The imposition of a hard threshold on the ℓ_2 -norms, whose value is dictated by the signal-to-noise ratio (SNR) of the recorded RF voltage signals (31a), mitigates this amplification.

Let the factor $\xi \in (0; 1]$ specify the lower bound on the

ℓ_2 -norms of the sensing matrix's column vectors

$$a_{\xi,\text{lb}}[p^{(\text{in})}] = \xi \max_{i \in [N_{\text{lat}}]} \left\{ \|\mathbf{a}_i[p^{(\text{in})}]\|_2 \right\}. \quad (36)$$

The thresholded ℓ_2 -norms of these column vectors

$$a_{\xi,i}[p^{(\text{in})}] = \max \left\{ \|\mathbf{a}_i[p^{(\text{in})}]\|_2, a_{\xi,\text{lb}}[p^{(\text{in})}] \right\} \quad (37)$$

populate the real-valued $N_{\text{lat}} \times N_{\text{lat}}$ weighting matrix

$$\mathbf{W}_\xi = \text{diag} \left\{ a_{\xi,1}[p^{(\text{in})}] \quad \dots \quad a_{\xi,N_{\text{lat}}}[p^{(\text{in})}] \right\} \quad (38a)$$

and its inverse matrix

$$\mathbf{W}_\xi^{-1} = \text{diag} \left\{ \frac{1}{a_{\xi,1}[p^{(\text{in})}]} \quad \dots \quad \frac{1}{a_{\xi,N_{\text{lat}}}[p^{(\text{in})}]} \right\}, \quad (38b)$$

whose dependences on the incident acoustic pressure fields (26) are omitted for the sake of notational lucidity. The right multiplication of the sensing matrix (33) by the diagonal inverse weighting matrix (38b) yields the complex-valued normalized $N_{\text{obs}} \times N_{\text{lat}}$ sensing matrix

$$\bar{\mathbf{A}}_\xi[p^{(\text{in})}] = \mathbf{A}[p^{(\text{in})}] \mathbf{W}_\xi^{-1} = \Phi[p^{(\text{in})}] \Psi \mathbf{W}_\xi^{-1}, \quad (39)$$

whose column vectors exhibit unity ℓ_2 -norms, if the ℓ_2 -norm of the corresponding column vector in the original sensing matrix (33) is not smaller than the specified lower bound (36). This matrix maintains the potential dense population of the sensing matrix (33).

With the normalized versions of the recorded RF voltage signals $\bar{\mathbf{u}}^{(\text{rx})} = \mathbf{u}^{(\text{rx})} / \|\mathbf{u}^{(\text{rx})}\|_2$, the additive errors $\bar{\boldsymbol{\eta}} = \boldsymbol{\eta} / \|\mathbf{u}^{(\text{rx})}\|_2$ of bounded ℓ_2 -norm $\|\bar{\boldsymbol{\eta}}\|_2 \leq \bar{\eta} = \eta / \|\mathbf{u}^{(\text{rx})}\|_2$, and the nearly-sparse representation

$$\bar{\boldsymbol{\theta}}_\xi^{(\kappa)} = \frac{1}{\|\mathbf{u}^{(\text{rx})}\|_2} \mathbf{W}_\xi \boldsymbol{\theta}^{(\kappa)}, \quad (40)$$

the insertions of the weighting matrices (38) and the normalized sensing matrix (39) into the linear algebraic system (34) yield the equivalent system

$$\begin{aligned} \bar{\mathbf{u}}^{(\text{rx})} &= \frac{1}{\|\mathbf{u}^{(\text{rx})}\|_2} \left[\underbrace{\mathbf{A}[p^{(\text{in})}] \mathbf{W}_\xi^{-1} \mathbf{W}_\xi}_{=\bar{\mathbf{A}}_\xi[p^{(\text{in})}]} \boldsymbol{\theta}^{(\kappa)} + \boldsymbol{\eta} \right] \\ &= \bar{\mathbf{A}}_\xi[p^{(\text{in})}] \bar{\boldsymbol{\theta}}_\xi^{(\kappa)} + \bar{\boldsymbol{\eta}}. \end{aligned} \quad (41)$$

The associated normalized CS problem (5) reads

$$\begin{aligned} \text{Recover} \quad & \text{nearly-sparse } \bar{\boldsymbol{\theta}}_\xi^{(\kappa)} \in \mathbb{C}^{N_{\text{lat}}} \\ \text{subject to} \quad & \|\bar{\mathbf{u}}^{(\text{rx})} - \bar{\mathbf{A}}_\xi[p^{(\text{in})}] \bar{\boldsymbol{\theta}}_\xi^{(\kappa)}\|_2 \leq \bar{\eta} \end{aligned} \quad (42)$$

and the sparsity-promoting ℓ_q -minimization method for its stable solution ($\mathbf{P}_{q,\eta}$), $q \in [0; 1]$, recovers the complex-valued normalized $N_{\text{lat}} \times 1$ vector of transform coefficients

$$\begin{aligned} \hat{\boldsymbol{\theta}}_\xi^{(\kappa,q,\eta)} &\in \arg \min_{\boldsymbol{\theta} \in \mathbb{C}^{N_{\text{lat}}}} \|\tilde{\boldsymbol{\theta}}\|_q \\ \text{subject to} \quad & \|\bar{\mathbf{u}}^{(\text{rx})} - \bar{\mathbf{A}}_\xi[p^{(\text{in})}] \tilde{\boldsymbol{\theta}}\|_2 \leq \bar{\eta}. \end{aligned} \quad (\bar{\mathbf{R}}_{q,\xi,\eta})$$

The inversions of both the normalization in (40) and the basis transform in (32) estimate the compressibility fluctuations (30) as

$$\hat{\gamma}_\xi^{(\kappa,q,\eta)} = \|\mathbf{u}^{(\text{rx})}\|_2 \Psi \mathbf{W}_\xi^{-1} \hat{\boldsymbol{\theta}}_\xi^{(\kappa,q,\eta)}. \quad (43)$$

Their doubled real parts estimate the physically meaningful real-valued regular samples in the discretized compressibility fluctuations (25c) for all grid points.

VI. IMPLEMENTATION

The Fourier coefficients of the recorded RF voltage signals (8b) were determined first. The proposed method influenced the statistical properties of the additive errors in the linear algebraic system (34). In the absence of any model inaccuracies, the expected energies of both these errors and the recorded RF voltage signals (31a) permitted an estimate of the ℓ_2 -norm of the additive errors in the normalized CS problem (42). Matrix-free compositions of the fast multipole method (FMM) and a fast basis transform accelerated the sparsity-promoting ℓ_q -minimization method ($\bar{\mathbf{R}}_{q,\xi,\eta}$).

A. Determination of the Relevant Fourier Coefficients

The concurrent analog-to-digital conversion (ADC) of the RF voltage signals generated by all array elements at the rates $f_s^{(n)} = 1/T_s^{(n)} > 2f_{\text{ub}}^{(n)}$ quantized the endpoints of each recording time interval (7) as $t_{\text{lb}}^{(n)} = q_{\text{lb}}^{(n)} T_s^{(n)}$ and $t_{\text{ub}}^{(n)} = q_{\text{ub}}^{(n)} T_s^{(n)}$, where $q_{\text{lb}}^{(n)}, q_{\text{ub}}^{(n)} \in \mathbb{N}_0$ and $q_{\text{ub}}^{(n)} > q_{\text{lb}}^{(n)}$. It recorded $N_t^{(n)} = q_{\text{ub}}^{(n)} - q_{\text{lb}}^{(n)}$ real-valued samples per signal⁸ and, thus, $N_{\text{el}} N_t^{(n)}$ samples per pulse-echo measurement for all $n \in [N_{\text{in}} - 1]_0$. Normalized $N_t^{(n)}$ -point discrete Fourier transforms (DFTs) (cf. e.g. [93, Sect. 3.3.2], [75, Sect. 2.2.3], [76, Sect. 6.2]) provided the Fourier coefficients (8b) forming the vector (31a) for the quantized recording times $T_{\text{rec}}^{(n)} = N_t^{(n)} T_s^{(n)}$. The effective time-bandwidth products (10), the quantized recording times, the lower bounds on the sampling rates, and the effective bandwidths approximate the efficiencies of these procedures as

$$\text{Efficiency}^{(n)} = \frac{2N_{f,\text{BP}}^{(n)}}{N_t^{(n)}} \approx 2T_s^{(n)} B_u^{(n)} < 1 - \frac{f_{\text{lb}}^{(n)}}{f_{\text{ub}}^{(n)}} \quad (44)$$

for all $n \in [N_{\text{in}} - 1]_0$, where a Fourier coefficient occupies twice the data volume of a signal sample. The upper bounds show that the digitized data volumes exceeded those occupied by the relevant Fourier coefficients.

B. Additive Errors

Additive errors, which were statistically modeled as Gaussian white noise (GWN) (cf. e.g. [75, 110]) with zero mean and the variance σ_η^2 , corrupted the recorded samples of all RF voltage signals. The expected energy of the recorded RF voltage signals (31a) in the linear algebraic system (34) was

$$\mathbb{E} \left\{ \|\mathbf{u}^{(\text{rx})}\|_2^2 \right\} = \|\mathbf{u}^{(\text{B})}\|_2^2 + \sigma_\eta^2 N_{\text{el}} \sum_{n=0}^{N_{\text{in}}-1} \frac{N_{f,\text{BP}}^{(n)}}{N_t^{(n)}}.$$

⁸Assuming identical samples at the endpoints of the recording time intervals (7), i.e. $\tilde{u}_m^{(\text{rx},n)}[t_{\text{lb}}^{(n)}] = \tilde{u}_m^{(\text{rx},n)}[t_{\text{ub}}^{(n)}]$ for all $(n, m) \in [N_{\text{in}} - 1]_0 \times [N_{\text{el}} - 1]_0$. In general, the averages of the left and right limits replace any discontinuities [76, 40].

It permitted the ℓ_2 -norm of the normalized additive errors in the normalized CS problem (42) and the sparsity-promoting ℓ_q -minimization method ($\bar{\mathbf{R}}_{q,\xi,\eta}$) to be estimated as

$$\hat{\eta} = \left[1 + \frac{\|\mathbf{u}^{(B)}\|_2^2}{\sigma_{\hat{\eta}}^2 N_{\text{el}} \sum_{n=0}^{N_{\text{in}}-1} N_{f,\text{BP}}^{(n)} / N_t^{(n)}} \right]^{-\frac{1}{2}}. \quad (45)$$

C. Sparsity-Promoting ℓ_q -Minimization Method

Spectral projected gradient for ℓ_1 -minimization (SPGL₁) [94] implemented the convex ℓ_1 -minimization method ($\bar{\mathbf{R}}_{1,\xi,\eta}$). Foucart's algorithm [42, Sect. 4] iteratively applied this method based on SPGL₁ to a sequence of renormalized CS problems to approximate the nonconvex ℓ_q -minimization method ($\bar{\mathbf{R}}_{q,\xi,\eta}$) for the half-open parameter interval $q \in [0; 1)$. SPGL₁ is iterative and left multiplied a sequence of recursively-generated vectors by the potentially densely-populated normalized sensing matrix (39) or its adjoint. Its matrix-free implementation interpreted each type of matrix-vector product as a linear map and dedicated a customized auxiliary function to its numerical evaluation. Both functions aimed at circumventing the explicit storage of the associated matrix in the fast but limited random-access memory (RAM) and accelerating the numerical computations. In fact, the memory consumption of the normalized sensing matrix (39) and the number of multiplications executed by the associated matrix-vector product pose challenges for modern UI systems. They equal $M_{\text{conv}} = N_{\text{obs}} N_{\text{lat}} w_c$, where $w_c \in \mathbb{R}^+$ denotes the amount of memory allocated to a complex-valued variable, and $N_{\text{mul,conv}} = N_{\text{obs}} N_{\text{lat}}$, respectively. For this reason, both functions composed the FMM, a fast basis transform, and the normalization of the column vectors. The latter corresponded to a multiplication by the diagonal inverse weighting matrix (38b) and readily permitted an efficient evaluation.

D. Fast Multipole Method for the Observation Process

The FMM (cf. e.g. [95, Chapt. 9], [92], [96]) efficiently approximated the action of the observation process (31c) or its adjoint on a suitable vector. It substituted the outgoing free-space Green's functions (A.55) in the entries of the observation process (28b) by error-regulated truncated multipole expansions if the grid points $\mathbf{r}_{\text{lat},i} \in \mathcal{L}$ and $\mathbf{r}_{\text{mat},\nu}^{(m)} \in \mathcal{V}_m$, satisfied a specific geometric relationship [95, Chapt. 9], [96]. This substitution decomposed the observation process (31c) into the sum $\Phi[p^{(\text{in})}] \approx \Phi^{(\text{near})}[p^{(\text{in})}] + \Phi^{(\text{far})}[p^{(\text{in})}]$, where $\Phi^{(\text{near})}[p^{(\text{in})}]$ accounted for the grid points close to the planar transducer array, and $\Phi^{(\text{far})}[p^{(\text{in})}]$ accounted for those exceeding a specified distance from the planar transducer array [95, Sect. 9.1], [96, (8) and (23)]. The sparse population of the summand $\Phi^{(\text{near})}[p^{(\text{in})}]$ enabled both its explicit storage in the RAM and fast numerical evaluations of the associated matrix-vector products. The resulting block structure of the summand $\Phi^{(\text{far})}[p^{(\text{in})}]$, which consisted of the products of only a few unique diagonal translation matrices and densely-populated aggregation and disaggregation matrices, provided similar benefits. The small number of unique matrices enabled their explicit storage in the RAM, whereas the diagonal

population of the translation matrices concurrently reduced the computational costs.

Two C programs based on CUDA (NVIDIA Corp., Santa Clara, CA, USA) implemented parallelized versions of the FMM for the observation process (31c) and its adjoint. A Tesla K40c graphics processing unit (GPU) performed all computations with 32 bit single precision. A Matlab (The MathWorks, Inc., Natick, MA, USA) interface, which used the MEX framework and the 8 B floating-point format for real-valued variables, i.e. $w_c = 16$ B, simplified the data analyses.

E. Fast Basis Transform for the Nearly-Sparse Representation

A fast basis transform implemented the matrix-vector products between the unitary matrix Ψ , which represents the orthonormal basis specified in the nearly-sparse representation (32), or its adjoint and a suitable vector. The fast Fourier transform (FFT), for example, efficiently implemented the matrix-vector products involving the unitary DFT matrix Ψ , which represents the discrete Fourier basis, or its adjoint. Various wavelet [93] or wave atom bases [97] provide comparably-fast transforms that circumvent the explicit storage of the matrices in the RAM and minimize the computational costs.

VII. SIMULATION STUDY

The proposed method was validated using synthetic RF voltage signals. These were generated by numerical simulations of a typical pulse-echo measurement process probing two lossy heterogeneous objects by each type of incident wave. The first object mimicked a wire phantom, whereas the second object approximated the structure and the properties of human soft tissues. Additive errors of five distinct energy levels corrupted these synthetic RF voltage signals.

A. Parameters

1) *Instrumentation*: A commercial linear transducer array was emulated in the two-dimensional Euclidean space (cf. Table IV(a)). The kerfs of width zero simplified the implementation. The products $h_{m,l}^{(\text{c})} = -j\omega_l \rho_0 h_{m,l}^{(\text{tx})}$ in the incident acoustic pressure fields (26) corresponded to a modulated Gaussian pulse in the time domain.

2) *Pulse-Echo Measurement Process*: A single pulse-echo measurement was simulated for each type of incident wave (cf. Table IV(b)). The object-specific recording time interval (7) was identical for all types of incident waves. The lower and upper frequency bounds were derived from the modulated Gaussian pulse. The relevant Fourier coefficients were determined at the approximate efficiency (44) of $\text{Efficiency}^{(0)} \approx 28\%$.

3) *Syntheses of the Incident Waves*: The reference voltage signal in the excitation voltages (20) corresponded to a single period of a sinusoid, whose amplitude was irrelevant in the LTI measurement process (cf. Table IV(c)). The frequency of the clock signal in the quantization operator (20a) matched the specifications of commercial UI systems. The steered QPW propagated preferentially along the r_2 -axis. The fixed time period (23b) emerged from the direction $\mathbf{e}_\vartheta^{(0)} = (\cos(\vartheta), \sin(\vartheta))^T$.

TABLE IV: Values of all simulation parameters for the two-dimensional Euclidean space, i.e. $d = 2$, $\bar{b} = b/(2\pi)\zeta$.

a) Instrumentation (cf. Table II)		b) Pulse-echo measurements		c) Wave syntheses		d) Discretization (cf. Table III)	
$N_{\text{el}} = N_{\text{el},1} = 128$	$k_{\text{el},1} = 0$	$N_{\text{in}} = 1$, $f_s^{(0)} = 20$ MHz	$\tilde{u}^{(\text{tx},0)}(t) = \hat{u} \sin(\omega_c t)$	$N_{\text{mat}} = N_{\text{mat},1} = 4$			
$\Delta r_{\text{el},1} = w_{\text{el},1} = 304.8$ μm	$\chi_{m,l}^{(\text{tx})}(r_1) = \chi_{m,l}^{(\text{rx})}(r_1) = 1$	$f_{\text{lb}}^{(0)} = 2.6$ MHz	$f_{\text{clk}} = 80$ MHz	$\Delta r_{\text{mat},1} = 76.2$ μm			
$f_c = \omega_c/(2\pi) = 4$ MHz	$B_{h,\text{frac}} = 0.7$	$f_{\text{ub}}^{(0)} = 5.4$ MHz	QPW: $\mathbf{e}_\vartheta^{(0)} = \mathbf{e}_2$	$N_{\text{lat},1} = N_{\text{lat},2} = 512$			
$h_{m,l}^{(\text{rx})} = 1$ V m N ⁻¹		$B_u^{(0)} = 2.8$ MHz	$e_{\vartheta,1}^{(0)} \approx \cos(77.6^\circ)$	$\Delta r_{\text{lat},1} = \Delta r_{\text{lat},2} = \Delta r_{\text{mat},1}$			
$t_{\text{cut}} = 12 \ln(10)/(\omega_c B_{h,\text{frac}})$	$a = 3 \ln(10)/t_{\text{cut}}^2$			$\mathbf{r}_{\text{lat},0} = (-511, 1)^T \Delta r_{\text{lat},1}/2$			
$\tilde{h}_m^{(\text{c})}(t) = e^{-a(t-t_{\text{cut}})^2} \cos[\omega_c(t-t_{\text{cut}})]$, $t \in [0; 2t_{\text{cut}}]$				$N_{\text{lat}} = 262\,144$			
e) Wire phantom		f) Tissue-mimicking phantom		g) Regularization			
$\ \boldsymbol{\gamma}^{(\kappa)}\ _0 = 21$	$q_{\text{lb}}^{(0)} = 1$, $q_{\text{ub}}^{(0)} = 1648$	$\ \boldsymbol{\theta}^{(\kappa)}\ _0 = 10$	$q_{\text{lb}}^{(0)} = 0$, $q_{\text{ub}}^{(0)} = 1607$	$N_{\text{iter}} = 1000$			
$\boldsymbol{\Psi} = \mathbf{I}$	$T_{\text{rec}}^{(0)} = 1647 T_s^{(0)}$	$\boldsymbol{\Psi} = \boldsymbol{\Psi}_{\text{DFT}}$	$T_{\text{rec}}^{(0)} = 1607 T_s^{(0)}$	$q \in \{0.5; 1\}$			
$b = 0.217$ dB MHz ⁻² m ⁻¹	$l_{\text{lb}}^{(0)} = 215$, $l_{\text{ub}}^{(0)} = 444$	$b = 0.5$ dB MHz ⁻¹ cm ⁻¹	$l_{\text{lb}}^{(0)} = 209$, $l_{\text{ub}}^{(0)} = 433$	$N_{\text{ren}} = 10$			
$\omega_{\text{ref}} = \omega_c$	$N_{f,\text{BP}}^{(0)} = 230$	$\omega_{\text{ref}} = \omega_c$	$N_{f,\text{BP}}^{(0)} = 225$	$\epsilon_n = 1/(2+n)$, $n \in [4]_0$			
$c_{\text{ref}} = 1500$ m s ⁻¹	$N_{\text{obs}} = 29\,440$	$c_{\text{ref}} = 1540$ m s ⁻¹	$N_{\text{obs}} = 28\,800$				

4) *Spatial Discretizations*: The constant spacing between the adjacent grid points on each vibrating face along the r_1 -axis ensured approximately 3.7 points per smallest wavelength (cf. Table IV(d)). The FOV was square shaped and laterally centered in front of the linear transducer array. The identical spacings between the adjacent grid points on each vibrating face and in the FOV, i.e. $\Delta r_{\text{lat},1} = \Delta r_{\text{lat},2} = \Delta r_{\text{mat},1}$, simplified the computations of the incident acoustic pressure fields (26) and the implementation of the FMM.

5) *Wire Phantom*: The wires were represented by identical nonzero components in the compressibility fluctuations (30) (cf. Table IV(e)). Their axial distances from the linear transducer array ranged from 5 mm to 37 mm, and their axial and lateral spacings amounted to approximately 5 mm and 10 mm, respectively. The canonical basis defined the structural building block with the index $n \in [N_{\text{lat}}]$ as the individual sample located at the position $\mathbf{r}_{\text{lat},n-1} \in \mathcal{L}$ and induced a sparse representation (32). The absorption parameters in the wavenumber (13) equaled those of pure water at a temperature of 20 °C [82, Table 4.8], where the quadratic frequency dependence prevented dispersion. The quantized recording time interval (7) and the associated number of relevant discrete frequencies (10) resulted in the ratio $N_{\text{obs}}/N_{\text{lat}} \approx 11.23\%$.

6) *Tissue-Mimicking Phantom*: The discrete Fourier basis defined the structural building block with the index $n \in [N_{\text{lat}}]$ as the complex exponential function with the normalized discrete lateral and axial frequencies $\hat{K}_{n,1} = (\lceil n/512 \rceil - 257)/512$ and $\hat{K}_{n,2} = (n + 511)/512 - \lceil n/512 \rceil$, respectively (cf. Table IV(f)). Nonzero components of identical absolute value and uniformly distributed phase in the sparse representation (32) spawned dense compressibility fluctuations (30). Typical absorption parameters for soft tissues [82, Table 4.20] governed the wavenumber (13), where the linear frequency dependence implied anomalous dispersion. The quantized recording time interval (7) and the associated number of relevant discrete frequencies (10) resulted in the ratio $N_{\text{obs}}/N_{\text{lat}} \approx 10.99\%$.

7) *Additive Errors*: The five variances

$$\sigma_\eta^2 = \frac{2 \|\mathbf{u}^{(\text{B},\text{QPW})}\|_2^2}{N_{\text{el}}} 10^{-\frac{\text{SNR}_{\text{dB}}}{10}}, \quad (46)$$

where $\|\mathbf{u}^{(\text{B},\text{QPW})}\|_2^2$ equals the energy of the Born approximation of the recorded RF voltage signals (31b) induced by the QPW, and $\text{SNR}_{\text{dB}} \in \{3 \text{ dB}, 6 \text{ dB}, 10 \text{ dB}, 20 \text{ dB}, 30 \text{ dB}\}$ is the reference SNR, specified additive errors of distinct energy levels.

8) *Regularization*: The variances (46), the effective time-bandwidth product (10), and the quantized recording time permitted the approximation of the estimated ℓ_2 -norm of the normalized additive errors (45) as

$$\hat{\eta} \approx \left[1 + \frac{\|\mathbf{u}^{(\text{B})}\|_2^2 f_s^{(0)}}{\|\mathbf{u}^{(\text{B},\text{QPW})}\|_2^2 2B_u^{(0)}} 10^{\frac{\text{SNR}_{\text{dB}}}{10}} \right]^{-\frac{1}{2}}.$$

For each reference SNR, the empirical factors

$$\xi = \frac{\|\mathbf{u}^{(\text{B},\text{QPW})}\|_2^2 10^{-\frac{\text{SNR}_{\text{dB}}}{20}}}{\|\mathbf{u}^{(\text{B})}\|_2^2} \quad (47)$$

specified the lower bounds on the ℓ_2 -norms of the column vectors (36). The maximum number of iterations in SPG ℓ_1 was N_{iter} (cf. Table IV(g)). The normalization parameters ϵ_n induced a sequence of five renormalized CS problems in Foucart's algorithm (cf. Subject VI-C). Since SPG ℓ_1 provided the initial guess, Foucart's algorithm entailed six ℓ_1 minimizations.

9) *Reference Sensing Matrices*: Two types of sensing matrices, which emerged from GWN, served as benchmarks. For a sufficiently large number of observations (29), both the real-valued random $N_{\text{obs}} \times N_{\text{lat}}$ observation process

$$\boldsymbol{\Phi}^{(\text{RIP})} = \underset{m=1}{\text{vcat}} \underset{i=1}{\text{hcat}} \phi_{m,i}^{(\text{RIP})}, \quad \phi_{m,i}^{(\text{RIP})} \underset{\text{i.i.d.}}{\sim} \mathcal{N}\left(0; \frac{1}{N_{\text{obs}}}\right) \quad (48a)$$

and the associated complex-valued $N_{\text{obs}} \times N_{\text{lat}}$ sensing matrix

$$\mathbf{A}^{(\text{RIP})} = \boldsymbol{\Phi}^{(\text{RIP})} \boldsymbol{\Psi} \quad (48b)$$

met the RIP with very high probability (cf. Sect. III). The specified variance ensured recorded electric energies (35) of unity expectation. The replacement of the incident acoustic pressure field (26) in the observation process (31c) by complex-valued GWN additionally formed the complex-valued structured $N_{\text{obs}} \times N_{\text{lat}}$ observation process

$$\Phi^{(\text{GWN})} = \Phi[p^{(\text{in})}], \quad p_l^{(\text{in},0)}(\mathbf{r}_{\text{lat},i}) \underset{\text{i.i.d.}}{\sim} \mathcal{N}(0;1) \quad (49a)$$

and the associated complex-valued $N_{\text{obs}} \times N_{\text{lat}}$ sensing matrix

$$\mathbf{A}^{(\text{GWN})} = \Phi^{(\text{GWN})}\Psi. \quad (49b)$$

Although the complex-valued GWN violated the Helmholtz equations (15), this replacement correctly respected the monopole scattering and the reception by the instrumentation.

B. Methods

1) *Incident Acoustic Pressure Fields*: The acoustic pressure fields (26) were computed for all types of incident waves. For the wire phantom, their spatial and spectral dependencies were analyzed for the discrete frequency closest to the center frequency and three closely spaced positions next to the r_2 -axis, respectively. The least-squares fit of an affine linear model to the unwrapped phase of the acoustic pressure field (26) associated with the QPW at the first position was subtracted from all unwrapped phases to emphasize the differences.

2) *Recorded Radio Frequency Voltage Signals*: Ten realizations of the recorded RF voltage signals (31a) were derived from their Born approximation (31b) for each type of incident wave and each SNR by inserting the sparse representation (32) and the additive errors into the linear algebraic system (34).

3) *Recorded Electric Energies*: The recorded electric energies (35) were computed for all sensing matrices (33) except for the first reference (48b), which approximately induced the expected energies of unity. Their visual inspections revealed the transfer behaviors of the sensing matrices (33) for the tissue-mimicking phantom.

4) *Transform Point Spread Functions*: The TPSFs (6) associated with all sensing matrices were evaluated for all $(n_1, n_2) \in [N_{\text{lat}}] \times \mathbb{I}$, where $\mathbb{I} \subset [N_{\text{lat}}]$ fixed nine indices. For the wire phantom, the positions $\mathbf{r}_{\text{lat},n_2-1}$ were approximately uniformly distributed along the diagonal from $(-17.5 \text{ mm}, 2 \text{ mm})^T$ to $(17.5 \text{ mm}, 37 \text{ mm})^T$ and numbered from 1 to 9 with increasing axial coordinate. For the tissue-mimicking phantom, the normalized spatial frequencies $\hat{\mathbf{K}}_{n_2} = (\hat{K}_{n_2,1}, \hat{K}_{n_2,2})^T$ were approximately uniformly distributed along the semicircle with the center $\hat{\mathbf{K}}_c = (0, 25)^T/128$ and the radius $\hat{K}_r = 101/512$ and numbered from 1 to 9 with increasing polar angle. The thresholded ℓ_2 -norms of the column vectors (37), however, substituted the original ℓ_2 -norms in the denominators of the TPSFs (6) for this phantom to avoid the numerical inaccuracies caused by their high dynamic ranges. The empirical factors (47) with $\text{SNR}_{\text{dB}} = 10 \text{ dB}$ specified their lower bounds (36). In addition to a visual inspection, each computed TPSF (6) was characterized by its full extent at half maximum (FEHM) for each index $n_2 \in \mathbb{I}$ and its empirical cumulative distribution function (CDF). The latter excluded all $n_1 = n_2$ and, thus, stated

the percentages of diverse pulse echoes whose correlation coefficient did not exceed a specified threshold.

5) *Adjoint Normalized Sensing Matrices*: The normalized recorded RF voltage signals (41) generated by all types of incident waves were left multiplied by the adjoint normalized sensing matrices (39). The visual inspections of these products, which underlay the implementation of the sparsity-promoting ℓ_q -minimization method ($\bar{\mathbf{R}}_{q,\xi,\eta}$), revealed important interference effects affecting the recovery.

6) *Recovery by ℓ_q -Minimization*: The 200 instances of the normalized CS problem (42) generated by all types of incident waves and all realizations of the recorded RF voltage signals (31a) were solved by the sparsity-promoting ℓ_q -minimization method ($\bar{\mathbf{R}}_{q,\xi,\eta}$). In addition to a visual inspection, structural differences between the recovered compressibility fluctuations (43) and their specified version (30) were quantified by the mean structural similarity (SSIM) indices [98, (2)], whereas quantitative differences were measured by the relative root mean-squared errors (RMSEs). The sparsity and speed of convergence were gauged by the numbers of components within the illustrated dynamic range and the numbers of iterations in $\text{SPG}\ell_1$, respectively. For each wire, the incident acoustic energies (27) and the recorded electric energies (35) were related to the sample means of the relative RMSEs caused by the nonconvex $\ell_{0.5}$ -minimization method ($\bar{\mathbf{R}}_{0.5,\xi,\eta}$).

VIII. RESULTS

A. Wire Phantom

1) *Incident Acoustic Pressure Fields*: The random waves differed significantly from the QPW (cf. Fig. 5). The interference of the QCWs introduced beamlike fluctuations into the absolute values. These were relatively subtle and regular for the QPW but pronounced and irregular for the random waves. Their dynamic ranges increased from 8.15 dB for the QPW to 67.54 dB for the superposition of randomly-delayed QCWs. The paths of constant phase, which were approximately parallel to the r_1 -axis for the QPW, turned irregular with heterogeneous normal vectors exhibiting nonzero r_2 -components for the random waves. They indicated a transition from plane to irregular wavefronts.

At the three indicated positions, the absolute values reflected the approximate Gaussian shape of the electromechanical pulse echo, and the phase differences depended approximately affine-linearly on the frequency. Their slopes indicated the diverse TOFs of the wavefronts from the linear transducer array to each position. The QPW achieved very similar absolute values at all three positions, whereas the random waves induced notches and peaks at various frequencies that erratically modified the approximate Gaussian shape for each position. The former additionally achieved linear phases, whereas the latter introduced erratic deviations from this linear frequency dependence. The superposition of randomly-apodized QCWs induced relatively modest modifications, whereas both superpositions of QCWs using random time delays induced more pronounced modifications.

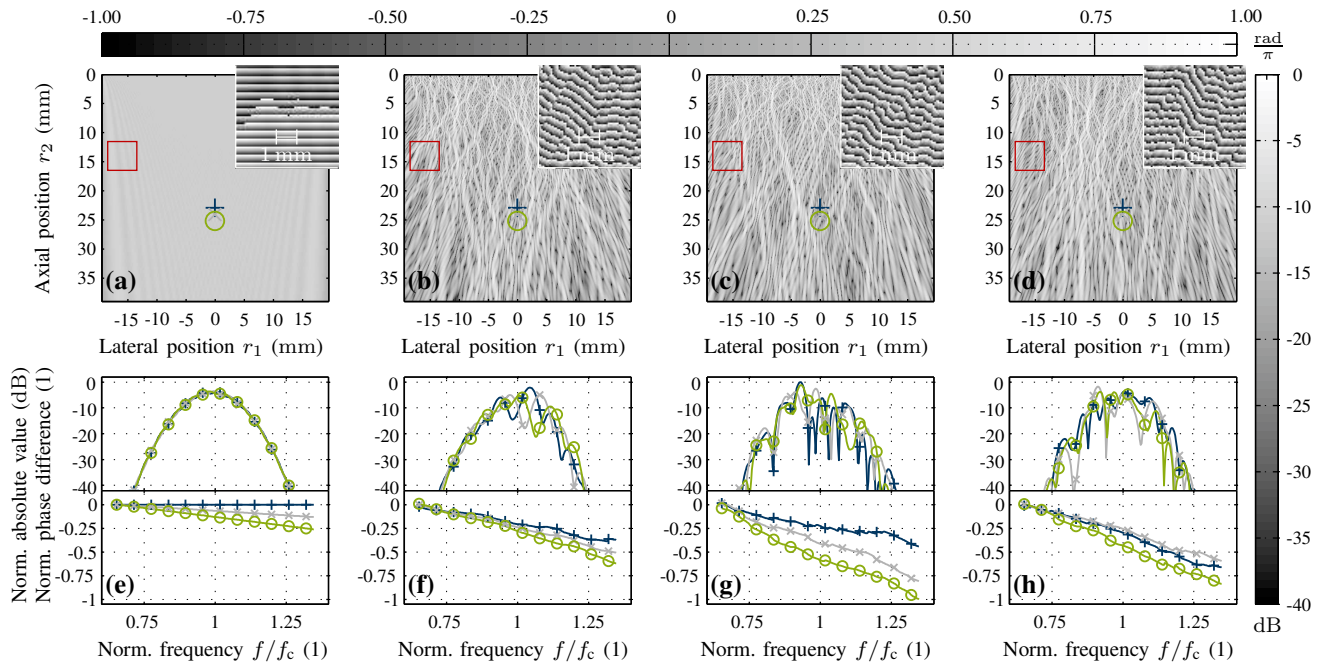


Fig. 5: Incident acoustic pressure fields (26) associated with the quasi-plane wave (cf. (a) and (e)) and the superpositions of randomly-apodized quasi-cylindrical waves (QCWs) (cf. (b) and (f)), randomly-delayed QCWs (cf. (c) and (g)), and both randomly-apodized and randomly-delayed QCWs (cf. (d) and (h)). The top row (cf. (a) to (d)) displays these fields at the discrete frequency closest to the center frequency as functions of the position. For each type of incident wave, the large image shows the normalized absolute value (right colorbar), whereas the inset image shows the phase inside the region indicated by the red square (top colorbar). The bottom row (cf. (e) to (h)) displays the normalized absolute values and the normalized phase differences at the three positions indicated by the markers in the top row as functions of the frequency.

2) *Point Spread Functions*: Although all computed PSFs (6) correctly attained their maximum absolute values of unity at the fixed positions, they differed in their behavior for the remaining positions (cf. Fig. 6). Both reference observation processes produced random values close to zero that rendered the maxima sharp and isolated. The random observation process (48a) uniformly distributed these values over the FOV, whereas its structured version (49a) formed noticeable gaps that were laterally adjacent to the maxima and shaped hourglasses of larger absolute values (cf. inset image). The observation processes (31c) induced by all incident waves concentrated relatively large absolute values close to unity in elliptical-shaped regions around the maxima. The lengths of the minor and major axes ranged from 0.15 mm to 0.3 mm and from 0.46 mm to 0.76 mm, respectively. They distributed the nonzero values less uniformly and formed sidelobes of various characters.

The observation process (31c) induced by the QPW deviated most significantly from both references. It formed the largest elliptical-shaped region and coherent sidelobes of approximately constant absolute values. In contrast, the observation processes (31c) induced by the random waves resembled that induced by the GWN (49a). The sizes of the elliptical-shaped regions decreased relative to the QPW. The sidelobes diffused and fluctuated in their values, similar to a speckle pattern, resulting in more uniform distributions. Both superpositions of QCWs using random time delays distributed the nonzero

values slightly more uniformly than the superposition of randomly-apodized QCWs. In addition, the distributed values appeared more random.

The random waves achieved FEHMs that were smaller than or equal to those of the QPW for all fixed positions, except those numbered $s \in \{6, 7\}$ (cf. Table V). The FEHMs generally increased with the axial coordinate of these positions. The maximum normalized differences ranged from 23.5% for the superposition of both randomly-apodized and randomly-delayed QCWs at the ninth fixed position, i.e. $s = 9$, to 73.7% for the superposition of randomly-delayed QCWs at the first fixed position, i.e. $s = 1$. The mean FEHMs reflected these reductions relative to the QPW. The superposition of randomly-apodized QCWs produced the largest sample mean and sample standard deviation among the random waves. Both reference observation processes consistently achieved the minimum FEHM of a two-dimensional volume element $\Delta V \approx 5.81 \times 10^{-3} \text{ mm}^2$ for all fixed positions.

The empirical CDFs confirmed the beneficial properties of the random waves (cf. Fig. 7). The random observation process (48a) primarily attained absolute values ranging from -70 dB to -30.93 dB. Only approximately 4.3% of the FOV were attributed to smaller absolute values. The structured random observation process (49a) deviated modestly from this behavior. The absolute values ranged from -70 dB to -16.79 dB. This increased dynamic range reflected the gaps that were laterally adjacent to the maxima (cf. Fig. 6(b)).

TABLE V: Full extents at half maximum of the point spread functions (6) associated with the observation processes (31c) induced by all incident waves. They were evaluated for nine uniformly distributed positions along the diagonal from $(-17.5 \text{ mm}, 2 \text{ mm})^T$ to $(17.5 \text{ mm}, 37 \text{ mm})^T$ and numbered from 1 to 9 with increasing axial coordinate.

Incident wave	Full extent at half maximum (mm^2)									Sample mean \pm std. dev.
	1	2	3	4	5	6	7	8	9	
QPW	0.19	0.18	0.21	0.24	0.28	0.32	0.38	0.42	0.51	0.30 ± 0.11
Rnd. apo.	0.07	0.09	0.14	0.17	0.16	0.18	0.44	0.36	0.51	0.24 ± 0.16
Rnd. del.	0.05	0.10	0.09	0.11	0.14	0.33	0.20	0.34	0.46	0.20 ± 0.14
Rnd. apo. del.	0.11	0.15	0.12	0.19	0.23	0.19	0.33	0.28	0.39	0.22 ± 0.10

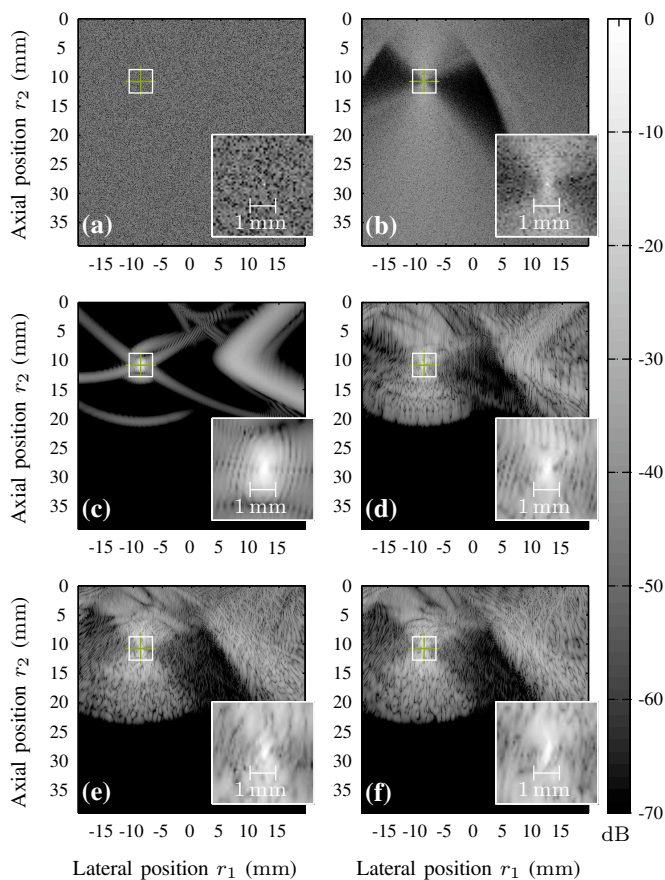


Fig. 6: Absolute values of the point spread functions (6) associated with the random observation process (cf. (a)) and the observation processes (31c) induced by the Gaussian white noise (cf. (b)), the quasi-plane wave (cf. (c)), and the superpositions of randomly-apodized quasi-cylindrical waves (QCWs) (cf. (d)), randomly-delayed QCWs (cf. (e)), and both randomly-apodized and randomly-delayed QCWs (cf. (f)). The green crosshairs indicate the third fixed position. The inset images magnify the regions indicated by the white squares.

The observation processes (31c) induced by the random waves deviated in a stronger but similar fashion from both references. The absolute values below -70 dB constituted approximately 49.5% to 56.2% of the FOV and those above this threshold,

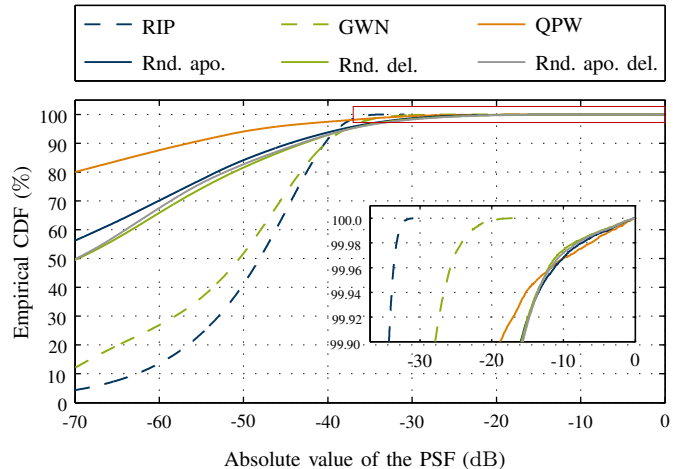


Fig. 7: Empirical cumulative distribution functions (CDFs) of the point spread functions (6) associated with both reference observation processes and the observation processes (31c) induced by all incident waves. The inset graphic magnifies the region indicated by the red rectangle.

which reached up to -0.11 dB , formed the remaining 43.8% to 50.5%. The superposition of randomly-apodized QCWs distributed the latter values over the smallest percentage of the FOV. Clearly, the observation process (31c) induced by the QPW deviated strongest from both references. The absolute values ranging from -70 dB to -0.15 dB strongly concentrated on only 20.1% of the FOV and indicated the distinctive sidelobes (cf. Fig. 6(c)).

3) *Adjoint Normalized Sensing Matrices*: All incident waves accurately detected the wires (cf. Fig. 8). The random waves substituted the coherent sidelobes produced by the QPW, whose absolute values did not fluctuate, by noise-like artifacts with a more uniform spatial distribution. These artifacts appeared slightly less uniform for the superposition of randomly-apodized QCWs than for both superpositions of QCWs using random time delays.

4) *Recovery by ℓ_q -Minimization*: All incident waves enabled both the accurate detection and the precise localization of the wires (cf. Fig. 9). The spatial extents recovered by the convex ℓ_1 -minimization method ($\mathbf{R}_{1,\xi,\eta}$) were smaller for the random waves than for the QPW. These reductions were more

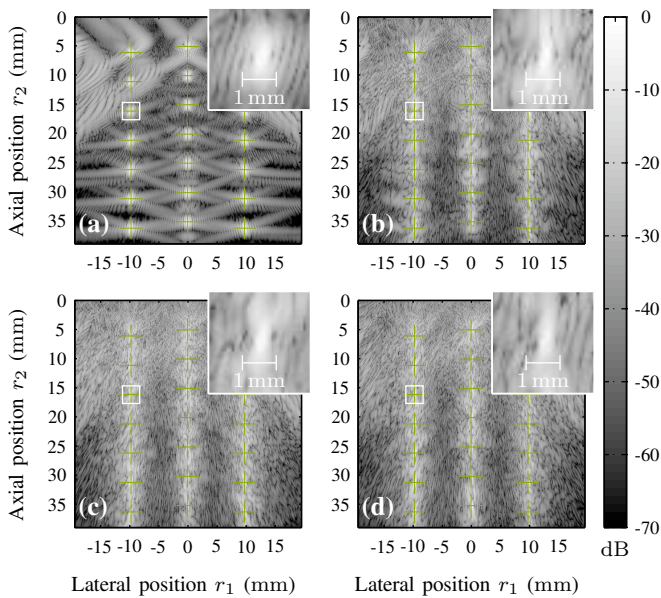


Fig. 8: Absolute values of the matrix-vector products between the adjoint normalized sensing matrix (39) and the normalized recorded RF voltage signals (41) for the quasi-plane wave (cf. (a)) and the superpositions of randomly-apodized quasi-cylindrical waves (QCWs) (cf. (b)), randomly-delayed QCWs (cf. (c)), and both randomly-apodized and randomly-delayed QCWs (cf. (d)). The green crosshairs indicate the positions of the wires and coincide with local maxima. The inset images magnify the regions indicated by the white squares. The reference SNR amounted to $\text{SNR}_{\text{dB}} = 30$ dB.

pronounced for smaller axial coordinates and, thus, approximately followed the trend of the normalized differences in the FEHMs of the PSFs (6) (cf. Table V). Moreover, the random waves caused less artifacts near the wires than the QPW (cf. inset images). Both advantages agreed with the reduced numbers of components within the illustrated dynamic range relative to the QPW. The normalized differences ranged from 58.4% for the superposition of randomly-apodized QCWs to 66.4% for the superposition of randomly-delayed QCWs. In contrast, the nonconvex $\ell_{0.5}$ -minimization method ($\bar{\mathbf{R}}_{0.5,\xi,\eta}$) consistently recovered isolated components that matched the specified compressibility fluctuations (30). The numbers of components within the illustrated dynamic range equaled the number of wires.

The mean SSIM indices confirmed the excellent structural recovery, whereas the relative RMSEs revealed an increased sensitivity of the quantitative recovery using the random waves to the energy of the additive errors (cf. Fig. 10). All incident waves achieved mean SSIM indices close to unity and comparable trends in both the relative RMSEs and the numbers of iterations for all reference SNRs and the convex ℓ_1 -minimization method ($\bar{\mathbf{R}}_{1,\xi,\eta}$). The sample means of the relative RMSEs decreased from at most 87.6% for the superposition of randomly-apodized QCWs at the lowest reference SNR to at least 34.1% for the superposition of randomly-

delayed QCWs at the highest reference SNR. Concurrently, the sample means of the normalized numbers of iterations increased from at least 3.4% for the QPW to at most 28.3% for the superposition of both randomly-apodized and randomly-delayed QCWs. The sample standard deviations of the relative RMSEs exceeded those of the mean SSIM indices and the normalized numbers of iterations for $\text{SNR}_{\text{dB}} \geq 10$ dB. The nonconvex $\ell_{0.5}$ -minimization method ($\bar{\mathbf{R}}_{0.5,\xi,\eta}$) consistently improved both the mean SSIM indices and the relative RMSEs for all reference SNRs. The random waves, however, caused significantly larger relative RMSEs than the QPW at the low reference SNRs, i.e. $\text{SNR}_{\text{dB}} \in \mathbb{Q} = \{3 \text{ dB}, 6 \text{ dB}, 10 \text{ dB}\}$, and the superposition of randomly-apodized QCWs performed worst. The sample means of the normalized numbers of iterations increased significantly by at least 18% for the QPW at the lowest reference SNR to at most 71.7% for the superposition of both randomly-apodized and randomly-delayed QCWs at the highest reference SNR. In addition, the sample standard deviations of the relative RMSEs were reduced for $\text{SNR}_{\text{dB}} \geq 10$ dB.

The variations in the incident acoustic energies (27) across the isolated positions of the wires were negligible for the QPW but strong and erratic for the random waves (cf. Fig. 11). The dynamic ranges amounted to at least 7.6 dB for the superposition of randomly-delayed QCWs and at most 8.7 dB for the superposition of randomly-apodized QCWs. The recorded electric energies (35) strongly reflected these variations and generally decreased with increasing axial coordinates of the identical wires. Fixing the energy of the additive errors in the linear algebraic system (34), they additionally reflected the SNRs of the recorded RF voltage signals (31a) induced by the individual wires. Those insonified by relatively low incident acoustic energies (27), e.g. the wires with the indices 6, 8, and 16 for the superposition of randomly-apodized QCWs (cf. blue bars in (a)), induced recorded RF voltage signals (31a) of worse SNR (cf. blue bars in (b)) than those insonified by relatively high incident acoustic energies (27), e.g. the wires with the indices 3, 11, and 16 for the superposition of both randomly-apodized and randomly-delayed QCWs (cf. gray bars in (a) and (b)). These variations in the SNRs induced variations in the mean relative RMSEs caused by the nonconvex $\ell_{0.5}$ -minimization method ($\bar{\mathbf{R}}_{0.5,\xi,\eta}$) (cf. (c)).

B. Tissue-Mimicking Phantom

1) *Recorded Electric Energies:* The transfer behaviors of the sensing matrices (33) induced by all incident waves resembled those of bandpass filters suppressing relatively low and high spatial frequencies (cf. Fig. 12). The high dynamic ranges exceeding 70 dB indicated the existence of structural building blocks whose pulse echoes contained relatively low electric energies (35). The QPW induced relatively large electric energies (35) exceeding -20 dB in a sickle-shaped passband inside the interval of normalized spatial frequencies $\mathbf{K} \in [-0.24; 0.24] \times [0.15; 0.49]$, whereas the random waves induced those in arbelos-shaped passbands inside the intervals of normalized spatial frequencies $\mathbf{K} \in [-0.43; 0.43] \times [0; 0.49]$. All formed passbands, which were significantly enlarged by

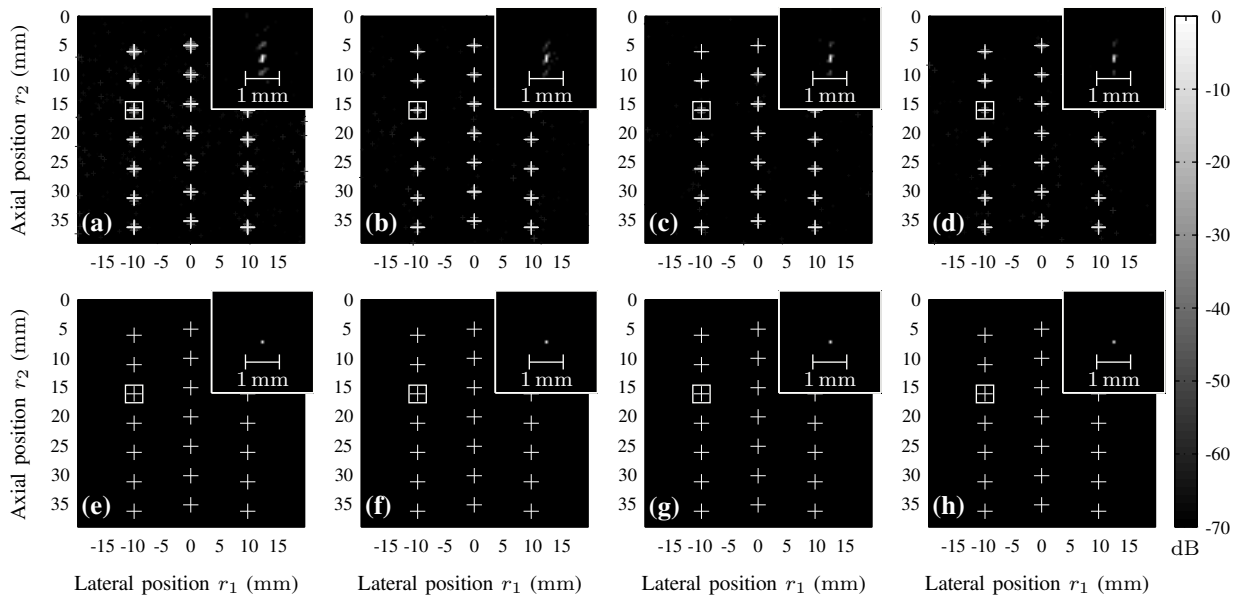


Fig. 9: Absolute values of the recovered compressibility fluctuations (43) for the quasi-plane wave (cf. (a) and (e)) and the superpositions of randomly-apodized quasi-cylindrical waves (QCWs) (cf. (b) and (f)), randomly-delayed QCWs (cf. (c) and (g)), and both randomly-apodized and randomly-delayed QCWs (cf. (d) and (h)). The top row (cf. (a) to (d)) shows the results of the convex ℓ_1 -minimization method ($\bar{R}_{1,\xi,\eta}$), whereas the bottom row (cf. (e) to (h)) shows those of the nonconvex $\ell_{0.5}$ -minimization method ($\bar{R}_{0.5,\xi,\eta}$). The large images represent the nonzero absolute values by crosshairs of proportional gray values and sizes, whereas the inset images exclusively use gray values to magnify the regions indicated by the white squares. The reference SNR amounted to $\text{SNR}_{\text{dB}} = 30$ dB.

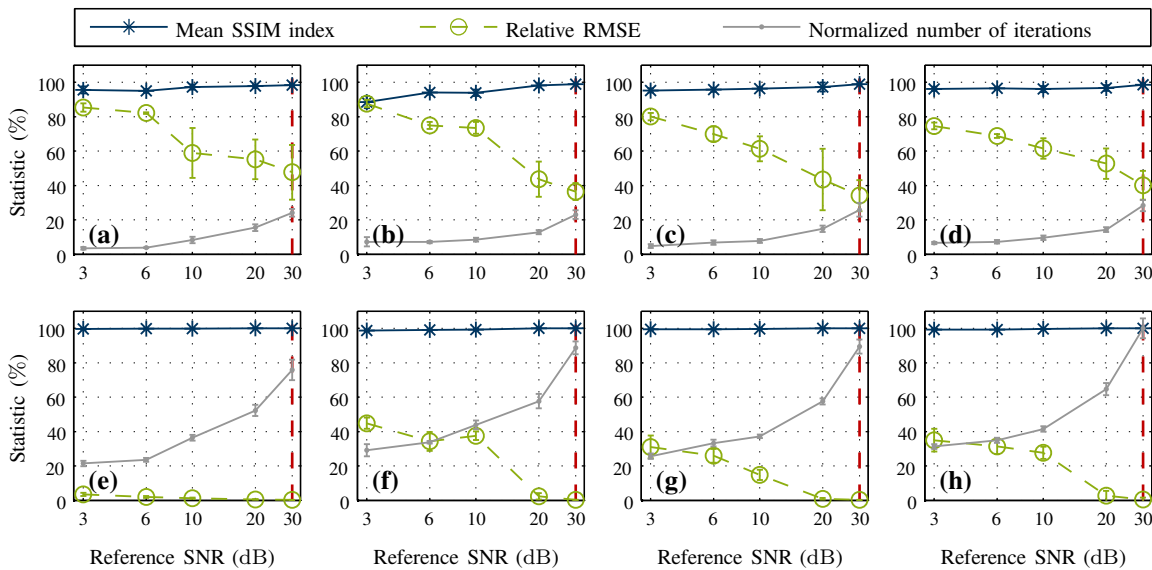


Fig. 10: Sample means and sample standard deviations of the mean structural similarity (SSIM) indices and the relative root mean-squared errors (RMSEs) achieved by the recovered compressibility fluctuations (43) and the normalized numbers of iterations in SPGL_1 . The assignment of all incident waves and both parameters $q \in \{0.5; 1\}$ governing the sparsity-promoting ℓ_q -minimization method ($\bar{R}_{q,\xi,\eta}$) to the columns and rows in this figure equals that in Fig. 9. The dashed red lines indicate the reference SNR selected for Fig. 9. The maximum sample mean of 1348.6 normalized the numbers of iterations.

the latter waves, strongly agreed with the predictions of the FDT (cf. footnote 1 in Sect. I). The bounded FOV, however, expanded the predicted passbands by beamlike artifacts. Owing to the periodicity of the DFT, these artifacts re-entered

the illustrations at the maximum normalized axial frequency of unity, i.e. $\hat{K}_2 = 1$. The absence of aliasing confirmed the specifications of sufficiently small constant spacings between the adjacent grid points in the FOV.

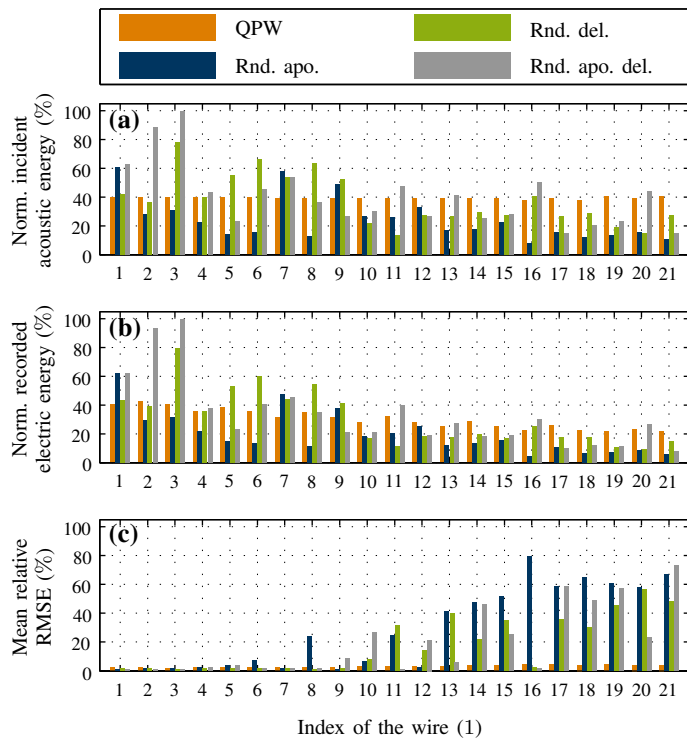


Fig. 11: Normalized incident acoustic energies (27) (cf. (a)), normalized recorded electric energies (35) (cf. (b)), and sample means of the relative root mean-squared errors (RMSEs) caused by the nonconvex $\ell_{0.5}$ -minimization method ($\bar{\mathbf{R}}_{0.5,\xi,\eta}$) (cf. (c)) for all individual wires. The maximum energies normalized both types of energy. The r_2 -coordinate of each wire increased monotonically with its index. The reference SNR amounted to $\text{SNR}_{\text{dB}} = 3$ dB.

2) *Transform Point Spread Functions*: Although all computed TPSFs (6) correctly attained their maximum absolute values of unity at the fixed spatial frequencies, they differed in their behavior for the remaining spatial frequencies (cf. Fig. 13). Both reference sensing matrices produced similar results as the random observation process (48a), i.e. uniformly distributed random values close to zero that rendered the maxima sharp and isolated (cf. Fig. 6(a)). The structured random sensing matrix (49b), however, significantly elongated these maxima along the \hat{K}_2 -axis in addition to modest lateral extensions (cf. inset image). The sensing matrices (33) induced by the random waves approximately maintained these maxima but confined similar noise-like artifacts to their passbands. In contrast, the sensing matrix (33) induced by the QPW formed smooth coherent sidelobes, whose absolute values lacked noise-like features, and indicated the presence of unspecified spatial frequencies by secondary isolated maxima, e.g. an absolute value of approximately -2.4 dB at the normalized spatial frequency $\hat{\mathbf{K}} \approx (0.12, 0.35)^T$.

The random waves achieved smaller FEHMs than the QPW for all fixed spatial frequencies, except that numbered $s = 5$ (cf. Table VI). These were identical for each fixed spatial frequency, except that numbered $s = 8$, where the superposition

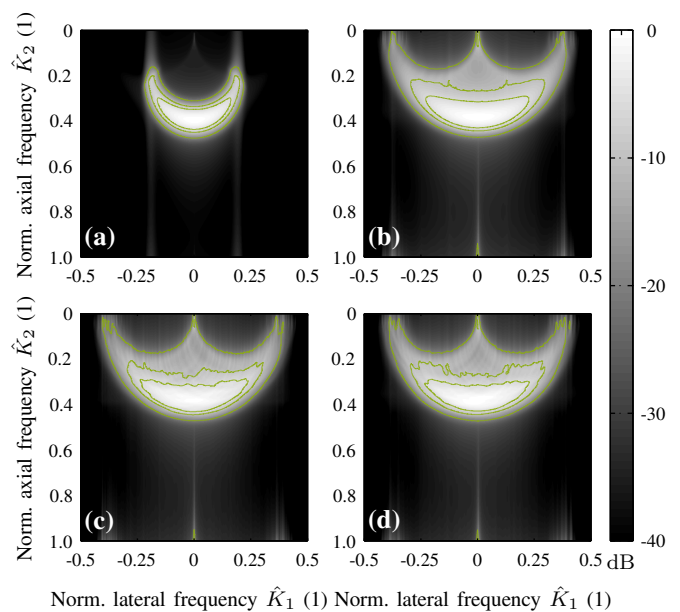


Fig. 12: Recorded electric energies (35) induced by the quasi-plane wave (cf. (a)) and the superpositions of randomly-apodized quasi-cylindrical waves (QCWs) (cf. (b)), randomly-delayed QCWs (cf. (c)), and both randomly-apodized and randomly-delayed QCWs (cf. (d)). The green contours indicate the values -6 dB, -10 dB, and -20 dB.

of randomly-delayed QCWs produced a slightly larger FEHM than the other two random waves. The secondary maxima, which were erroneously formed by the QPW (cf. Fig. 13(c)), approximately doubled these FEHMs for all fixed spatial frequencies, except that numbered $s = 5$. In fact, the maximum normalized differences ranged from 41.2% at the fixed spatial frequencies $s \in \{1, 9\}$ to 62.5% at the fixed spatial frequencies $s \in \{4, 6\}$. The mean FEHMs reflected these increases relative to the random waves. For $s = 5$, the fixed normalized spatial frequency $\hat{\mathbf{K}}_{n_2} = (0, 201)^T / 512$ matched the preferred direction of propagation of the QPW that outperformed the random waves by a normalized difference exceeding 200% . Both reference sensing matrices consistently achieved the minimum FEHM of a two-dimensional normalized spatial frequency element $\Delta \hat{K} \approx 3.81 \times 10^{-6}$ for all fixed spatial frequencies.

The empirical CDFs confirmed the beneficial properties of the random waves (cf. Fig. 14). The random sensing matrix (48b) almost exclusively attained absolute values ranging from -70 dB to -33.2 dB. Only approximately 0.3% of the admissible spatial frequencies were attributed to smaller absolute values. The structured random sensing matrix (49b) deviated marginally from this behavior. The absolute values, however, ranged from -70 dB to -7.78 dB. This increased dynamic range reflected the extended maxima (cf. Fig. 13(b)). The sensing matrices (33) induced by the random waves deviated in a stronger but almost identical fashion from both references. The absolute values below -70 dB constituted approximately 20% of the admissible spatial frequencies and those above this threshold, which reached up to -0.47 dB, formed the remain-

TABLE VI: Full extents at half maximum of the transform point spread functions (6) associated with the sensing matrices (33) induced by all incident waves. They were evaluated for nine uniformly distributed normalized spatial frequencies along the semicircle with the center $\hat{\mathbf{K}}_c = (0, 25)^T/128$ and the radius $\hat{K}_r = 101/512$ and numbered from 1 to 9 with increasing polar angle.

Incident wave	Full extent at half maximum (10^{-6})									Sample mean \pm std. dev.
	1	2	3	4	5	6	7	8	9	
QPW	64.85	26.70	22.89	30.52	3.81	30.52	22.89	26.70	64.85	32.64 ± 19.92
Rnd. apo.	38.15	11.44	11.44	11.44	11.44	11.44	11.44	11.44	38.15	17.38 ± 11.77
Rnd. del.	38.15	11.44	11.44	11.44	11.44	11.44	11.44	15.26	38.15	17.80 ± 11.60
Rnd. apo. del.	38.15	11.44	11.44	11.44	11.44	11.44	11.44	11.44	38.15	17.38 ± 11.77

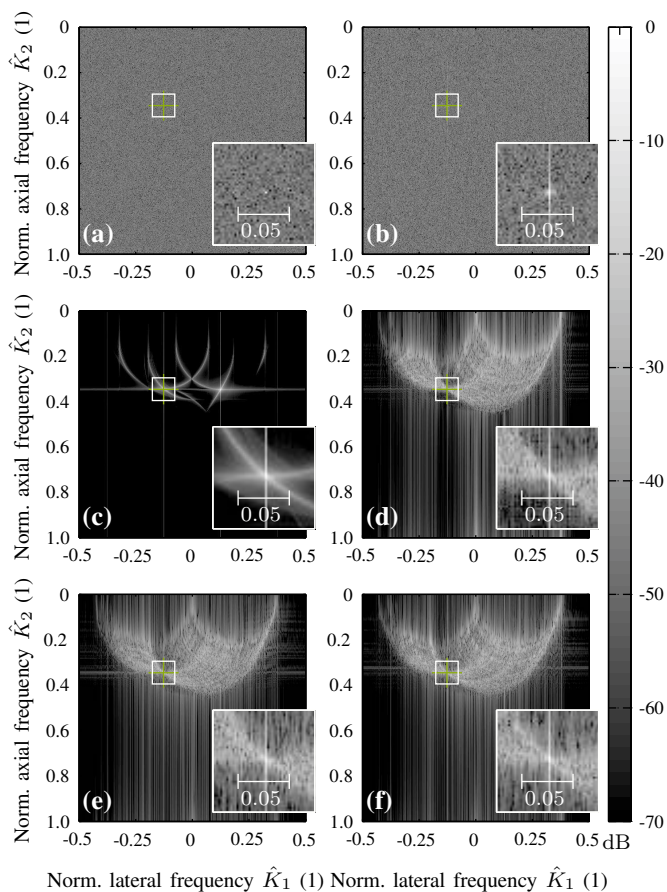


Fig. 13: Absolute values of the transform point spread functions (6) associated with the random sensing matrix (cf. (a)) and the sensing matrices (33) induced by the Gaussian white noise (cf. (b)), the quasi-plane wave (cf. (c)), and the superpositions of randomly-apodized quasi-cylindrical waves (QCWs) (cf. (d)), randomly-delayed QCWs (cf. (e)), and both randomly-apodized and randomly-delayed QCWs (cf. (f)). The green crosshairs indicate the seventh fixed normalized spatial frequency. The inset images magnify the regions indicated by the white squares.

ing 80%. Clearly, the sensing matrix (33) induced by the QPW deviated strongest from both references. The absolute values

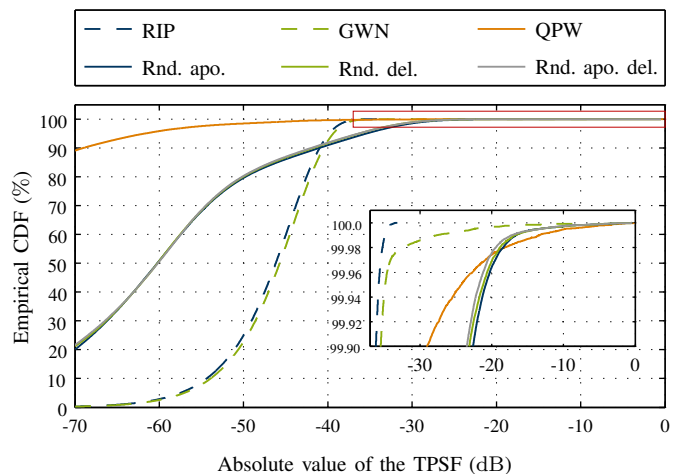


Fig. 14: Empirical cumulative distribution functions (CDFs) of the transform point spread functions (6) associated with both reference sensing matrices and the sensing matrices (33) induced by all incident waves. The inset graphic magnifies the region indicated by the red rectangle.

ranging from -70 dB to -0.19 dB strongly concentrated on only 11% of the admissible spatial frequencies and reflected both the distinctive sidelobes and the secondary maxima (cf. Fig. 13(c)).

3) *Adjoint Normalized Sensing Matrices:* All incident waves accurately detected at least 80% of the specified spatial frequencies (cf. Fig. 15). The QPW, which missed the normalized spatial frequency $\hat{\mathbf{K}} \approx (-0.23, 0.25)^T$, produced smooth coherent sidelobes and erroneously indicated the presence of multiple unspecified spatial frequencies by isolated local maxima. A pronounced local maximum was located at $\hat{\mathbf{K}}_1 \approx (-0.19, 0.25)^T$ and multiple smaller local maxima were located at $\hat{\mathbf{K}}_2 \approx (-0.11, 0.44)^T$, $\hat{\mathbf{K}}_3 \approx (-0.03, 0.46)^T$, $\hat{\mathbf{K}}_4 \approx (0.02, 0.46)^T$, $\hat{\mathbf{K}}_5 \approx (0.07, 0.46)^T$, and $\hat{\mathbf{K}}_6 \approx (0.11, 0.27)^T$. These misguided the sparsity-promoting ℓ_q -minimization method ($\bar{\mathbf{R}}_{q,\xi,\eta}$) for sufficiently large additive errors. In contrast, the random waves substituted both these sidelobes and the undesired local maxima by similar noise-like artifacts inside their passbands. These facilitated the identification of the specified spatial frequencies.

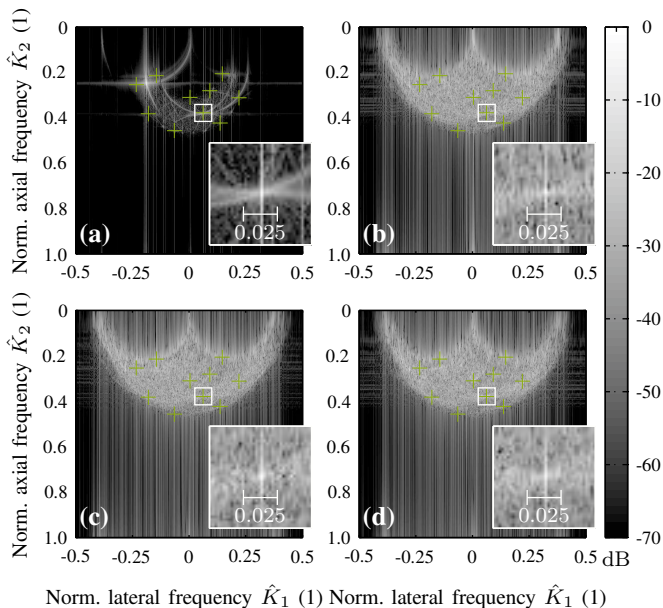


Fig. 15: Absolute values of the matrix-vector products between the adjoint normalized sensing matrix (39) and the normalized recorded RF voltage signals (41) for the quasi-plane wave (cf. (a)) and the superpositions of randomly-apodized quasi-cylindrical waves (QCWs) (cf. (b)), randomly-delayed QCWs (cf. (c)), and both randomly-apodized and randomly-delayed QCWs (cf. (d)). The green crosshairs indicate the specified spatial frequencies and mostly coincide with local maxima. The inset images magnify the regions indicated by the white squares. The reference SNR amounted to $\text{SNR}_{\text{dB}} = 10$ dB.

4) *Recovery by ℓ_q -Minimization:* The random waves enabled both the accurate detection and the precise determination of the specified spatial frequencies, whereas the QPW underperformed (cf. Fig. 16). The latter specifically failed at detecting the normalized spatial frequency $\hat{\mathbf{K}} \approx (-0.23, 0.25)^T$ near the edge of the passband and erroneously indicated multiple unspecified spatial frequencies. These coincided with the coherent sidelobes and the undesired local maxima at $\hat{\mathbf{K}}_2$ to $\hat{\mathbf{K}}_6$ (cf. Fig. 15(a)). Using the convex ℓ_1 -minimization method ($\bar{\mathbf{R}}_{1,\xi,\eta}$), the axial extents recovered by the random waves fell below those recovered by the QPW (cf. inset images). This advantage was reflected by the normalized differences in the numbers of discrete spatial frequencies indicated within the illustrated dynamic range, which exceeded 98%. The nonconvex $\ell_{0.5}$ -minimization method ($\bar{\mathbf{R}}_{0.5,\xi,\eta}$) consistently reduced both the axial extents recovered by all incident waves and the number of unspecified spatial frequencies erroneously indicated by the QPW. In fact, the numbers of discrete spatial frequencies indicated within the illustrated dynamic range equaled the number of specified spatial frequencies for both superpositions of QCWs using random time delays, whereas the superposition of randomly-apodized QCWs only caused a negligible increase. The recovered spatial frequencies strongly resembled the specified sparse representation (32). The QPW, however, still overestimated the number of speci-

fied spatial frequencies. The aforementioned findings resulted in significantly different periodic patterns in the recovered compressibility fluctuations (43) (cf. reclined images and their insets).

Both the mean SSIM indices and the relative RMSEs were consistent for the random waves, but indicated an increased sensitivity of the recovery based on the QPW to the energy of the additive errors (cf. Fig. 17). Using the convex ℓ_1 -minimization method ($\bar{\mathbf{R}}_{1,\xi,\eta}$), the random waves achieved mean SSIM indices increasing from 80.2% to 90.6%, relative RMSEs decreasing from 33.3% to 20.6%, and comparable trends in the normalized numbers of iterations for all reference SNRs. The sample means of the latter increased from at least 5.2% for the superposition of both randomly-apodized and randomly-delayed QCWs at the lowest reference SNR to at most 27.2% for the superposition of randomly-apodized QCWs at the highest reference SNR. In contrast, the QPW produced significantly worse mean SSIM indices and relative RMSEs for the low reference SNRs, i.e. $\text{SNR}_{\text{dB}} \in \mathbb{Q}$. The sample means of the former metric increased from 36.6% to 46.4%, whereas those of the latter metric decreased from 74.9% to 63.4%. For the high reference SNRs, i.e. $\text{SNR}_{\text{dB}} \in \{20 \text{ dB}, 30 \text{ dB}\}$, however, both metrics improved significantly and attained values up to 99.9% and down to 1.4%, respectively. The sample means of the normalized numbers of iterations increased from 6.4% at the lowest reference SNR to 13.1% at the highest reference SNR. Using the nonconvex $\ell_{0.5}$ -minimization method ($\bar{\mathbf{R}}_{0.5,\xi,\eta}$), the random waves consistently achieved mean SSIM indices close to unity and relative RMSEs below 6.9% for all reference SNRs. The sample means of the normalized numbers of iterations increased significantly by at least 23% for the superposition of randomly-delayed QCWs at $\text{SNR}_{\text{dB}} = 6$ dB to at most 72.8% for the superposition of randomly-apodized QCWs at the highest reference SNR. In contrast, the QPW produced only slightly better mean SSIM indices and relative RMSEs than for the convex ℓ_1 -minimization method ($\bar{\mathbf{R}}_{1,\xi,\eta}$). For all reference SNRs except $\text{SNR}_{\text{dB}} = 30$ dB, the sample means of the normalized numbers of iterations drastically exceeded those for the random waves by up to 22.9%.

C. Memory Consumption and Computational Costs

The approximate decomposition of the observation process (31c) by the FMM reduced the memory consumption, which theoretically amounted to $M_{\text{conv}} = 115$ GiB for the wire phantom and $M_{\text{conv}} = 112.5$ GiB for the tissue-mimicking phantom, to $M_{\text{FMM}} \approx 2.24\% M_{\text{conv}} \approx 2.58$ GiB and $M_{\text{FMM}} \approx 2.21\% M_{\text{conv}} \approx 2.49$ GiB, respectively. It concurrently reduced the number of multiplications, which theoretically amounted to $N_{\text{mul,conv}} \approx 7.72 \times 10^9$ for the wire phantom and $N_{\text{mul,conv}} \approx 7.55 \times 10^9$ for the tissue-mimicking phantom, to $N_{\text{mul,FMM}} \approx 93.91\% N_{\text{mul,conv}} \approx 7.25 \times 10^9$ and $N_{\text{mul,FMM}} \approx 92.32\% N_{\text{mul,conv}} \approx 6.97 \times 10^9$, respectively.

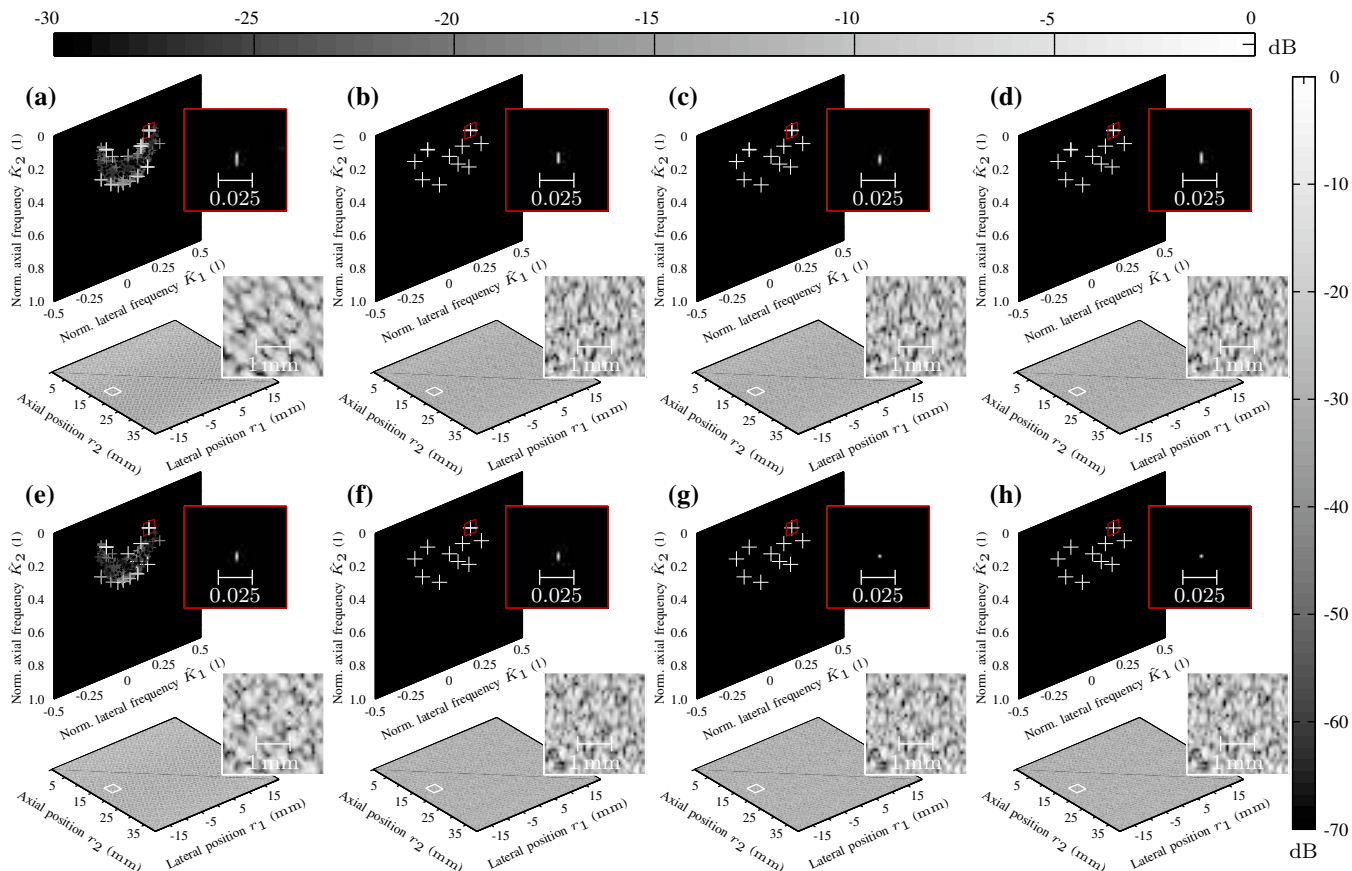


Fig. 16: Absolute values of the recovered compressibility fluctuations (43) (top colorbar; reclined) and their nearly-sparse representations (32) (right colorbar; upright) for the quasi-plane wave (cf. (a) and (e)) and the superpositions of randomly-apodized quasi-cylindrical waves (QCWs) (cf. (b) and (f)), randomly-delayed QCWs (cf. (c) and (g)), and both randomly-apodized and randomly-delayed QCWs (cf. (d) and (h)). The top row (cf. (a) to (d)) shows the results of the convex ℓ_1 -minimization method ($\tilde{\mathbf{R}}_{1,\xi,\eta}$), whereas the bottom row (cf. (e) to (h)) shows those of the nonconvex $\ell_{0.5}$ -minimization method ($\tilde{\mathbf{R}}_{0.5,\xi,\eta}$). The large upright images represent the nonzero absolute values by crosshairs of corresponding gray values and sizes, whereas the remaining images exclusively use gray values. The inset images magnify the regions indicated by the red and white squares. The reference SNR amounted to $\text{SNR}_{\text{dB}} = 10$ dB.

IX. DISCUSSION

A. Random Waves Decorrelate the Pulse Echoes of the Admissible Structural Building Blocks

The isolated maxima of minimum FEHMs, which were embedded in random values close to zero and characterized the TPSFs (6) associated with all reference sensing matrices (cf. Figs. 6(a), 6(b), 13(a) and 13(b)), indicate optimal spatial and spectral resolutions. They resolved the adjacent grid points in the FOV for the wire phantom and the adjacent discrete spatial frequencies for the tissue-mimicking phantom. In fact, the RIP for 4-sparse representations (32), which was met by the random sensing matrices (48b) with very high probability, ensured the stable recovery of all 2-sparse representations (32), including those whose nonzero components populate adjacent grid points or discrete spatial frequencies.

The noise-like properties of random values close to zero enabled their removal by the sparsity-promoting ℓ_q -minimization method ($\tilde{\mathbf{R}}_{q,\xi,\eta}$). The gaps formed by the structured random observation process (49a) for the wire phantom (cf. Fig. 6(b))

arose from the single reception angle in the pulse-echo setup, i.e. the fixed position of the linear transducer array on a single edge of the FOV. The elimination of these gaps by the structured random sensing matrix (49b) for the tissue-mimicking phantom (cf. Fig. 13(b)) hints at potential benefits provided by the random waves for the specified structural building blocks, i.e. the complex exponential functions.

The increased FEHMs of the TPSFs (6) associated with the sensing matrices (33) induced by all incident waves (cf. Tables V and VI), which resulted from the elliptical-shaped regions of absolute values close to unity around the maxima for the wire phantom (cf. Figs. 6(c) to 6(f)) and the extended maxima for the tissue-mimicking phantom (cf. Figs. 13(c) to 13(f)), indicate degraded spatial and spectral resolutions. In contrast to the GWN forming the structured random sensing matrix (49b), the incident acoustic pressure fields met the Helmholtz equations (15) and, thus, strongly correlated the pulse echoes of the adjacent grid points and the adjacent discrete spatial frequencies. In their attempt to replicate the desirable properties of the GWN, however, the random waves

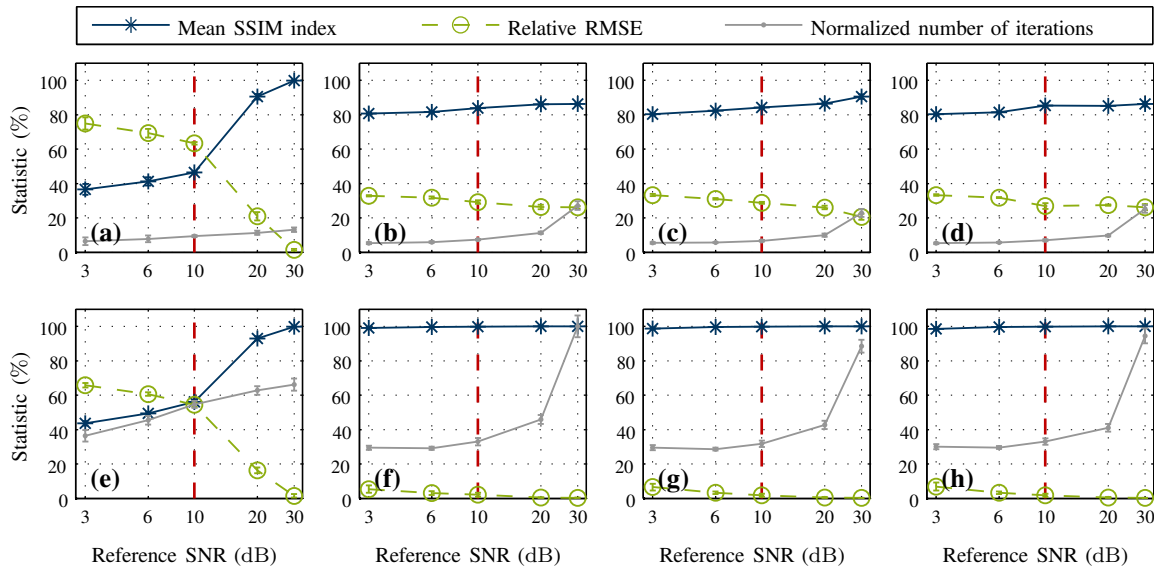


Fig. 17: Sample means and sample standard deviations of the mean structural similarity (SSIM) indices and the relative root mean-squared errors (RMSEs) achieved by the recovered compressibility fluctuations (43) and the normalized numbers of iterations in SPG_{ℓ_1} . The assignment of all incident waves and both parameters $q \in \{0.5; 1\}$ governing the sparsity-promoting ℓ_q -minimization method ($\bar{\mathbf{R}}_{q,\xi,\eta}$) to the columns and rows in this figure equals that in Fig. 16. The dashed red lines indicate the reference SNR selected for Fig. 16. The maximum sample mean of 1127.6 normalized the numbers of iterations.

significantly outperformed the QPW.

In fact, the noise-like artifacts (cf. Figs. 6(d) to 6(f) and 13(d) to 13(f)) with more uniform distributions of the nonzero values, which populated 43.8% to 50.5% of the FOV for the wire phantom (cf. Fig. 7) and 80% of the admissible spatial frequencies for the tissue-mimicking phantom (cf. Fig. 14), resembled those induced by the structured random sensing matrices (49b) (cf. Figs. 6(b) and 13(b)). Unlike the coherent sidelobes and the secondary maxima induced by the QPW (cf. Figs. 6(c) and 13(c)), they prevented sparse approximations and, thus, enabled their removal by the sparsity-promoting ℓ_q -minimization method ($\bar{\mathbf{R}}_{q,\xi,\eta}$). The reductions in the FEHMs, which ranged from 23.53% to 73.68% for the wire phantom (cf. Table V) and from 41.17% to 62.52% for the tissue-mimicking phantom (cf. Table VI) with few exceptions, indicate improved spatial and spectral resolutions. The slightly increased mean FEHM and the deviation in the empirical CDF produced by the superposition of randomly-apodized QCWs for the wire phantom, however, indicate potential benefits provided by the random time delays.

B. Image Recovery by ℓ_q -Minimization is Quantitative

The left multiplications of the normalized recorded RF voltage signals (41) by the adjoint normalized sensing matrices (39) initialized SPG_{ℓ_1} and qualitatively recovered the normalized nearly-sparse representations (40) (cf. Figs. 8 and 15). They linearly combined the TPSFs (6) for all $n_1 \in \text{supp}[\theta^{(\kappa)}]$ and added errors, as shown in (A.57) (cf. Appendix II). Equivalently, they assigned linear combinations of the zero-lag cross-correlations (A.58) between the recorded RF voltage signals (8) and the pulse echoes of the admissible structural building blocks to the components and, thus, significantly en-

hanced the popular DAS method. In fact, the latter combines the canonical basis with the approximation of all pulse echoes by delayed Dirac delta distributions [28, Sect. IV.A.2].

The proposed method, in contrast, enabled the quantitative recovery of the specified compressibility fluctuations (30) via the sparsity-promoting ℓ_q -minimization method ($\bar{\mathbf{R}}_{q,\xi,\eta}$). Since the identification of the significant components in the normalized nearly-sparse representations (40) essentially thresholded the aforementioned products [41, Fig. 2], however, the coherent sidelobes and the secondary maxima in the TPSFs (6) induced by the QPW (cf. Figs. 6(c) and 13(c)) caused artifacts for sufficiently large additive errors (cf. Figs. 9(a), 16(a) and 16(e)). The FEHMs for the wire phantom, which significantly exceeded the size of a volume element (cf. Table V), increased the numbers of components within the illustrated dynamic range and, thus, the relative RMSEs for the convex ℓ_1 -minimization method ($\bar{\mathbf{R}}_{1,\xi,\eta}$) (cf. Figs. 10(a) to 10(d)). Although the tissue-mimicking phantom reduced this ratio (cf. Table VI) and, thus, the relative RMSEs for the random waves (cf. Figs. 17(b) to 17(d)), the secondary maxima prevented this reduction for the QPW (cf. Fig. 17(a)). The mean SSIM indices, however, confirmed the excellent structural recovery of both phantoms by the random waves.

The consistent improvements of all quality metrics by the nonconvex $\ell_{0.5}$ -minimization method ($\bar{\mathbf{R}}_{0.5,\xi,\eta}$) (cf. Figs. 10 and 17) indicate its superiority to the convex ℓ_1 -minimization method ($\bar{\mathbf{R}}_{1,\xi,\eta}$) for the specified compressibility fluctuations (30). The larger numbers of iterations, which arose from the six executions of SPG_{ℓ_1} , however, increase the computational costs and the recovery times. These findings agree with those derived from numerical experiments in the literature (cf. e.g. [42, Sect. 5], [43, Sect. 3], [44, Sect. III]). In fact, the

minimization of the ℓ_q -quasinorm, $q \in (0; 1)$, in the sparsity-promoting method ($\mathbf{P}_{q,\eta}$) exactly recovered sparse representations (2) from a significantly smaller number of error-free observations [43], [44]. Sufficient conditions, which relax the upper bounds on the restricted isometry ratio or constant for smaller parameters q , ensure the stable recovery and justify these findings [42, Thm. 3.1], [44, Thm. 1]⁹.

The intractability of the nonconvex ℓ_q -minimization method ($\bar{\mathbf{R}}_{q,\xi,\eta}$), $q \in [0; 1)$, necessitates the approximation of the global minima by local minima using suitable initializations. Although the proposed implementation does not guarantee the recovery of the global minimum [42, Sect. 4], the observed improvements indicate its convergence to the specified sparse representations (32).

The simulation study focused on the two parameters $q \in \{0.5; 1\}$. Foucart *et al.* [42, Sect. 5] demonstrated the benefits of retaining the sparsest result provided by a finite set of discrete parameters $q \in [0; 1]$ at the expense of higher computational costs. The reweighted ℓ_1 minimization [99] is a special instance of Foucart's algorithm for $q = 0$ that does not unequivocally achieve the best results. Achim *et al.* [100] proposed a method to infer the optimal parameter q from the characteristic exponent of a symmetric α -stable distribution modeling the temporal samples of an individual beamformed RF voltage signal or its DFTs. The author speculates that suitable statistical models for the normalized nearly-sparse representation (40) could enable similar methods.

C. Spatially Extended Structural Building Blocks Increase the Robustness Against the Additive Errors

For the wire phantom, the substantial relative RMSEs at the low reference SNRs (cf. Figs. 10(f) to 10(h)) revealed an undesired sensitivity of the compressibility fluctuations (43) recovered by the random waves to the energy of the additive errors. The variations in the incident acoustic energies (27) across the isolated positions of the wires and the resulting variations in the mean relative RMSEs (cf. Figs. 11(a) and 11(c)) suggest that (i) the energy-guided relocation of the wires, (ii) different realizations of the random waves, or (iii) multiple sequential pulse-echo measurements overcome this sensitivity. A fixed experimental setup, however, excludes option (i), and only option (iii) ensures consistent results for various configurations. The variations further suggest that (iv) spatially extended structural building blocks reduce this sensitivity.

Indeed, for the tissue-mimicking phantom, the negligible relative RMSEs at the low reference SNRs (cf. Figs. 17(f) to 17(h)) indicate the robustness of the compressibility fluctuations (43) recovered by the random waves against the additive errors. In contrast to the wires, the spatially extended complex exponential functions scattered the incident acoustic pressure fields (26) at all grid points in the FOV and, thus, completely reradiated their spatial variations. The significantly enlarged passbands of the sensing matrices (33) induced by the random waves (cf. Figs. 12(b) to 12(d)) prove that their scattered waves interfere less destructively on the faces of the array elements

than those caused by the QPW. In addition to the robustness, they explain the reductions of the mean FEHMs relative to the QPW for the wire phantom (cf. Table V). Their strong agreement with the predictions of the FDT further indicates the correctness of the numerical simulations.

D. Worst-Case Coherences Provide Impractical Upper Bounds on the Numbers of Nonzero Components

The arguments of the maxima in the empirical CDFs of the TPSFs (6) (cf. Figs. 7 and 14) bounded from below the worst-case coherences of the sensing matrices (33), which are defined as [35, Def. 5.1]

$$\mu(\mathbf{A}[p^{(in)}]) = \max_{n_1 \neq n_2} \left\{ |\text{TPSF}\{\mathbf{A}[p^{(in)}]\}(n_1, n_2)| \right\} \quad (50)$$

and obey the Welch lower bounds [35, Thm. 5.7]

$$\mu_{\text{lb,w}}(\mathbf{A}[p^{(in)}]) = \sqrt{\frac{N_{\text{lat}} - N_{\text{obs}}}{N_{\text{obs}}(N_{\text{lat}} - 1)}}, \quad (51)$$

according to the inequality

$$\mu_{\text{lb,w}}(\mathbf{A}[p^{(in)}]) \leq \mu_{\text{lb}}(\mathbf{A}[p^{(in)}]) \leq \mu(\mathbf{A}[p^{(in)}]). \quad (52)$$

These measures, in turn, loosely bounded from above the RICs of the normalized sensing matrices (39) for $2s$ nonzero components [35, Prop. 6.2], i.e.

$$\delta_{2s}(\bar{\mathbf{A}}_{\xi}[p^{(in)}]) \leq (2s - 1)\mu(\mathbf{A}[p^{(in)}]) < \delta_{2s,\text{ub}} \quad (53)$$

for all factors $\xi \leq \min_{i \in [N_{\text{lat}}]} \{\|\mathbf{a}_i[p^{(in)}]\|_2\} / \max_{i \in [N_{\text{lat}}]} \{\|\mathbf{a}_i[p^{(in)}]\|_2\}$, where $\delta_{2s,\text{ub}}$ denotes the specific upper bound imposed by a suitable sufficient condition ensuring the stable recovery. The complete relaxation of this upper bound, i.e. $\delta_{2s,\text{ub}} = 1$ [35, 134], and the successive insertions of both lower bounds on the worst-case coherences (52) yield the upper bounds on the numbers of nonzero components

$$s < \frac{1}{2} \left[\frac{1}{\mu_{\text{lb}}(\mathbf{A}[p^{(in)}])} + 1 \right] \leq \frac{1}{2} \left[\frac{1}{\mu_{\text{lb,w}}(\mathbf{A}[p^{(in)}])} + 1 \right]. \quad (54)$$

These upper bounds, however, did not provide any practical guarantees for the normalized sensing matrices (39) induced by all incident waves and, thus, seemed to contradict the numerical simulations (cf. Table VII). Moreover, both reference sensing matrices only ensured the recovery of at most 22 nonzero components, and neither of the investigated sensing matrices (33) achieved the Welch lower bounds (51). Multiple authors confirmed this impracticality [66] and the worst-case coherences close to unity in pulse-echo UI [25, Fig. 6], [51, Table 1], [28, Fig. 9].

The impracticality of the upper bounds (54) arose from both the looseness of the upper bounds on the RICs provided by the worst-case coherences (53) and the limited spatial and spectral resolutions. The latter prevented the recovery of sparse representations (32) whose nonzero components populated adjacent grid points or discrete spatial frequencies. The upper bounds $s < 2$ prohibited such configurations and reflected this limitation. They did not contradict the numerical simulations because specific configurations meeting the resolution requirements were recoverable. The increase of the

⁹Foucart *et al.* [42] corrected a minor imprecision in the argument.

TABLE VII: Upper bounds on the numbers of nonzero components (54) for both reference sensing matrices and the sensing matrices (33) induced by all incident waves. Their best possible values arose from the Welch lower bounds on the worst-case coherences (51), whereas their remaining values arose from the lower bounds on the worst-case coherences (52) provided by the arguments of the maxima in the empirical CDFs of the TPSFs (6).

Object	Upper bound on the number of nonzero components (1) [lower bound on the worst-case coherence (%)]						
	Welch lower bound	RIP	GWN	QPW	Rnd. apo.	Rnd. del.	Rnd. apo. del.
Wire phantom	91 [0.55]	18 [2.84]	3 [14.47]	1 [98.28]	1 [98.71]	1 [98.67]	1 [98.46]
Tissue-mimicking phantom	90 [0.56]	23 [2.19]	1 [40.82]	1 [97.87]	1 [94.68]	1 [94.21]	1 [94.77]

constant spacings between the adjacent grid points in the FOV trivially decorrelates their pulse echoes and, thus, effectively reduces the worst-case coherences (50) and increases the upper bounds (54). Faithful discrete representations of the continuous physical models, however, impose upper bounds on these spacings and enforce a trade-off. The impracticality of the upper bounds (54) emphasizes the importance of alternative concepts to assess the suitability of the normalized sensing matrices (39), e.g. the presented and frequently-used investigation of the TPSFs (cf. e.g. [39], [41]) and quantitative recovery experiments. These empirically revealed the advantages of the random waves over the QPW.

E. Multiple Sequential Pulse-Echo Measurements per Image do not Resolve the Effective Underdeterminedness

The number of sequential pulse-echo measurements per image simultaneously controls both the acquisition time and the number of observations (29). Its sufficient increase formally resolves the typical underdeterminedness of the linear algebraic system (31) in ultrafast UI. The wire and the tissue-mimicking phantoms, for instance, required the minimal numbers $N_{\text{in}} \geq 9$ and $N_{\text{in}} \geq 10$, respectively, for this purpose. Even an observation process (31c) of full mathematical rank, however, remains ill-conditioned and, thus, exhibits a non-trivial quasi-nullspace, i.e. a set of nonzero compressibility fluctuations (30) whose pulse echoes contain relatively low electric energies [61, 4], [62, 1, 3]. These vectors represent lossy heterogeneous objects that are almost invisible to the pulse-echo measurement process [21, Sects. 6.9.1 and 6.9.4]. Their existence renders the linear algebraic system (31) effectively underdetermined because the additions of their linear combinations to any exact solution only induce negligible residuals [61, 4], [62, 1, 3]. The complex exponential functions of relatively low and high spatial frequencies exemplified such vectors for the observation processes (31c) induced by all waves incident on the tissue-mimicking phantom (cf. Fig. 12). The maximal passbands, which are limited by the electromechanical transfer behavior of the instrumentation and approximately achieved by the random waves, are invariant to the number of sequential pulse-echo measurements per image. Although the increase of the latter does not eliminate the need for regularization, it (i) enlarges the suboptimal passbands achieved by the steered QPWs for various preferred directions of propagation and (ii) improves the robustness

of the recovered compressibility fluctuations (43) against the additive errors (cf. Subject. IX-C).

F. Significance of the Fast Multipole Method for the Sparsity-Promoting ℓ_q -Minimization Method

The numerical evaluations of tens to hundreds of matrix-vector products involving the normalized sensing matrix (39) or its adjoint by the sparsity-promoting ℓ_q -minimization method ($\bar{\mathbf{R}}_{q,\xi,\eta}$) (cf. Figs. 10 and 17) emphasize the significance of both auxiliary functions in the proposed matrix-free implementation. The normalized reductions in the memory consumption and the number of multiplications achieved by the FMM, which amounted up to 97.8% and 7.7%, respectively, confirm its effectiveness in achieving both aims of these functions. Although modern UI systems typically lack the amounts of fast RAM required for the explicit storage of the observation process (31c), they can readily store its approximate decomposition provided by the FMM. A detailed analysis of the FMM for the excitation by steered PWs reported even higher normalized reductions in the memory consumption and the number of multiplications of 99.75% and 76%, respectively [101]. The author hypothesizes that additional optimizations in the discretization of the truncated multipole expansions enable further improvements.

The availability of the FMM, which results from the usage of the outgoing free-space Green's functions (A.55), is a crucial advantage of the analytical derivation of the observation process (31c) over the numerical constructions using simulation software or experimental measurements proposed in [26], [54]. The FMM provides explicit analytical expressions for the sparse approximation of the observation process (31c), whereas algebraic methods, e.g. the singular value decomposition [61], [62] and its enhancements [102], the adaptive cross approximation [103], or various transforms [91], [97], [104], rely on the numerical values of its entries (28b) or its action on a suitable vector. The constancy of the observation process (31c) in multiple instances of the normalized CS problem (42), which frequently occurs in practice, reduces the relevance of the increased complexity.

G. Reduction of the Number of Observations Enables Sub-Nyquist Sampling Rates

The number of observations (29) defines the minimal data volume required for the determination of the relevant Fourier coefficients (8b). It simultaneously controls both the memory

consumption and the computational costs raised by the numerical evaluations of the matrix-vector products involving the normalized sensing matrix (39) or its adjoint. Besides minimizing the number of sequential pulse-echo measurements per image, (i) the deactivation of selected receiving array elements [25, Sect. III-C.1)], [51, Sects. 3.2 and 4], [28, Sect. V-B], (ii) the random temporal mixing of the recorded RF voltage signals [25, Sect. III-C.2)], (iii) random temporal projections [29], and (iv) customized alternative discretizations of the frequency axis [39, Sects. VI-B and VII] enable its significant reduction. The latter specifically reduce the cardinalities of the sets of relevant discrete frequencies (9) below the effective time-bandwidth products (10). These approaches, however, potentially discard essential observations discriminating the pulse echoes of the structural building blocks and typically increase their correlations.

Optimal methods therefore (i) minimize these correlations and (ii) capture Fourier coefficients (8b) of relatively high SNRs. The suppression of the incoherent aliasing by the sparsity-promoting ℓ_q -minimization method ($\bar{\mathbf{R}}_{q,\xi,\eta}$) then enables sub-Nyquist spatiotemporal sampling rates. In the simulation study, for instance, the approximate Gaussian distribution of the energy in the Fourier coefficients (8b) over the frequency axis (cf. Table IV) permits the selection of only a few consecutive discrete frequencies around the center frequency [72, Sect. III-B], [73, Sect. IV-B]. A uniform distribution of this energy, in contrast, would permit the selection of randomly and uniformly distributed discrete frequencies [73, Sect. IV-B].

Using sub-Nyquist temporal sampling rates, the proposed method resembles the compressed beamforming methods [70]–[74]. In fact, both types of methods leverage a sparsity-promoting ℓ_q -minimization method ($\mathbf{P}_{q,\eta}$) to recover specific signals from only a few Fourier coefficients (8b) associated with the selected discrete frequencies. The former, however, recovers d -dimensional acoustic material parameters based on realistic physical models. It minimizes the number of sequential pulse-echo measurements per image and, thus, maximizes the frame rate. The latter methods, in contrast, use the popular DAS method to focus the recorded RF voltage signals. They model the one-dimensional focused signals composing the image as quantized finite streams of known pulses¹⁰ and individually recover hundreds of nearly-sparse parameter vectors defining these streams. They primarily reduce the temporal sampling rates, and only their most recent versions additionally support high frame rates [70], [71]. The superior physical model driving the proposed method, however, further increases the frame rate and significantly improves the image quality.

H. Experimental Validations

An experimental validation of the proposed method using the plane-wave imaging challenge in medical ultrasound (PICMUS) data and $N_{\text{in}} \in \{1, 3\}$ sequential pulse-echo measurements based on steered QPWs was presented in [107].

¹⁰Finite streams of known pulses are special instances of finite rate of innovation signals, i.e. analog signals defined by a finite number of parameters in an underlying signal model per unit of time (cf. e.g. [105] and [106]).

Comparisons to established image recovery methods, including SA, DAS, filtered backpropagation, and the progressive scanning by focused beams, at increasing stages of evolution were shown in [30], [32]–[34].

I. Limitations

Multiple important investigations had to be left for future research. These mainly include statistical analyses of the admissible numbers of significant components in the nearly-sparse representation (32) for various numbers of sequential pulse-echo measurements per image, parameters q governing the sparsity-promoting ℓ_q -minimization method ($\bar{\mathbf{R}}_{q,\xi,\eta}$), energy levels of the additive errors, realizations of the random waves, and orthonormal bases (cf. e.g. [43, Figs. 1 and 2], [44, Figs. 3 and 4]). The large numbers of parameter combinations and the high computational costs induced by the proposed implementation of the sparsity-promoting ℓ_q -minimization method ($\bar{\mathbf{R}}_{q,\xi,\eta}$) currently prevent such combinatorial analyses for normalized CS problems (42) of the investigated sizes. Furthermore, the presented study focused on simple types of random waves that can readily be synthesized by programmable UI systems. Although more advanced syntheses, e.g. element specific coded excitation voltages, increase the complexity of the transmit hardware, they potentially further decorrelate the pulse echoes and, thus, deserve additional studies. Moreover, the numerical simulations of the pulse-echo measurement process in the two-dimensional Euclidean space, i.e. $d = 2$, exclude variations along the elevational direction. They underestimate the diffraction-induced decay of the ultrasonic waves, which is asymptotically proportional to $\|\mathbf{r}\|_2^{-(d-1)/2}$ for the outgoing free-space Green's functions (A.55), and predict less realistic results. The rectilinear boundary conditions prohibit the usage of curved transducer arrays, and the linear wave propagation neglects finite amplitude effects. Eventually, the Born approximation, which dominates practical image recovery methods in UI, excludes multiple scattering and, thus, any phase aberrations. Despite these limitations and open investigations, however, the presented results reliably outline the potential drawbacks and the benefits of random incident waves in fast compressed pulse-echo UI.

X. CONCLUSION AND OUTLOOK

The proposed syntheses of random waves applied random apodization weights, time delays, or combinations thereof to reference excitation voltages and aided in meeting a central requirement of the CS framework in fast compressed pulse-echo UI. They decorrelated the pulse echoes of the admissible structural building blocks composing the lossy heterogeneous object to be imaged relative to the prevalent steered QPWs. These blocks equaled the individual basis functions in a nearly-sparse representation of the spatial compressibility fluctuations. A sparsity-promoting ℓ_q -minimization method enabled both the structural and the quantitative recovery of two phantoms from synthetic RF voltage signals. These were generated by single realizations of the random waves in numerical simulations of the pulse-echo measurement process in the two-dimensional Euclidean space. Although the spatial variations in the incident

acoustic energies caused residual errors at low SNRs for the sparse wire phantom, they improved the identification of the spatially extended structural building blocks defined by the discrete Fourier basis and significantly enlarged the passbands of the sensing matrices for the tissue-mimicking phantom. The FMM enabled an efficient GPU-based implementation of both types of matrix-vector products required by the iterative algorithms.

The proposed physical models for the pulse-echo measurement process and the syntheses of the incident waves provide the flexibility to investigate alternative types of incident waves, e.g. superpositions of multiple individually coded quasi- $(d-1)$ -spherical waves [108], random focused beams, structured waves [109], and even arbitrary experimentally measured waves. The author is currently investigating the superpositions of multiple individually coded quasi- $(d-1)$ -spherical waves to further decorrelate the pulse echoes. He is simultaneously extending the implementation to the three-dimensional Euclidean space and exploring nonlinear CS to regularize the nonlinear ISP generalizing the Born approximation. Alternative orthonormal bases, e.g. wavelet bases, and customized redundant dictionaries [110], which can be learned from the ultrasound images of interest [111], potentially further improve fast compressed pulse-echo UI and deserve additional studies.

ACKNOWLEDGMENT

The author thanks Prof. Dr.-Ing. Georg Schmitz, who kindly provided access to the laboratory and the computer equipment. He gratefully acknowledges the financial support provided by German Academic Exchange Service (DAAD) for his invited talk at Acoustics '17 [59].

APPENDIX I

The outgoing free-space Green's functions (cf. e.g. [21, (2.14) and (2.19)], [22, (3.14) and (3.15)])

$$g_l(\mathbf{r}) = \begin{cases} j\mathbf{H}_0^{(2)}(k_l \|\mathbf{r}\|_2)/4 & \text{for } d = 2, \\ -e^{-jk_l \|\mathbf{r}\|_2}/(4\pi \|\mathbf{r}\|_2) & \text{for } d = 3, \end{cases} \quad (\text{A.55})$$

uniquely solve the fundamental inhomogeneous Helmholtz equations

$$(\Delta + k_l^2) g_l(\mathbf{r}) = \delta(\mathbf{r})$$

subject to the Sommerfeld radiation conditions (SRCs) (cf. e.g. [21, (1.48) or (2.8)], [22, (7.61)])

$$\lim_{r \rightarrow \infty} \max_{\|\mathbf{r}\|_2=r} \|\mathbf{r}\|_2^{\frac{d-1}{2}} [\langle \nabla g_l(\mathbf{r}), \mathbf{e}_r(\mathbf{r}) \rangle + jk_l g_l(\mathbf{r})] = 0 \quad (\text{A.56})$$

for all $l \in \mathbb{L}_{\text{BP}}^{(n)}$, where $\mathbf{H}_0^{(2)}$ denotes the zero-order Hankel function of the second kind [112, §10.2(ii) and 10.4.3], δ indicates the Dirac delta distribution, and $\mathbf{e}_r(\mathbf{r}) = \mathbf{r}/\|\mathbf{r}\|_2$ for all $\mathbf{r} \in \mathbb{R}^d \setminus \{\mathbf{0}\}$ is the radial unit vector. The SRCs (A.56) account for a lossy homogeneous fluid of infinite extent and ensure the causality in the time domain [21, Sect. 2.1.4].

APPENDIX II

The left multiplication of the normalized recorded RF voltage signals (41) by the adjoint normalized sensing matrix (39) yields

$$\check{\boldsymbol{\theta}}_{\xi}^{(\kappa)} = \bar{\mathbf{A}}_{\xi}^{\text{H}} [p^{(\text{in})}] \bar{\mathbf{u}}^{(\text{rx})} = \frac{1}{\|\bar{\mathbf{u}}^{(\text{rx})}\|_2} \mathbf{W}_{\xi}^{-1} \underbrace{\mathbf{A}^{\text{H}} [p^{(\text{in})}] \mathbf{u}^{(\text{rx})}}_{=\check{\boldsymbol{\theta}}^{(\kappa)}}.$$

Its components linearly combine the TPSFs (6) according to

$$\begin{aligned} \check{\boldsymbol{\theta}}_{\xi,i}^{(\kappa)} &= \left\langle \underbrace{\bar{\mathbf{A}}_{\xi} [p^{(\text{in})}] \bar{\boldsymbol{\theta}}_{\xi}^{(\kappa)}}_{=\bar{\mathbf{u}}^{(\text{rx})}} + \bar{\boldsymbol{\eta}}, \frac{\mathbf{a}_i [p^{(\text{in})}]}{a_{\xi,i} [p^{(\text{in})}]} \right\rangle \\ &= \left\langle \underbrace{\sum_{q \in [N_{\text{lat}}]} \frac{\mathbf{a}_q [p^{(\text{in})}]}{a_{\xi,q} [p^{(\text{in})}]} \bar{\boldsymbol{\theta}}_{\xi,q}^{(\kappa)}}_{=\bar{\mathbf{A}}_{\xi} [p^{(\text{in})}] \bar{\boldsymbol{\theta}}_{\xi}^{(\kappa)}}, \frac{\mathbf{a}_i [p^{(\text{in})}]}{a_{\xi,i} [p^{(\text{in})}]} \right\rangle + \frac{\langle \bar{\boldsymbol{\eta}}, \mathbf{a}_i [p^{(\text{in})}] \rangle}{a_{\xi,i} [p^{(\text{in})}]} \\ &= \sum_{q \in [N_{\text{lat}}]} \frac{\|\mathbf{a}_q\|_2 \|\mathbf{a}_i\|_2 \bar{\boldsymbol{\theta}}_{\xi,q}^{(\kappa)} \text{TPSF}\{\mathbf{A}\}(q,i)}{a_{\xi,q} a_{\xi,i}} + \frac{\langle \bar{\boldsymbol{\eta}}, \mathbf{a}_i \rangle}{a_{\xi,i}} \end{aligned} \quad (\text{A.57})$$

for all $i \in [N_{\text{lat}} - 1]_0$, where the dependence on $p^{(\text{in})}$ was omitted in the last line. Inserting the Fourier coefficients (8b), the components contain the zero-lag cross-correlations

$$\begin{aligned} \check{\boldsymbol{\theta}}_i^{(\kappa)} &= \sum_{n=0}^{N_{\text{in}}-1} \sum_{l \in \mathbb{L}_{\text{BP}}^{(n)}} \sum_{m=0}^{N_{\text{el}}-1} a_{m,l,i}^{(n)} * \frac{1}{T_{\text{rec}}^{(n)}} \underbrace{\int_{\mathbb{T}_{\text{rec}}^{(n)}} \tilde{u}_m^{(\text{rx},n)}(t) e^{-j\omega_l t} dt}_{=u_{m,l}^{(\text{rx},n)}} \\ &= \sum_{n=0}^{N_{\text{in}}-1} \sum_{m=0}^{N_{\text{el}}-1} \frac{1}{T_{\text{rec}}^{(n)}} \int_{\mathbb{T}_{\text{rec}}^{(n)}} \tilde{u}_m^{(\text{rx},n)}(t) \underbrace{\left[\sum_{l \in \mathbb{L}_{\text{BP}}^{(n)}} a_{m,l,i}^{(n)} e^{j\omega_l t} \right]^* dt}_{=\tilde{a}_{m,i}^{(n)}(t)} \\ &= \sum_{n=0}^{N_{\text{in}}-1} \sum_{m=0}^{N_{\text{el}}-1} \frac{1}{T_{\text{rec}}^{(n)}} \int_{\mathbb{T}_{\text{rec}}^{(n)}} \tilde{u}_m^{(\text{rx},n)}(t) \tilde{a}_{m,i}^{(n)*}(t) dt \end{aligned} \quad (\text{A.58})$$

for all $i \in [N_{\text{lat}} - 1]_0$.

REFERENCES

- [1] T. L. Szabo. *Diagnostic Ultrasound Imaging: Inside Out*. Elsevier Academic Press, 2nd edition, Dec. 2013.
- [2] S. M. Bierig and A. Jones. Accuracy and cost comparison of ultrasound versus alternative imaging modalities, including CT, MR, PET, and angiography. *J. Diagn. Med. Sonog.*, 25(3):138–144, May 2009.
- [3] J. T. Bushberg, J. A. Seibert, E. M. Leidholdt Jr., and J. M. Boone. *The Essential Physics of Medical Imaging*. Lippincott Williams & Wilkins, 3rd (north america) edition, Dec. 2011.
- [4] J. A. Jensen. Medical ultrasound imaging. *Prog. Biophys. Mol. Bio.*, 93(1–3):153–165, Jan.–Apr. 2007.
- [5] P. N. T. Wells. Ultrasound imaging. *Phys. Med. Biol.*, 51(13):R83–R98, Jul. 2006.
- [6] G. Montaldo, M. Tanter, J. Bercoff, N. Benech, and M. Fink. Coherent plane-wave compounding for very high frame rate ultrasonography and transient elastography. *IEEE Trans. Ultrason., Ferroelectr., Freq. Control*, 56(3):489–506, Mar. 2009.
- [7] E. Moghimirad, C. A. Villagómez Hoyos, A. Mahloojifar, B. Mohammadzadeh Asl, and J. A. Jensen. Synthetic aperture ultrasound Fourier beamformation using virtual sources. *IEEE Trans. Ultrason., Ferroelectr., Freq. Control*, 63(12):2018–2030, Dec. 2016.

- [8] J. A. Jensen, S. I. Nikolov, K. L. Gammelmark, and M. H. Pedersen. Synthetic aperture ultrasound imaging. *Ultrasonics*, 44, Supplement:e5–e15, Dec. 2006.
- [9] J. Cheng and J. y. Lu. Extended high-frame rate imaging method with limited-diffraction beams. *IEEE Trans. Ultrason., Ferroelectr., Freq. Control*, 53(5):880–899, May 2006.
- [10] J. y. Lu. 2D and 3D high frame rate imaging with limited diffraction beams. *IEEE Trans. Ultrason., Ferroelectr., Freq. Control*, 44(4):839–856, Jul. 1997.
- [11] M. Tanter and M. Fink. Ultrafast imaging in biomedical ultrasound. *IEEE Trans. Ultrason., Ferroelectr., Freq. Control*, 61(1):102–119, Jan. 2014.
- [12] J. Bercoff, M. Tanter, and M. Fink. Supersonic shear imaging: A new technique for soft tissue elasticity mapping. *IEEE Trans. Ultrason., Ferroelectr., Freq. Control*, 51(4):396–409, Apr. 2004.
- [13] J. Bercoff, G. Montaldo, T. Loupas, D. Savery, F. Meziere, M. Fink, and M. Tanter. Ultrafast compound Doppler imaging: Providing full blood flow characterization. *IEEE Trans. Ultrason., Ferroelectr., Freq. Control*, 58(1):134–147, Jan. 2011.
- [14] C. Papadacci, M. Pernot, M. Couade, M. Fink, and M. Tanter. High-contrast ultrafast imaging of the heart. *IEEE Trans. Ultrason., Ferroelectr., Freq. Control*, 61(2):288–301, Feb. 2014.
- [15] E. Mace, G. Montaldo, B. Osmanski, I. Cohen, M. Fink, and M. Tanter. Functional ultrasound imaging of the brain: Theory and basic principles. *IEEE Trans. Ultrason., Ferroelectr., Freq. Control*, 60(3):492–506, Mar. 2013.
- [16] J. Provost, C. Papadacci, J. E. Arango, M. Imbault, M. Fink, J.-L. Gennisson, M. Tanter, and M. Pernot. 3D ultrafast ultrasound imaging in vivo. *Phys. Med. Biol.*, 59(19):L1–L13, Oct. 2014.
- [17] D. Garcia, L. L. Tarnez, S. Muth, E. Montagnon, J. Porée, and G. Cloutier. Stolt's f - k migration for plane wave ultrasound imaging. *IEEE Trans. Ultrason., Ferroelectr., Freq. Control*, 60(9):1853–1867, Sep. 2013.
- [18] M. Zhang, F. Varray, A. Besson, R. E. Carrillo, M. Viallon, D. Garcia, J.-P. Thiran, D. Friboulet, H. Liebgott, and O. Bernard. Extension of Fourier-based techniques for ultrafast imaging in ultrasound with diverging waves. *IEEE Trans. Ultrason., Ferroelectr., Freq. Control*, 63(12):2125–2137, Dec. 2016.
- [19] P. Kruijzinga, F. Mastik, N. de Jong, A. F. W. van der Steen, and G. van Soest. Plane-wave ultrasound beamforming using a nonuniform fast Fourier transform. *IEEE Trans. Ultrason., Ferroelectr., Freq. Control*, 59(12):2684–2691, Dec. 2012.
- [20] M. F. Schiffrer and G. Schmitz. Plane wave pulse-echo ultrasound diffraction tomography with a fixed linear transducer array. In A. Nowicki, J. Litniewski, and T. Kujawska, editors, *Acoust. Imaging*, volume 31 of *Acoust. Imaging*, pages 19–30. Springer Netherlands, 2012.
- [21] A. J. Devaney. *Mathematical Foundations of Imaging, Tomography and Wavefield Inversion*. Cambridge University Press, 1st edition, Jul. 2012.
- [22] F. Natterer and F. Wübbeling. *Mathematical Methods in Image Reconstruction*. Mathematical Modeling and Computation. Society for Industrial and Applied Mathematics (SIAM), 2001.
- [23] A. C. Kak and M. Slaney. *Principles of Computerized Tomographic Imaging*. Classics in Applied Mathematics. Society for Industrial and Applied Mathematics (SIAM), 2001.
- [24] E. Ozkan, V. Vishnevsky, and O. Goksel. Inverse problem of ultrasound beamforming with sparsity constraints and regularization. *IEEE Trans. Ultrason., Ferroelectr., Freq. Control*, 65(3):356–365, Mar. 2018.
- [25] A. Besson, D. Perdios, F. Martinez, Z. Chen, R. E. Carrillo, M. Arditi, Y. Wiaux, and J.-P. Thiran. Ultrafast ultrasound imaging as an inverse problem: Matrix-free sparse image reconstruction. *IEEE Trans. Ultrason., Ferroelectr., Freq. Control*, 65(3):339–355, Mar. 2018.
- [26] B. Berthoin, P. Morichau-Beauchant, J. Porée, A. Garofalakis, B. Tavittian, M. Tanter, and J. Provost. Spatiotemporal matrix image formation for programmable ultrasound scanners. *Phys. Med. Biol.*, 63(3):03NT03, Feb. 2018.
- [27] A. Besson, M. Zhang, F. Varray, H. Liebgott, D. Friboulet, Y. Wiaux, J.-P. Thiran, R. E. Carrillo, and O. Bernard. A sparse reconstruction framework for Fourier-based plane-wave imaging. *IEEE Trans. Ultrason., Ferroelectr., Freq. Control*, 63(12):2092–2106, Dec. 2016.
- [28] G. David, J. I. Robert, B. Zhang, and A. F. Laine. Time domain compressive beam forming of ultrasound signals. *J. Acoust. Soc. Am.*, 137(5):2773–2784, May 2015.
- [29] Q. Zhang, B. Li, and M. Shen. A measurement-domain adaptive beamforming approach for ultrasound instrument based on distributed compressed sensing: Initial development. *Ultrasonics*, 53(1):255–264, Jan. 2013.
- [30] M. F. Schiffrer and G. Schmitz. Compensating the combined effects of absorption and dispersion in plane wave pulse-echo ultrasound imaging using sparse recovery. In *2013 IEEE Int. Ultrasonics Symp. (IUS)*, pages 573–576, Jul. 2013.
- [31] M. F. Schiffrer and G. Schmitz. The separate recovery of spatial fluctuations in compressibility and mass density in plane wave pulse-echo ultrasound imaging. In *2013 IEEE Int. Ultrasonics Symp. (IUS)*, pages 577–580, Jul. 2013.
- [32] M. F. Schiffrer and G. Schmitz. Fast image acquisition in pulse-echo ultrasound imaging using compressed sensing. In *2012 IEEE Int. Ultrasonics Symp. (IUS)*, pages 1944–1947, Oct. 2012.
- [33] M. F. Schiffrer, T. Jansen, and G. Schmitz. Compressed sensing for fast image acquisition in pulse-echo ultrasound. *Biomed. Tech.*, 57(SI-1 Track-B):192–195, Aug. 2012.
- [34] M. F. Schiffrer and G. Schmitz. Fast pulse-echo ultrasound imaging employing compressive sensing. In *2011 IEEE Int. Ultrasonics Symp. (IUS)*, pages 688–691, Oct. 2011.
- [35] S. Foucart and H. Rauhut. *A Mathematical Introduction to Compressive Sensing*. Applied and Numerical Harmonic Analysis. Springer, 1st edition, Aug. 2013.
- [36] G. Kutyniok. Theory and applications of compressed sensing. *GAMM-Mitteilungen*, 36(1):79–101, Aug. 2013.
- [37] R. G. Baraniuk. Compressive sensing [lecture notes]. *IEEE Signal Process. Mag.*, 24(4):118–121, Jul. 2007.
- [38] E. J. Candes and M. B. Wakin. An introduction to compressive sampling. *IEEE Signal Process. Mag.*, 25(2):21–30, Mar. 2008.
- [39] J. Provost and F. Lesage. The application of compressed sensing for photo-acoustic tomography. *IEEE Trans. Med. Imag.*, 28(4):585–594, Apr. 2009.
- [40] G.-H. Chen, J. Tang, and S. Leng. Prior image constrained compressed sensing (PICCS): A method to accurately reconstruct dynamic CT images from highly undersampled projection data sets. *Med. Phys.*, 35(2):660–663, Feb. 2008.
- [41] M. Lustig, D. Donoho, and J. M. Pauly. Sparse MRI: The application of compressed sensing for rapid MR imaging. *Magnet. Reson. Med.*, 58(6):1182–1195, Dec. 2007.
- [42] S. Foucart and M.-J. Lai. Sparsest solutions of underdetermined linear systems via ℓ_q -minimization for $0 < q \leq 1$. *Appl. Comput. Harmon. A.*, 26(3):395–407, May 2009.
- [43] R. Chartrand and W. Yin. Iteratively reweighted algorithms for compressive sensing. In *2008 IEEE Int. Conf. Acoustics, Speech and Signal Processing (ICASSP)*, pages 3869–3872, Mar.–Apr. 2008.
- [44] R. Chartrand. Exact reconstruction of sparse signals via nonconvex minimization. *IEEE Signal Process. Lett.*, 14(10):707–710, Oct. 2007.
- [45] G. Montaldo, D. Palacio, M. Tanter, and M. Fink. Building three-dimensional images using a time-reversal chaotic cavity. *IEEE Trans. Ultrason., Ferroelectr., Freq. Control*, 52(9):1489–1497, Sep. 2005.
- [46] T. Fromenteze, O. Yurduseven, M. Boyarsky, J. Gollub, D. L. Marks, and D. R. Smith. Computational polarimetric microwave imaging. *Opt. Express*, 25(22):27488–27505, Oct. 2017.
- [47] J. N. Gollub, O. Yurduseven, K. P. Trofatter, D. Armitz, M. F. Imani, T. Sleasman, M. Boyarsky, A. Rose, A. Pedross-Engel, H. Odabasi, T. Zvolensky, G. Lipworth, D. Brady, D. L. Marks, M. S. Reynolds, and D. R. Smith. Large metasurface aperture for millimeter wave computational imaging at the human-scale. *Sci. Rep.*, 7:42650, Feb. 2017.
- [48] T. Fromenteze, O. Yurduseven, M. F. Imani, J. Gollub, C. Decroze, D. Carsenat, and D. R. Smith. Computational imaging using a mode-mixing cavity at microwave frequencies. *Appl. Phys. Lett.*, 106(19):194104–1–194104–5, May 2015.
- [49] G. Lipworth, A. Mrozack, J. Hunt, D. L. Marks, T. Driscoll, D. Brady, and D. R. Smith. Metamaterial apertures for coherent computational imaging on the physical layer. *J. Opt. Soc. Am. A*, 30(8):1603–1612, Aug. 2013.
- [50] J. Hunt, T. Driscoll, A. Mrozack, G. Lipworth, M. Reynolds, D. Brady, and D. R. Smith. Metamaterial apertures for computational imaging. *Science*, 339(6117):310–313, Jan. 2013.
- [51] A. Besson, R. E. Carrillo, O. Bernard, Y. Wiaux, and J.-P. Thiran. Compressed delay-and-sum beamforming for ultrafast ultrasound imaging. In *2016 IEEE Int. Conf. Image Processing (ICIP)*, pages 2509–2513, Sep. 2016.
- [52] A. Liutkus, D. Martina, S. Popoff, G. Chardon, O. Katz, G. Lerosey, S. Gigan, L. Daudet, and I. Carron. Imaging with nature: Compressive imaging using a multiply scattering medium. *Sci. Rep.*, 4:5552, Jul. 2014.

- [53] P. Kruizinga, P. van der Meulen, A. Fedjajevs, F. Mastik, G. Springeling, N. de Jong, J. G. Bosch, and G. Leus. Compressive 3D ultrasound imaging using a single sensor. *Sci. Adv.*, 3(12), Dec. 2017.
- [54] A. Ghanbarzadeh-Dagheyan, C. Liu, A. Molaei, J. Heredia, and J. Martinez Lorenzo. Holey-cavity-based compressive sensing for ultrasound imaging. *Sensors*, 18(6), 2018.
- [55] R. van Sloun, A. Pandharipande, M. Mischi, and L. Demi. Compressed sensing for ultrasound computed tomography. *IEEE Trans. Biomed. Eng.*, 62(6):1660–1664, Jun. 2015.
- [56] J. Liu, Q. He, and J. Luo. Compressed sensing based synthetic transmit aperture imaging: Validation in a convex array configuration. *IEEE Trans. Ultrason., Ferroelectr., Freq. Control*, 65(3):300–315, Mar. 2018.
- [57] J. Liu, Q. He, and J. Luo. A compressed sensing strategy for synthetic transmit aperture ultrasound imaging. *IEEE Trans. Med. Imag.*, 36(4):878–891, Apr. 2017.
- [58] M. Schiffner and G. Schmitz. Random incident sound waves for fast compressed pulse-echo ultrasound imaging. In *2017 IEEE Int. Ultrasonics Symp. (IUS)*, page 1, Sept. 2017.
- [59] M. F. Schiffner and G. Schmitz. Fast compressive pulse-echo ultrasound imaging using random incident sound fields. *J. Acoust. Soc. Am.*, 141(5):3611, May 2017.
- [60] J. A. Tropp and S. J. Wright. Computational methods for sparse solution of linear inverse problems. *Proc. IEEE*, 98(6):948–958, Jun. 2010.
- [61] P. C. Hansen. *Discrete Inverse Problems: Insight and Algorithms*. Fundamentals of Algorithms. Society for Industrial and Applied Mathematics (SIAM), Jan. 2010.
- [62] P. C. Hansen. *Rank-Deficient and Discrete Ill-Posed Problems: Numerical Aspects of Linear Inversion*. Mathematical Modeling and Computation. Society for Industrial and Applied Mathematics (SIAM), Jan. 1998.
- [63] Y. C. Eldar and G. Kutyniok, editors. *Compressed Sensing: Theory and Applications*. Cambridge University Press, 1st edition, May 2012.
- [64] S. Foucart. A note on guaranteed sparse recovery via ℓ_1 -minimization. *Appl. Comput. Harmon. A.*, 29(1):97–103, Jul. 2010.
- [65] E. J. Candès. The restricted isometry property and its implications for compressed sensing. *C. R. Acad. Sci. Paris, Ser. I*, 346(9–10):589–592, May 2008.
- [66] A. M. Tillmann and M. E. Pfetsch. The computational complexity of the restricted isometry property, the nullspace property, and related concepts in compressed sensing. *IEEE Trans. Inf. Theory*, 60(2):1248–1259, Feb. 2014.
- [67] R. Baraniuk, M. Davenport, R. DeVore, and M. Wakin. A simple proof of the restricted isometry property for random matrices. *Constr. Approx.*, 28(3):253–263, Dec. 2008.
- [68] M. Fornasier and H. Rauhut. Compressive sensing. In O. Scherzer, editor, *Handbook of Mathematical Methods in Imaging*, pages 205–256. Springer, 2nd edition, 2015.
- [69] M. Rudelson and R. Vershynin. On sparse reconstruction from Fourier and Gaussian measurements. *Commun. Pur. Appl. Math.*, 61(8):1025–1045, Aug. 2008.
- [70] T. Chernyakova, R. Cohen, R. Mulayoff, Y. Sde-Chen, C. Fraschini, J. Bercoff, and Y. C. Eldar. Fourier-domain beamforming and structure-based reconstruction for plane-wave imaging. *IEEE Trans. Ultrason., Ferroelectr., Freq. Control*, 65(10):1810–1821, Oct. 2018.
- [71] M. F. Schiffner and G. Schmitz. A low-rate parallel Fourier domain beamforming method for ultrafast pulse-echo imaging. In *2016 IEEE Int. Ultrasonics Symp. (IUS)*, pages 1–4, Sep. 2016.
- [72] A. Burshtein, M. Birk, T. Chernyakova, A. Eilam, A. Kempinski, and Y. C. Eldar. Sub-Nyquist sampling and Fourier domain beamforming in volumetric ultrasound imaging. *IEEE Trans. Ultrason., Ferroelectr., Freq. Control*, 63(5):703–716, May 2016.
- [73] T. Chernyakova and Y. C. Eldar. Fourier-domain beamforming: The path to compressed ultrasound imaging. *IEEE Trans. Ultrason., Ferroelectr., Freq. Control*, 61(8):1252–1267, Aug. 2014.
- [74] N. Wagner, Y. C. Eldar, and Z. Friedman. Compressed beamforming in ultrasound imaging. *IEEE Trans. Signal Process.*, 60(9):4643–4657, Sep. 2012.
- [75] D. G. Manolakis, V. K. Ingle, and S. M. Kogon. *Statistical and Adaptive Signal Processing: Spectral Estimation, Signal Modeling, Adaptive Filtering, and Array Processing*. Artech House Signal Processing Library. Artech House, Inc., 2005.
- [76] W. L. Briggs and V. E. Henson. *The DFT: An Owner's Manual for the Discrete Fourier Transform*. Other Titles in Applied Mathematics. Society for Industrial and Applied Mathematics (SIAM), 1995.
- [77] National Cancer Institute (NCI) at the National Institutes of Health (NIH). NCI Dictionary of Cancer Terms, May 2017. <https://www.cancer.gov/publications/dictionaries/cancer-terms/def/soft-tissue>
- [78] J. Ng, R. Prager, N. Kingsbury, G. Treece, and A. Gee. Modeling ultrasound imaging as a linear, shift-variant system. *IEEE Trans. Ultrason., Ferroelectr., Freq. Control*, 53(3):549–563, Mar. 2006.
- [79] J. A. Jensen. Ultrasound imaging and its modeling. In M. Fink, W. A. Kuperman, J.-P. Montagner, and A. Tourin, editors, *Imaging of Complex Media with Acoustic and Seismic Waves*, volume 84 of *Topics in Applied Physics*, pages 135–166. Springer, 1st edition, 2002.
- [80] J. A. Jensen. A model for the propagation and scattering of ultrasound in tissue. *J. Acoust. Soc. Am.*, 89(1):182–190, Jan. 1991.
- [81] J. C. Gore and S. Leeman. Ultrasonic backscattering from human tissue: A realistic model. *Phys. Med. Biol.*, 22(2):317–326, Mar. 1977.
- [82] F. A. Duck. *Physical Properties of Tissue - A Comprehensive Reference Book*. Academic Press Limited, 1990.
- [83] P. N. T. Wells. Absorption and dispersion of ultrasound in biological tissue. *Ultrason. Med. Biol.*, 1(1):369 – 376, Mar. 1975.
- [84] J. F. Kelly, R. J. McGough, and M. M. Meerschaert. Analytical time-domain Green's functions for power-law media. *J. Acoust. Soc. Am.*, 124(5):2861–2872, Nov. 2008.
- [85] K. R. Waters, J. Mobley, and J. G. Miller. Causality-imposed (Kramers-Kronig) relationships between attenuation and dispersion. *IEEE Trans. Ultrason., Ferroelectr., Freq. Control*, 52(5):822–833, May 2005.
- [86] T. L. Szabo. Causal theories and data for acoustic attenuation obeying a frequency power law. *J. Acoust. Soc. Am.*, 97(1):14–24, Jan. 1995.
- [87] L. W. Schmerr Jr. *Fundamentals of Ultrasonic Phased Arrays*, volume 215 of *Solid Mechanics and Its Applications*. Springer International Publishing, 1st edition, 2015.
- [88] Y. Labyed and L. Huang. TR-MUSIC inversion of the density and compressibility contrasts of point scatterers. *IEEE Trans. Ultrason., Ferroelectr., Freq. Control*, 61(1):16–24, Jan. 2014.
- [89] M. Born and E. Wolf. *Principles of Optics: Electromagnetic Theory of Propagation, Interference and Diffraction of Light*. Cambridge University Press, 7th (expanded) edition, Oct. 1999.
- [90] J. Li, X. Wang, and T. Wang. On the validity of Born approximation. *Prog. Electromagn. Res.*, 107:219–237, 2010.
- [91] W. C. Chew, J.-M. Jin, C.-C. Lu, E. Michielssen, and J. M. Song. Fast solution methods in electromagnetics. *IEEE Trans. Antennas Propag.*, 45(3):533–543, Mar. 1997.
- [92] V. Rokhlin. Rapid solution of integral equations of scattering theory in two dimensions. *J. Comput. Phys.*, 86(2):414–439, Feb. 1990.
- [93] S. Mallat. *A Wavelet Tour of Signal Processing: The Sparse Way*. Academic Press, 3rd edition, 2009.
- [94] E. van den Berg and M. P. Friedlander. Probing the pareto frontier for basis pursuit solutions. *SIAM J. Sci. Comput.*, 31(2):890–912, 2009.
- [95] W. C. Gibson. *The Method of Moments in Electromagnetics*. CRC Press, 2nd edition, Aug. 2014.
- [96] R. Coifman, V. Rokhlin, and S. Wandzura. The fast multipole method for the wave equation: A pedestrian prescription. *IEEE Antennas Propag. Mag.*, 35(3):7–12, Jun. 1993.
- [97] L. Demanet and L. Ying. Wave atoms and sparsity of oscillatory patterns. *Appl. Comput. Harmon. A.*, 23(3):368–387, Nov. 2007.
- [98] Z. Wang and A. C. Bovik. Mean squared error: Love it or leave it? A new look at Signal Fidelity Measures. *IEEE Signal Process. Mag.*, 26(1):98–117, Jan. 2009.
- [99] E. J. Candès, M. B. Wakin, and S. P. Boyd. Enhancing sparsity by reweighted ℓ_1 minimization. *J. Fourier Anal. Appl.*, 14(5–6):877–905, Dec. 2008.
- [100] A. Achim, A. Basarab, G. Tzagkarakis, P. Tsakalides, and D. Kouamé. Reconstruction of ultrasound RF echoes modeled as stable random variables. *IEEE Trans. Comput. Imag.*, 1(2):86–95, Jun. 2015.
- [101] M. F. Schiffner and G. Schmitz. Pulse-echo ultrasound imaging combining compressed sensing and the fast multipole method. In *2014 IEEE Int. Ultrasonics Symp. (IUS)*, pages 2205–2208, Sep. 2014.
- [102] S. Chaillat and G. Biros. FaIMS: A fast algorithm for the inverse medium problem with multiple frequencies and multiple sources for the scalar Helmholtz equation. *J. Comput. Phys.*, 231(12):4403–4421, Jun. 2012.
- [103] K. Zhao, M. N. Vouvakis, and J.-F. Lee. The adaptive cross approximation algorithm for accelerated method of moments computations of EMC problems. *IEEE Trans. Electromagn. Compat.*, 47(4):763–773, Nov. 2005.
- [104] L. Demanet and L. Ying. Scattering in flatland: Efficient representations via wave atoms. *Found. Comput. Math.*, 10(5):569–613, Oct. 2010.

- [105] T. Blu, P.-L. Dragotti, M. Vetterli, P. Marziliano, and L. Coulot. Sparse sampling of signal innovations. *IEEE Signal Process. Mag.*, 25(2):31–40, Mar. 2008.
- [106] M. Vetterli, P. Marziliano, and T. Blu. Sampling signals with finite rate of innovation. *IEEE Trans. Signal Process.*, 50(6):1417–1428, Jun. 2002.
- [107] M. F. Schiffner and G. Schmitz. Ultrafast image acquisition in pulse-echo ultrasound imaging using compressed sensing. In *2016 IEEE Int. Ultrasonics Symp. (IUS)*, pages 1–3, Sep. 2016.
- [108] T. Misaridis and J. A. Jensen. Use of modulated excitation signals in medical ultrasound. Part III: High frame rate imaging. *IEEE Trans. Ultrason., Ferroelectr., Freq. Control*, 52(2):208–219, Feb. 2005.
- [109] T. Ilovitsh, A. Ilovitsh, J. Foiret, B. Z. Fite, and K. W. Ferrara. Acoustical structured illumination for super-resolution ultrasound imaging. *Nat. Commun. Biol.*, 1(1):3, Jan. 2018.
- [110] E. J. Candes, Y. C. Eldar, D. Needell, and P. Randall. Compressed sensing with coherent and redundant dictionaries. *Appl. Comput. Harmon. A.*, 31(1):59–73, Jul. 2011.
- [111] O. Lortintu, H. Liebgott, M. Alessandrini, O. Bernard, and D. Friboulet. Compressed sensing reconstruction of 3D ultrasound data using dictionary learning and line-wise subsampling. *IEEE Trans. Med. Imag.*, 34(12):2467–2477, Dec. 2015.
- [112] F. W. J. Olver, D. W. Lozier, R. F. Boisvert, and C. W. Clark, editors. *NIST Handbook of Mathematical Functions*. Cambridge University Press, 2010.